Politecnico di Torino

ScuDo
Scuola di Dottorato ~ Doctoral School
WHAT YOU ARE, TAKES YOU FAR

Doctoral Dissertation
Doctoral Program in Metrology (36^{th}cycle)

Development of Superconducting Single-Particle Detector Transition-Edge Sensor

By

Carlo Pepe

******

Supervisor(s):
Dr. M. Rajteri, Supervisor
Dr. E. Monticone, Co-Supervisor

Doctoral Examination Committee:
Prof. L. Gastaldo, Referee, Kirchhoff Institute for Physics, Heidelberg University
Dr. L. Gottardi, Referee, NWO-I/SRON, Netherlands Institute for Space Research

Politecnico di Torino
2024

Declaration

I hereby declare that, the contents and organization of this dissertation constitute my own original work and does not compromise in any way the rights of third parties, including those relating to the security of personal data.

Carlo Pepe
2024

* This dissertation is presented in partial fulfillment of the requirements for **Ph.D. degree** in the Graduate School of Politecnico di Torino (ScuDo).

Acknowledgements

I would like to express my deepest appreciation to:

- Dr. Mauro Rajteri for his meticulous supervision during these years of my PhD, both in the laboratory and in the writing of this thesis. His availability and patience, even for daily discussions, have been crucial for the success of this work.
- Dr. Eugenio Monticone for the unwavering scientific and moral support he has provided over the years. His profound knowledge of the subject and his sense of humor have always been a guiding reference throughout my journey.
- Dr. Sebastian Raupach and Dr. Jörn Beyer for being my supervisors at PTB, with funding from the PTB guest research program.
- Dr. Laura Manenti and the NYUAD group for the scientific collaboration in the QHaloS experiment.
- Dr. Francesco Pandolfi and the INFN Rome and Sapienza University of Rome colleagues for the scientific collaboration within the PTOLEMY project.
- Hobey Garrone for his collaboration in the fabrication of TES devices.

I also would like to thank:

- Danilo Serazio and Elio Bertacco for their technical support. Despite the improbable and often last-minute requests, they have always been available and professional. Without their help, this work would have suffered.
- Dr. Giorgio Brida for his scientific support.

- The PTOLEMY collaboration for useful discussions and founding. This work was partially funded by the contribution of grant 62313 from the John Templeton Foundation.
- The SEQUME collaboration for useful discussions, particularly with Dr. D. Fukuda.
- Dr. Matteo Fretto and Ivan De Carlo for their technical support.
- The students Federico Malnati and Benedetta Corcione for their valuable help in the lab while I was writing this thesis.
- The Quantum Optics Group at INRiM led by Prof. Marco Genovese for their scientific and technical support over the years.

Abstract

This thesis presents the development and advancement of superconducting single-particle detectors, specifically Transition-Edge Sensors (TESs), focusing on enhancing their performance for various scientific fields. TESs are highly sensitive microcalorimeters capable of detecting radiation across a wide spectrum, from sub-millimeter wavelengths to gamma rays, due to their intrinsic energy resolution. They are also known for their near-unit system detection efficiency, low dark count rate and photon-number resolution capabilities. This work was conducted at the Istituto Nazionale di Ricerca Metrologica (INRiM), the National Metrology Institute of Italy, where I worked in the Innovative Cryogenic Detectors Laboratory using TES devices fabricated at QR Laboratories, a micro and nanofabrication lab.

The primary motivation for this research is to improve TES performance to enhance their use in physical and metrological experiments. Among these is the PontCorvo Tritium Observatory for Light, Early-Universe, Massive-neutrino Yield (PTOLEMY) experiment, which seeks to detect the Cosmic Neutrino Background (CNB). TES devices with an energy resolution of 0.11 eV are required to detect electrons produced by CNB via neutrino captures on beta-unstable nuclides, providing insights into the early universe and the nature of neutrinos. Two TiAu TES, with areas of 20 μm $\times$ 20 μm and 50 μm $\times$ 50 μm, were characterized, achieving energy resolutions of 0.114 eV and 0.158 eV, respectively. These results are particularly noteworthy as they match state-of-the-art energy resolutions reported in the literature but with TES devices of significantly larger area. This advancement is critical for the PTOLEMY project because it facilitates the implementation of large-area detectors based on an array of TESs.

Moreover, this thesis demonstrates the first detection of electrons with kinetic energy in the 100 eV range using a TES. This was achieved with a 100 μm $\times$ 100 μm TiAu TES. Electrons were produced directly in the cryostat by a cold-cathode source

based on field emission from vertically-aligned multiwall carbon nanotubes. The energy resolution obtained for fully-absorbed electrons in the $(90-101)$ eV energy range was between 1.8 eV and 4 eV, compatible with the resolution for photons in the same energy range. This measurement opens new possibilities in electron detection, crucial for PTOLEMY, where TES devices must detect electrons with high precision, but also in electron spectroscopy.

The Quantum Haloscope Search experiment (QHaloS) aims to search for light dark matter in the form of dark photons using a dielectric haloscope equipped with a TES for photon detection. This innovative detector aims to convert non-relativistic dark photons into Standard Model photons, which are then detected by the TES. Since the experiment searches for rare events, it requires a detector with high efficiency and low dark count rate (DCR). We characterized the intrinsic DCR of a TiAu TES having an area of 20 μm $\times$ 20 μm, finding it to be 3.6×10^{-4} Hz in the 0.8 eV to 3.2 eV range. Furthermore, a deeper study was conducted to categorize the types of dark counts in TES to improve its use in the experiment.

The Single and Entangled Photon Sources for Quantum Metrology (SEQUME) project aims to develop high-purity single-photon sources and high-efficiency entangled-photon sources for quantum-enhanced measurements in quantum metrology. A TES with high efficiency is crucial for characterizing these single-photon sources. The results for the SEQUME project were obtained at the PTB in Braunschweig (Germany) during a four-month period abroad in my third year of PhD. In this thesis I present the measurement on a TiAu TES fabricated at AIST (Japan) with a system detection efficiency of 98%, a significant milestone for the SEQUME project's objectives.

Finally, the thesis describes preliminary results on the development of TES with fast recovery time to enhance operation above 1 MHz. Two distinct approaches are presented: one involving the use of Al TES with a high critical temperature, and the second utilizing Au pads to increase thermal conductance.

Overall, this thesis encompasses the development, characterization and application of advanced TES devices, significantly contributing to their potential use in metrological and fundamental physics research, pushing the boundaries of their performance.

Contents

Chapter 1

Introduction

The general context of my research is the development and enhancement of Transition-Edge Sensors (TESs) [1] for high-precision applications in quantum metrology, dark matter research, neutrino physics, and radiometry. TES detectors, which are a class of superconducting single-photon detectors, are used to detect radiation across a wide spectrum, from sub-millimeter wavelengths to gamma rays [2–5]. In this thesis, I will focus on improving their performances in the optical to near-infrared (IR) energy range, where they are among the best single-photon detectors [6, 7]. Most of my work has been carried out at the Istituto Nazionale di Ricerca Metrologica (INRiM) the National Metrology Institute of Italy, in the Turin campus.

The development of single-photon detectors began in the 1930s, leading to the creation of well-established solid-state detectors such as the photomultiplier tube and the single-photon avalanche diode, which have significantly impacted various research fields [8, 9]. However, Superconducting Single-Photon Detectors (SSPDs) represent a newer class of detectors with significantly improved performances. In particular, TESs, along with Superconducting Tunnel Junctions (STJs) [10], Kinetic Inductance Detectors (KIDs) [11], and Superconducting Nanowire Single-Photon Detectors (SNSPDs) [12], have demonstrated excellent performances in the optical to IR photon range by exploiting superconductivity for single-photon detection.

The key figures of merit for superconducting single-photon detectors, on which my research is focused, include:

- **System Detection Efficiency (SDE)**: SSPDs have achieved near-unit SDE at specific photon energies. TES detectors, for instance, have reported SDEs of 95% at 1556 nm [13] and 98% at 850 nm [14].
- **Dark Count Rate (DCR)**: TES detectors exhibit exceptionally low dark count rates (mHz range), making them ideal for applications requiring extremely low background noise [15, 16].
- **Energy Resolution (ΔE)**: TESs inherently possess excellent energy resolution capabilities, enabling them to discriminate single photons with a resolution as fine as 67 meV [17, 18].
- **Photon-Number Resolution (PNR)**: TES detectors can generate an output signal proportional to the cumulative energy of multiple photon absorption events, achieving photon-number resolution up to 55 incident photons at 1540 nm [19].
- **Time performances**: Among SSPDs, SNSPDs exhibit the best performances for both recovery time [20] and time jitter [21]. However, there is ongoing effort to reduce the recovery time of TES devices to enable high-repetition-rate experiments [22] and to minimize time jitter [23].

1.1 Motivation

The primary objective of my PhD thesis is to enhance the performances of TES to meet the demands of ongoing and future experiments. This involves characterizing these devices to ensure they achieve the necessary performance metrics.

Specifically, my research aims to reach 5 different objective:

1. Achieve excellent energy resolution with TES devices covering large areas to facilitate future realization of TES arrays. This is crucial for applications where the detection area required exceeds the capability of a single device.
2. Demonstrate that TESs can function as single-electron detectors with energy resolution comparable to that of photons.
3. Characterize and study the dark counts in TESs for rare events applications.

4. Attain a system detection efficiency greater than 90%, enabling the establishment of a single-photon source calibration facility.

5. Reduce the recovery time of TES to reach detection rate higher then 1 MHz as requested by state-of-the-art single photon sources.

In the following sections, I will introduce the experimental context that motivates these developments and researches.

1.1.1 PonteCorvo Tritium Observatory for Light, Early-Universe, Massive-neutrino Yield Experiment (PTOLEMY)

The PonteCorvo Tritium Observatory for Light, Early-Universe, Massive-neutrino Yield (PTOLEMY) project [24] aims to directly detect the Cosmic Neutrino Background (CNB), produced approximately one second after the Big Bang [25–27]. This detection is crucial as it offers insights into the early universe and the nature of neutrinos. The experiment plans to use tritium implanted on a carbon-based nanostructure to detect CNB via neutrino captures on beta-unstable nuclides.

The detection process involves observing electron kinetic energies emitted from a tritium target that are above the beta-decay endpoint. This allows the separation of the CNB signal from the beta-decay endpoint, requiring an energy resolution in full width half max (fwhm) of 0.11 eV at 10 eV. To achieve this precision, PTOLEMY will employ TESs as single electron detector in the microcalorimeter setup [28].

A demonstrator of the PTOLEMY experiment setup is depicted in Figure 1.1. PTOLEMY's setup consists of four key modules: the tritium target, a dynamic electromagnetic filter [29], a radio-frequency (RF) antenna for preselection, and an array of microcalorimeters based on TES. The source uses hydrogenated graphene to bind tritium atoms, providing a solid-state platform with high tritium density. The dynamic electromagnetic filter selects electrons with specific energy characteristics, guiding them toward an array of microcalorimeter for precise energy measurement. Considering a target of 100 g of tritium are expected only few events per year. The total area that the array should cover is still under evaluation by the collaboration.

At this stage of the project, the goals for TES development are twofold: to achieve the target energy resolution while increasing the device's area and to demonstrate TES

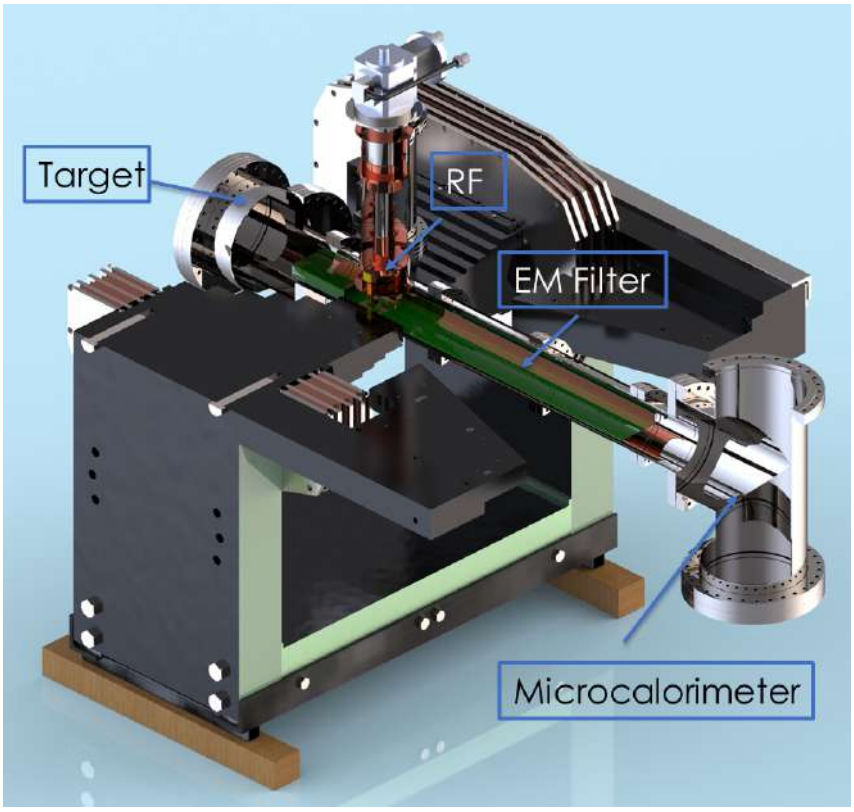

Fig. 1.1 Demonstrator of the PTOLEMY experiment setup.

capability in detecting electrons. To enhance energy resolution while maintaining a large detection area, it is necessary to minimize the device's thermal capacity and reduce the operation temperature. Additionally, to demonstrate that TES can function as single-electron detectors, it is crucial to generate low-energy electrons in a cryogenic environment. This can be accomplished using field emission from Carbon Nanotubes (CNTs) mounted in front of the TES and applying an electric field.

1.1.2 Quantum Haloscope for Dark Matter Search (QHaloS)

The Quantum Haloscope Search experiment (QHaloS) is designed to search for light dark matter in the form of dark photons using a novel detection technique known as the "dielectric haloscope" [30]. This innovative detector operates beyond the current state-of-the-art in this mass range, offering a great opportunity for dark matter discovery.

Significant evidence suggests that approximately 85% of the Universe's mass is in the form of dark matter (DM), a new type of particle beyond the Standard Model [31]. While direct DM searches have primarily focused on weakly-interacting massive particles (WIMPs), alternative models are also gaining attention. As large experiments rule out favored WIMP parameter spaces, dark photons (DPs) have become increasingly interesting among alternative DM models. The DP naturally arises in extensions of the Standard Model, hypothesizing the existence of an extra U(1) symmetry coupled to the U(1) gauge group of electromagnetism via kinetic mixing [32].

QHaloS is an upgrade of the Multilayer Dielectric Haloscope Investigation (MuDHI) [33] and aims to extend the search for DPs to weaker couplings using a dielectric haloscope equipped with a TES for photon detection. A dielectric haloscope utilizes a stack of alternating dielectric layers to convert into Standard Model (SM) photons. This conversion is facilitated through the breaking of translational invariance by altering the medium in which dark photons propagate. In the haloscope, the dielectric stack transforms dark photons into SM photons, which are then focused onto the TES. The energy of the converted photon corresponds to the mass of the dark photon [30].

The advantages of using a TES for such an experiment are that it can be designed to have a near-unit SDE in the same energy range where we expect the conversion from DP to SM photon, and TES can aim for a DCR of the order of mHz or below. Moreover, the TES is capable of differentiating the energy of the detected particle and this could be an advantage with respect to current experiments, like [34], where the detector applied is a SNSPD which can not distinguish the energies of the events. At this phase of the project, it is fundamental to characterize more in detail the dark count and tray to further suppress them. To study the intrinsic dark counts in TES, the signals produced by the TES in complete darkness within the cryostat needs first to be identified. It is important to address the difference between single-photon-like events and those caused by high-energy particles or electrical signals, which can be excluded from the dark count rate. Subsequent studies will investigate the correlation between high-energy events and single-photon-like events.

1.1.3 Single and Entangled Photon Sources for Quantum Metrology (SEQUME)

The SEQUME project aims to develop and enhance high-purity single-photon sources and high-efficiency entangled-photon sources. The project's goal is to apply these sources in quantum metrology to achieve quantum-enhanced measurements, providing a significant advantage over classical methods [35, 36]. SEQUME focuses on developing new fabrication methods for single-photon sources with high purity, brightness, and indistinguishability. These sources include defects in diamond [37], quantum dots [38], and single molecules [39]. By enhancing these sources, the project aims to improve the performances and capabilities of quantum measurements.

A key objective of SEQUME is to establish a European metrological infrastructure for the characterization of single-photon sources using TES detectors. This involves creating a standardized framework to ensure the accuracy and reliability of quantum measurements, which is crucial for the advancement of quantum technologies.

To this end, the project aims to integrate two TES detectors into a facility with an SDE above 90% at 930 nm and 1540 nm. To ensure this high SDE is achieved, measurements must be performed using a setup calibrated against a cryogenic radiometer, guaranteeing a well-known number of photons input to the cryostat.

Moreover, the project seeks to improve the recovery time of the TESs and achieve a detection rate above 2 MHz while maintaining PNR. To improve the recovery time of a TES, two approaches can be employed: increasing the operating temperature and enhancing the thermal conductance of the device.

1.2 Thesis Outline

In Chapter 2, I provide a detailed description of superconducting single-photon detectors. Section 2.1 offers an overview of superconductivity and the energy down-conversion process that occurs when a photon is absorbed by a superconductor. In Section 2.2, I discuss the four most relevant types of SSPDs: STJ, TES, SNSPD, and KID. Then, in Section 2.3, I delve into the state-of-the-art performances of TES detectors.

In Chapter 3, I present a theoretical model of TES operation. Starting from the thermal model of a superconductor coupled to a thermal bath (3.1), I introduce electrothermal feedback (3.2). The chapter continues with a description of how a Superconducting QUantum Interference Device (SQUID) can be used as a transimpedance amplifier to read out the TES response (3.3). In the following section, a comprehensive analysis of the TES response is presented (3.4). The chapter concludes with a section describing how important figures of merit can be theoretically described and the parameters to tune in order to improve them (3.5).

In Chapter 4, the experimental setups needed for the development and characterization of the TES used in this thesis are described. The low-temperature setup is detailed in Section 4.1, and Section 4.2 explains how the SQUID amplifier and its electronics are integrated into it. Section 4.3 describes the alignment system used to couple optical fiber to the TES. The setup used for the assessment of TES high SDE for the SEQUME project is detailed in Section 4.4. Sections 4.5 provide more details on the setups used for the integration of an electron source based on CNT in the cryostat. The chapter concludes with a highlight of the fabrication method used for TES development (4.6).

Chapter 5 is divided into five main sections that highlight the results corresponding to the five objectives of this thesis:

1. **Energy Resolution (Section 5.1):** The ongoing efforts to optimize TES detectors for excellent energy resolution while increasing the TES active area are described. I present two TES devices with high energy resolution and areas of 20 μm $\times$ 20 μm and 50 μm $\times$ 50 μm.

2. **Detection of Low-Energy Electrons (Section 5.2):** I present the results for the first detection of single electrons in the energy range of 100 eV, demonstrating that the energy resolution of TES for photons is comparable to that for electrons.

3. **Study of Dark Counts for Rare Event Searches (Section 5.3):** I present the test runs conducted to measure the intrinsic DCR of TES and the efforts to understand the origin of these dark counts.

4. **System Detection Efficiency Measurement (Section 5.4):** The preparation of a cryo-optical facility with high SDE and the achievement of an SDE of 98% at 1550 nm are discussed.

5. **Preliminary Results for Fast TES (Section 5.5):** The approach and results obtained in pursuing faster TES recovery times, either by using high T_C materials or by enhancing the conductance through gold pads, are presented.

Chapter 6 concludes the thesis, summarizing the key findings and discussing potential future work.

Chapter 2

Superconducting Single-Photon Detectors

In scientific experiments, especially those focused on understanding the structure of matter, a common framework is often employed. This framework includes a Probe, which can be a particle or a wave, an Interaction, and a Detector designed to capture and record the interactions of the probe. For example, in a basic optical microscope setup, light serves as the probe directed at a sample, while a system of lenses and our eyes act as the detector.

In the 17th century, Robert Hooke utilized this framework to examine cork in detail, leading to the discovery of small cavities separated by walls, which he called "cells". His scientific inquiry raised the fundamental question, "What are we made of?" In this setup, photons act as the probe, interacting with cork cells through processes like reflection, absorption, or transmission, depending on the cell's structure. The optics, including lenses, and our eyes play the role of the detector.

While our eyes function well as detectors, they have limitations in resolving dimensions down to hundreds of micrometers. The use of lenses in optical microscopes was a pivotal enhancement that allowed Hooke to observe cells for the first time, illustrating how advancements in detection technology can lead to significant scientific discoveries. Similarly, ongoing research to improve detection performance is crucial for advancing our understanding of the world.

In this thesis, I will discuss a different detection system from the optical microscope used by Hooke, focusing on a state-of-the-art single-photon detector known

as a Transition-Edge Sensor (TES) [1]. I will present the efforts made to enhance the performance of TES detectors and how these improvements can be applied in various physics experiments. This research underscores the importance of developing more sensitive and precise detection systems to push the boundaries of scientific exploration.

> "A single-photon detector is a device that can produce a measurable output signal, distinguishable from noise, due to a single photon incident on the detector's input plane" [40].

A single-photon detector is a highly sensitive device designed to detect individual photons, the smallest discrete units or quanta of light. These detectors are crucial in various fields of science and technology, including quantum computing [41], quantum communication [8], quantum-enabled metrology [42], astronomy [43], medical imaging [44], and fundamental physics [45].

A TES, in particular, is a superconducting single-photon detector, meaning that its functionality relies on the properties of superconducting materials. The development of single-photon detectors began in the 1930s, and since then, well-established solid-state detectors such as the photomultiplier tube and the single-photon avalanche diode have become available, having a great impact on various research fields [9]. Superconducting Single-Photon Detectors (SSPDs), on the other hand, represent a newer class of detectors with significantly improved performance. In particular, in the range of optical to near-infrared (IR) photons, TESs [1], along with Superconducting Tunnel Junctions (STJs) [10], Kinetic-Inductance Detectors (KIDs) [11], and Superconducting Nanowire Single-Photon Detectors (SNSPDs) [12], have shown great performance by exploiting superconductivity for single-photon detection. Some of the most important metrics of single-photon detectors where SSPDs excel in the optical and IR range, achieving state-of-the-art performance, include:

- **System Detection Efficiency (SDE)**

  > "System Detection Efficiency is the probability of a complete single-photon detection system to indicate a detection event due to one photon incident at the system's input plane" [40].

This metric includes all the efficiency terms in the detection system, from the optical losses to the readout. Ideally, in any experiment, the SDE should be 100%.

- **Dark Count Rate (DCR)**

  > "A dark count is a detection event in a single-photon or PNR detector that is uncorrelated with light at the input plane of the detector" [40].

  The Dark Count Rate (DCR) is the number of dark counts per unit time and is a metric that should ideally be zero. In experiments where the rate of events is low, a DCR higher than the rate of events would compromise the measurement. Achieving a very low DCR allows the detector to be used in rare event experiments.

- **Energy Resolution (ΔE)**

  Energy resolution refers to a detector's ability to differentiate between particles with closely spaced energy levels. An excellent energy resolution means that the detector can distinguish between events differing by only a small amount of energy. Ideally, the energy resolution of a detector should be zero, allowing for the discrimination of any discrete amount of energy.

- **Photon-Number Resolution (PNR)**

  > "A photon-number-resolving detector produces an output that is inherently representative of the number of photons input to the detector (over some range of photon numbers). From that output, an integer number of detected photons can be determined with some level of uncertainty, usually significantly less than one" [40].

  Detectors with intrinsic energy resolution can generate an output signal proportional to the cumulative energy of multiple photon absorption events. With ideal energy resolution, the PNR of a detector can be extended to any energy range. Moreover, an ideal single-photon detector would have PNR for an infinite number of photons with performance similar to single-photon events.

- **Recovery Time**

> "The recovery time of a single-photon detector is the total amount of time required after a detection event for the detection efficiency to return to its nominal steady-state value." [40].

This metric defines the amount of time during an experiment in which we are blind or not operating in ideal conditions. Ideally, a single-photon detector would have a recovery time of zero. This metric is strictly linked with the maximum detection rate.

- **Maximum Detection Rate (MDR)**

  > "The maximum count rate of a single-photon detector is a metric for the maximum rate at which a detection system can register detection events." [40].

  The lower the time we need to wait for the detection system to recover, the higher the detection rate can be. For an ideal system that needs zero recovery time, the maximum detection count (MDC) could be infinite.

- **Timing Jitter**

  > "Detector timing jitter is the variation in the time delay between when light arrives at the detector input plane and when a signal is output from the detector" [40].

  Low timing jitter is a crucial performance characteristic for some single-photon detection experiments, as it represents the uncertainty in determining the precise arrival time of a photon. Ideally, it should be zero.

The metrics presented here are crucial for defining the performance of single-photon detection systems in the optical-IR range. For each metric, I have outlined the ideal performance value. While achieving these ideal values is often challenging, this chapter will demonstrate that SSPDs can closely approach these targets under certain conditions. Notably, both TES and SNSPDs have achieved near-unit SDE at specific photon energies, as evidenced by studies such as [13, 14, 46–48].

However, there are additional metrics beyond those discussed here that may be important depending on the application. For instance, polarization sensitivity and the capability to create arrays of single-photon detectors are significant aspects in

the development of these devices. Despite this, the main focus of this thesis will be on the key performance metrics mentioned above.

In the following sections, I will briefly introduce the principles of superconductivity and how they are exploited by superconducting single-photon detectors. Then, I will discuss the state-of-the-art performance of these detectors concerning the key parameters previously outlined, with a particular emphasis on Transition-Edge Sensors. The informations provided here are based on recent reviews by D.V. Morozov et al. [6] and A. Lita et al. [7], which will serve as references for the rest of the chapter.

2.1 Overview of Superconductivity

Superconductivity was discovered in 1911 when Heike Kamerlingh Onnes observed that the resistance of solid mercury vanished when cooled to 4.15 K [49]. A few decades later, in the 1950s, theoretical frameworks were developed to explain phenomena such as the Meissner effect, a form of perfect diamagnetism [50], and quantum properties like fluxoid quantization [51]. The Ginzburg-Landau (GL) model was introduced to describe superconductivity through an order parameter representing a condensate of superconducting charge carriers with effective mass m^* and charge e^* [52]. This model leads to the derivation of the London equation [53], which characterizes the magnetic behavior of superconductors. Within the GL model, key superconducting properties like the magnetic penetration depth (λ_{L}) and the coherence length (ξ_{GL}) can be derived. These parameters indicate the depth to which magnetic fields penetrate and the distance over which the superconducting condensate varies significantly.

Superconductivity was further explained through the BCS theory, proposed by J. Bardeen, L. Cooper, and J. R. Schrieffer in 1957 [54, 55]. The BCS theory postulates that electrons form Cooper pairs due to an attractive interaction mediated by phonons, resulting in an energy gap of 2Δ in the density of states at the Fermi level E_{F}. These Cooper pairs, which act as bosons, lead to the coherent superconducting behavior observed in conventional superconductors. According to BCS theory, at temperatures below the critical temperature (T_{C}), some electrons might not form Cooper pairs, creating quasiparticles, which are fermions. These elementary excitations can occupy energy states above the superconducting gap. The binding energy of Cooper pairs

2Δ is typically in the range of millielectronvolts (meV), significantly smaller than typical semiconductor bandgaps or the energy of optical photons ($\sim$1 eV). When a superconductor absorbs energy from a photon, Cooper pairs can dissociate into quasiparticles, allowing a single photon to create hundreds or thousands of quasiparticle excitations.

Superconductors possess unique properties that are crucial for a variety of technological applications. When the temperature falls below T_C, superconductors exhibit zero DC resistance, an attractive property for applications that aim to minimize power losses while supporting high current density. The pursuit of highe T_C superconductor is ongoing, with significant implications in fields like physics, medicine, and the energy industry [56–58].

One of the most well-known effects in superconductivity is the tunneling of Cooper pairs between two superconductors separated by an insulator, known as the Josephson effect [59, 60]. This phenomenon was exploited to detect single photons in the IR range with a STJ for the first time in 1996 by Peacock et al. [61]. In superconductors, the transition between the superconducting and normal phases can be very steep, leading to a rapid increase in resistance. Cabrera et al. in 1998 used this sharp transition as the basis of TES operation to discriminate single photons [4].

Similarly, superconductors can maintain their superconducting state until the current density exceeds a critical value, J_C, beyond which the superconducting state collapses, resulting in resistive heating. This principle was used to detect single photon for the first time in 2001 by Gol'Tsman et al. [62] with a SNSPD. Additionally, superconductors exhibit 'kinetic inductance' ($l_k = \frac{m}{n_s e^2} = \mu_0 \lambda_L^2$), which depends on the density of Cooper pairs and varies with current and temperature. In 2003, Day et al. used a KID to exploit changes in kinetic inductance to detect single photons [63].

To better understand the process behind the detection of a single photon in SSPDs, the next section will delve into the energy down-conversion process that occurs after a photon with energy E_0 is absorbed by a superconductor. This section will follow the same scheme presented in [6].

2.1.1 Energy Down-Conversion Process in Superconductors

Superconducting single-photon detectors operate on the principle that even a single photon can break thousands of Cooper pairs, creating non-equilibrium states. When a photon with frequency ν interacts with a superconductor, its energy ($h\nu$) is compared to the superconducting energy gap parameter (Δ). Detection occurs if the photon's energy surpasses the binding energy of Cooper pairs ($h\nu > 2\Delta$). For photons in the visible to infrared range, the ratio $\frac{h\nu}{2\Delta}$ can be approximately 1,000, suggesting that one absorbed photon can generate up to 1,000 quasiparticles.

In superconducting materials, thermal equilibrium consists of three coexisting subsystems: Cooper pairs, quasiparticles, and phonons from the superconductor and the substrate. These subsystems remain in equilibrium when they share the same temperature [64]. External disturbances, such as a photon with sufficient energy ($E_0 = h\nu$), can disrupt this equilibrium [65].

Energy down-conversion following photon interaction typically proceeds through four stages [66], with the evolution of energy and particle density illustrated in Figure 2.1. In the first stage (I), the energy absorbed by the superconductor disrupts the equilibrium within one of the subsystems, resulting in the generation of energetic photoelectrons [67]. This leads to the production of secondary high-energy electrons (hot electrons), where strong electron-electron scattering, characterized by a typical interaction time ($\tau_{\text{e-e}}$), dominates the energy down-conversion process. After several $\tau_{\text{e-e}}$, the hot electrons thermalize to an energy of $E_1 = \hbar\omega_{\text{D}}$ (where ω_{D} is the Debye frequency), marking the conclusion of the first stage.

In the second stage (II), energy down-conversion continues to a second characteristic energy ($E_2 \sim 3\Delta$), where electron-phonon scattering ($\tau_{\text{e-ph}}$) becomes the dominant process, releasing high-energy phonons clustered around the Debye frequency (ω_{D}). At this stage, the quasiparticle population responds rapidly compared to the slower phonon distribution due to the higher scattering rate. The final outcome is a non-equilibrium distribution of high-energy phonons and quasiparticles.

The third stage (III) involves the further evolution of the mixed distribution of quasiparticles and phonons. This stage is characterized by processes such as Cooper pair breaking with phonon absorption, quasiparticle recombination into Cooper pairs with phonon emission, and phonon escape into the substrate. The stage concludes

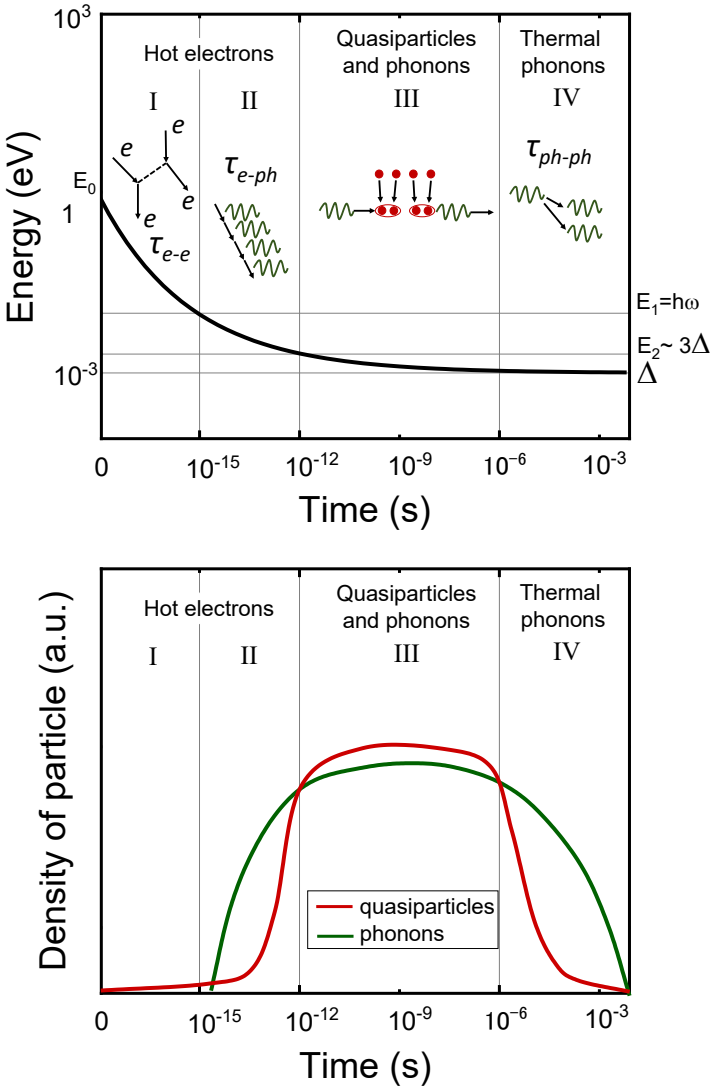

Fig. 2.1 A thermalization scheme that demonstrates the sequential channels of energy transfer and the evolution of subsystem populations in a superconductor as it approaches equilibrium after interacting with an energetic photon of energy E_0 [6]. The cascade of processes is categorized into four stages (I-IV). Stages I and II are dominated by hot electrons generated upon photon absorption, which transfer energy to quasiparticles and phonons during stage III. The final stage, IV, involves the dissipation of energy as thermal phonons. In this qualitative illustration, the photon energy E_0 is approximately 1 eV, which is an order of magnitude greater than the Debye energy $\hbar\omega_D$, and significantly larger than the superconducting energy gap parameter $\Delta \sim 10^{-3}$ eV. The solid line in the top plot represents the energy per particle over time, ranging from E_0 for hot electrons to Δ for quasiparticles. The bottom plot depicts the particle densities over time, with quasiparticles shown in red and phonons in green.

when the energy of the phonons drops below 2Δ, at which point new quasiparticles are no longer generated.

The fourth stage (IV) involves relaxation to a stable state, where phonon-phonon scattering and phonon escape lead to equilibrium at the bath temperature. These stages of energy down-conversion represent the fundamental processes for SSPDs. In the next section, I will describe the working principles of the main SSPDs.

2.2 Superconducting Single-Photon Detector Types

SSPDs encompass a range of technologies, each leveraging the unique properties of superconductivity to detect photons with unprecedented sensitivity. These detectors are distinguished by their operating principles and mechanisms, each excelling in specific figures of merit. The four main types include:

1. **Superconducting Tunnel Junction (STJ)**: The first superconductor-based single-photon detectors, STJs rely on the tunnel current of electrons excited by an incident particle and offer intrinsic energy resolution.

2. **Transition-Edge Sensors (TESs)**: TESs detect photons by measuring resistance changes in a superconducting film operating at its transition temperature, providing exceptional energy resolution.

3. **Superconducting Nanowire Single-Photon Detectors (SNSPDs)**: SNSPDs detect photons via resistive pulses generated upon photon absorption, offering high timing precision and rapid recovery times.

4. **Kinetic Inductance Detectors (KIDs)**: KIDs exploit changes in kinetic inductance due to photon absorption, enabling large-format detector arrays through frequency-division multiplexing.

Below, I will provide a summary of each type, exploring their working principles, characteristics, and key applications.

2.2.1 Superconducting Tunnel Junction

STJ detectors were the first superconductor-based optical single-photon detectors [61]. An STJ consists of two layers of superconducting film separated by a thin insulating barrier (SIS junction), typically on the order of nanometers. This structure forms a Josephson junction, allowing Cooper pairs to tunnel across the insulating barrier, a process known as the Josephson effect [59, 60]. Quasiparticles generated from broken Cooper pairs can also tunnel across the barrier, contributing to the detector's response.

When a photon is absorbed by one of the superconducting electrodes in an STJ, it breaks Cooper pairs, creating excess quasiparticles and phonons [68]. By applying a voltage across the junction, as shown in Figure 2.2, these quasiparticles tunnel to the other electrode, resulting in an excess tunneling current proportional to the photon's energy. This characteristic makes STJs intrinsically energy-resolving detectors. Therefore, this detector relies on the tunneling of quasiparticles generated in the third stage of energy down-conversion discussed in the previous section.

STJs are typically operated at sub-Kelvin temperatures and require a magnetic field to suppress Josephson tunneling of Cooper pairs [61]. The time constant for STJs typically ranges from a few microseconds or less, depending on the area of the electrodes. Since their invention, STJs have found various applications. Since 1999,

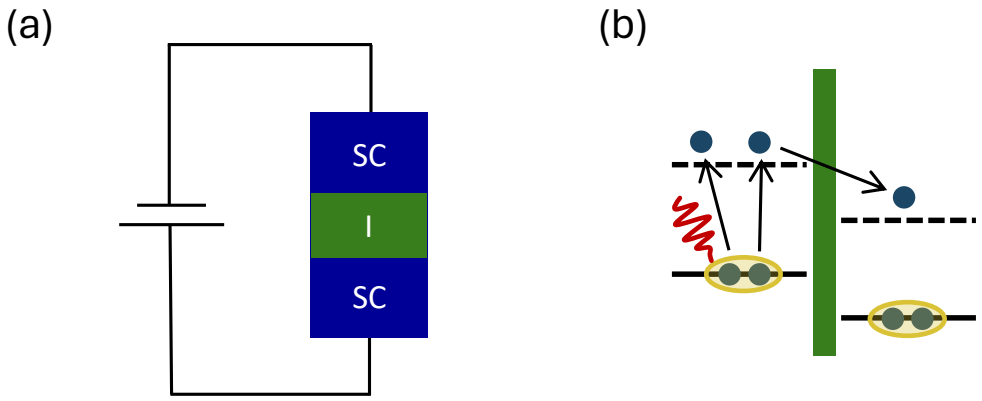

Fig. 2.2 Superconducting Tunnel Junction (STJ) (a) Schematic of a superconductor-insulator-superconductor junction with bias V. (b) The energy diagram of the junction shows the voltage bias shifting the Fermi energies of the two superconductors. Quasiparticles generated from broken Cooper pairs due to photon absorption can tunnel across the barrier.

the European Space Agency (ESA) has operated a superconducting single-photon camera, S-Cam3. This camera features a 10×12 pixel array that operates within a wavelength range of 340 nm to 740 nm, with an average energy resolution of 0.17 eV at 2.4 eV (500 nm) [69]. Table 2.1 presents record performance metrics for STJ devices compared to other detector technologies. Recently, there has been renewed interest in junction-based quantum detectors, with near-IR single-photon detection demonstrated using a graphene-based Josephson junction [70].

The performance of STJs heavily depends on the quality of the insulating barrier, which must be extremely thin, uniform, and free of holes. These stringent requirements make the fabrication of the junctions very challenging. Consequently, the development of alternative superconducting detectors, such as TESs, which are easier to fabricate, has led to a decline in the development of STJ detectors [71].

2.2.2 Transition-Edge Sensors

TES are highly sensitive microcalorimeters used to detect radiation across a wide spectrum, from sub-millimeter wavelengths to gamma rays [2–5]. Their sensitivity is due to the steep resistance change occurring at the superconducting transition. A typical TES designed for optical-IR photons consists of a superconducting film acting as both an absorber and a thermometer. Irwin et al. first proposed the electrothermal feedback mechanism and a Superconducting QUantum Interference Device (SQUID) to read the change in current in the TES due to particle absorption [3] and in the 1998 Cabrera et al. reported on the first optical experiments with TES devices [4].

When photons are absorbed by a TES, their energy is converted into heat, leading to an increase in temperature. The superconducting film, polarized at its superconducting-to-normal transition state, undergoes a significant change in resistance due to this temperature increase. As shown in Figure 2.3, the TES is voltage-biased and in series with an inductor. Any change in current in the TES is detected as a variation of magnetic flux in the inductor by the SQUID and translated into a voltage pulse. TES detectors operate in the sub-Kelvin temperature range and rely on the detection of equilibrium phonons generated in the final stage of energy down-conversion. Although relatively slow, this method provides high photon detection efficiency, along with energy and photon-number resolution [13, 14].

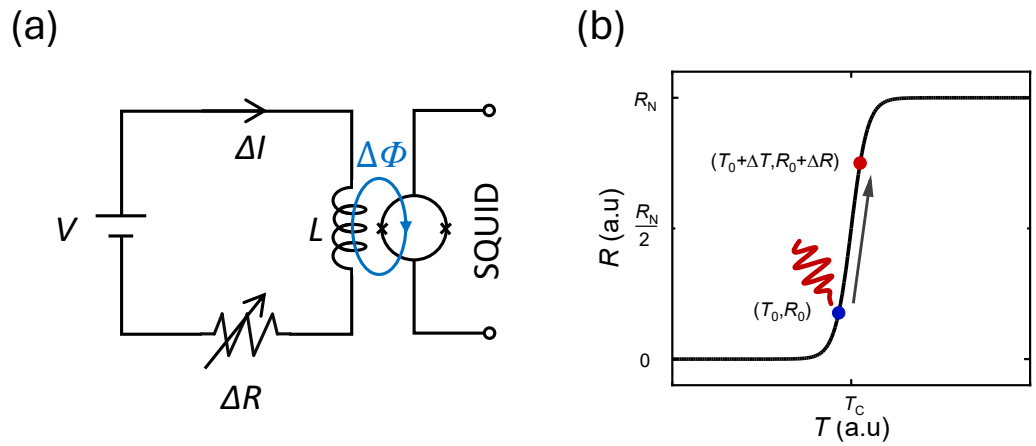

Fig. 2.3 Transition-edge sensor TES (a) Schematic of the circuit where the TES is voltage-biased and in series with an inductance. (b) The TES is polarized on its steep superconducting transition. When a photon is absorbed, the resistance increases, the current I decreases, and the SQUID detects a change in magnetic flux ($\Delta\Phi$) in L.

The high detection efficiency and photon-number resolution make TESs essential components in setups for fundamental physics experiments [45], quantum metrology [72, 73], quantum computation [74], quantum information [75], and dark matter experiments [16, 15].

TES detectors can be multiplexed in both time and frequency domains, enabling large-format detector arrays. Previous implementations in submillimeter astronomy applications have achieved arrays with a few kilo-pixels [76, 77]. However, for optical and near-IR TES detectors, the largest array size to date is a 36-pixel array [78]. As mentioned above, TESs have been used across a wide range of energies and, especially in the last decade, have been extensively studied by the X-ray community, where they were first developed and optimized for high-resolution detection [79, 80].

TESs for X-rays slightly differ from those used for optical photons due to the presence of an absorber, which fully stops X-rays and is connected to the TES that works as a thermometer.

In terms of performance in energy resolution, X-ray TESs have demonstrated impressive results. In [81], an energy resolution of 0.72 eV at 1.5 keV was obtained, and in [82], they achieved below 2 eV at 5.8 keV. These results show that these devices can have a resolving power ($\frac{E}{\Delta E}$) of more than 3000 in the X-ray energy range, which is more than two orders of magnitude higher than what can be achieved for IR photons. Compared to optical TESs, X-ray TESs often need to operate

in large arrays, and for this reason, much more effort is put into achieving better array numbers than optical TESs. An example of a large array readout technique is frequency domain multiplexing (FDM), developed in the framework of Athena X-IFU [83]. A prototype is described in [84].

In Chapter 3, I will further discuss the physics of TES detectors, explaining the electrothermal feedback, how the SQUID is used as a transimpedance amplifier, and the theoretical model behind the metrics of this detector. For now, it is sufficient to know that the pulse generated by the TES detection system upon particle absorption is proportional to the energy released in the substrate. The TES, therefore, has intrinsic energy resolution, making the detector capable of photon-number resolution in the case of fixed photon energy. The energy resolution is proportional to the operating temperature: the lower the temperature, the more enhanced the performance. However, the recovery time of the detector is inversely proportional to the temperature, and thus, often a trade-off is needed between energy resolution and fast recovery time.

2.2.3 Superconducting Nanowire Single-Photon Detectors

SNSPDs are highly sensitive devices that detect photons by rapidly generating a resistive pulse following photon absorption. An SNSPD typically consists of a narrow, very thin superconducting wire, usually 80–200 nm wide and 2–5 nm thick, often patterned in a meandering fashion on a substrate to maximize the active area. The wire is cooled well below its T_C and biased just below its I_C. The detection principle, shown in Figure 2.4, involves the creation of a localized region of broken Cooper pairs upon photon absorption, forming a "hotspot" that disrupts superconductivity, leading to a sudden increase in resistance, before rapidly returning to the superconducting state [62, 85].

SNSPDs operate in the Kelvin/sub-Kelvin temperature range and are known for their fast recovery times, often as short as a few nanoseconds, and exceptionally low timing jitter, reaching a few picoseconds [46, 21]. These properties make SNSPDs ideal for high-speed photon detection and applications requiring precise timing. They are typically made from disordered superconducting materials like NbN, WSi, or MoSi.

An other important feature of SNSPDs is their SDE, which can be higher than 98% [46–48] . The SNSPD design offers significant advantages in terms of noise reduction, as it intrinsically produces a digital pulse, reducing issues related to analog signal processing. The compact and efficient design also facilitates the implementation of SNSPD arrays [86], contributing to their growing use in various quantum applications.

2.2.4 Kinetic Inductance Detectors

KIDs are superconducting single-photon detectors that measure changes in kinetic inductance due to photon absorption in a superconducting material. KIDs consist of a superconducting microwave resonator, designed either as a lumped-element or a distributed system. When a photon is absorbed, it breaks Cooper pairs, generating quasiparticles and causing a change in the kinetic inductance due to the resulting variation in quasiparticle density. This change in kinetic inductance affects the

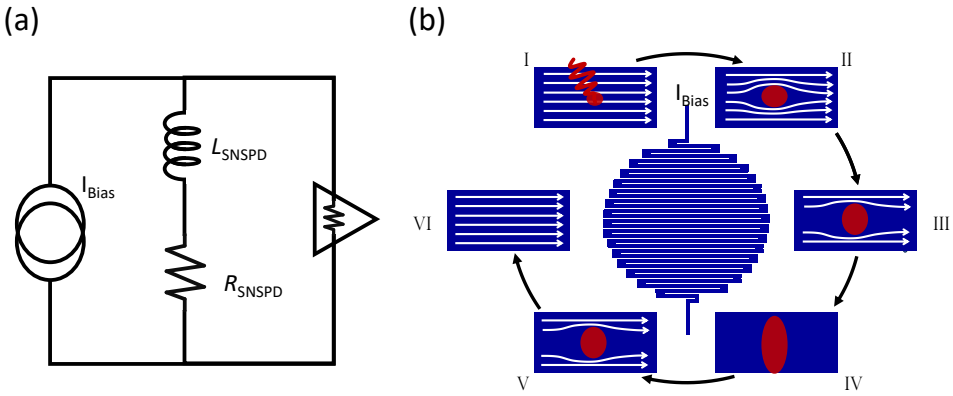

Fig. 2.4 Superconducting Nanowire Single-Photon Detector (SNSPD). (a) Electrical circuit where the SNSPD is current-biased. (b) Detection cycle schematic: The superconducting nanowire, kept below the critical temperature, is DC biased just below the critical current. (i) Absorption of a photon creates a small resistive hotspot. (ii) The supercurrent is diverted around the hotspot, increasing the local current density and exceeding the superconducting critical current density. (iii) This results in a resistive barrier across the nanowire. (iv) Joule heating, due to the DC bias, extends the resistive region until current flow is blocked and the bias current is shunted by the external circuit. (v) The resistive region then subsides, and the nanowire returns to its superconducting state, restoring the bias current to its original value (vi).

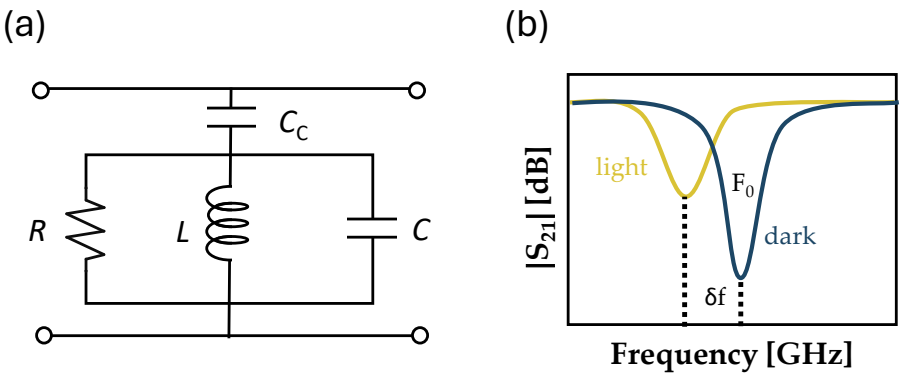

Fig. 2.5 Kinetic Inductance Detector. (a) Schematic of a KID in a resonant circuit where the detector is represented by the inductance. (b) The absorption of a photon changes the inductance, shifting the resonance amplitude.

resonance frequency and internal quality factor (Q) of the resonator, providing the fundamental basis for detection in KIDs.

The alteration in kinetic inductance is usually detected as a shift in the resonant frequency of a microwave resonator, as depicted in Figure 2.5. By analyzing the transmitted microwave signal in terms of its in-phase and quadrature (I-Q) components, it is possible to read out large numbers of Kinetic Inductance Detectors (KIDs) on a single microwave feed line using frequency-division multiplexing [63, 87]. This capability for multiplexing makes KIDs ideal for large-format detector arrays, as each resonator can be individually addressed with a specific microwave tone, allowing multiple detectors to be monitored simultaneously on a single broadband microwave channel [88].

KIDs typically operate in the sub-Kelvin temperature range. Because of frequency-division multiplexing, current KID devices can achieve response speeds of up to 1 kHz, although higher speeds have yet to be demonstrated [89]. KIDs have intrinsic photon-number resolution and energy-resolving capabilities due to their sensitivity to changes in kinetic inductance caused by quasiparticle generation.

Initially developed for millimeter and sub-millimeter wavelength detection in astronomy applications, KIDs have since been extended to include optical and near-infrared detection with large arrays of a few kilopixels for astronomical telescopes [90, 88].

Recent advancements have improved the ability to detect single photons in the near-infrared range. For instance, a group at the National Institute of Standards and Technology (NIST) [91] demonstrated enhanced single-photon counting at a 1550 nm wavelength, resolving up to 7 photons with an energy resolution of approximately 0.22 eV in TiN-based KIDs. Both Hf and PtSi-based KIDs have shown single-photon response at optical and infrared wavelengths [88, 92]. Another significant result in enhancing KID energy resolution was obtained by J. de Visser et al. [93], where they studied the effect of suspending the sensitive part of the detector on a 110-nm-thick SiN membrane, achieving an energy resolution of 0.04 eV at 1545 nm.

2.3 State-of-the-art Performance for TES

In this section, I will present the state-of-the-art performance in the key figures of merit for optical TES with respect to other SSPDs and among different TES devices. As discussed at the beginning of this chapter, the most relevant figures of merit for TES in the optical and IR range are listed here:

- System Detection Efficiency (SDE)
- Energy Resolution (ΔE)
- Photon-Number Resolution (PNR)
- Recovery Time
- Maximum Count Rate (MCR)
- Time Jitter (Δt_σ)
- Dark Count Rate (DCR)
- Number of Pixels in an Array

Table 2.1 summarizes the best performances of TES in these metrics compared to other SSPDs.

Different detector technologies excel in specific metrics, often requiring trade-offs. For example, TESs offer intrinsic photon-number resolution, capable of resolving up to double-digit photon counts, but they may suffer from higher timing jitter and complex readout electronics. In contrast, SNSPDs demonstrate exceptional timing jitter and high maximum count rates, but their photon-number resolving capability is limited.

Achieving high performance in one metric often involves trade-offs in others. For instance, an SNSPD with a record-breaking maximum count rate of 1.5×10^9 counts/s [94] operates at this rate with an efficiency of only 12%. Similarly, an SNSPD that achieved a timing-jitter value of 2.6 ps [21] did so with a narrow, straight segment of nanowire, which can affect optical mode coupling efficiency.

Table 2.1 Figure of merit for different superconducting single-photon detectors in the visible-infrared range

Device	SDE	ΔE	PNR	Recovery Time	MCR	Δt_σ	DCR	N of Pixels
TES	95% (1556 nm) [13] 98% (850 nm) [14]	0.067 eV [17]	55 (1550 nm) [19] 16 (802 nm) [97]	375 ns [22]	2 MHz [22]	30 ns [95] 2 ns (700 nm) [23]	0.36 mHz (0.8-3 eV)[16] 0.1 mHz (1.16 eV)[15]	36 [96]
SNSPD	98% [46, 47] 99.5% [48]	/	7 [98]	400 ps [20]	1.5 GHz [94]	2.6 ps [21]	100 mHz [99] 10 mHz [86]	1024 [86]
STJ	70% (150-600 nm) [10] 20% (1 µm) [10]	0.065 eV [10]	R$\sim$ 14 (500 nm) [10]	100 µs [69]	10 kHz [69]	1 µs [10]	/	120 [69]
KID	17% [90]	0.04 eV [93]	7 (1550 nm) [91] R $\sim$ 8 (400 nm) [90]	400 µs [90]	2.5 kHz	2 µs [90]	/	2024 [90] 20,440 [88]

Achieving high performance across multiple figures of merit is a key objective in the field, but it often necessitates compromises. Consequently, application-specific designs may not require record values for every metric, enabling optimization tailored to specific use cases.

From Table 2.1, we can see that TESs and SNSPDs lead in terms of SDE, while KIDs are more suitable for use in large arrays due to their scalability with high numbers of pixels. SNSPDs are unmatched in terms of speed, operating at high detection rates and capable of functioning at higher temperatures (around 1 K). This has led to the commercialization of SNSPDs, with several companies producing them. However, SNSPDs do not have intrinsic energy resolution or PNR compared to TESs, where the operational principle is based on these properties.

In the following section, I will further discuss the state-of-the-art performances achieved by TESs in these metrics. A summary of the major results obtained for TESs in the optical-IR range can be found in Table 2.2.

2.3.1 System Detection Efficiency (SDE)

SDE for TES is influenced by several factors, including coupling efficiency ($\varepsilon_{\text{coupling}}$), internal efficiency. The Internal efficiency depends on the quantum efficiency (ε_{QE}), which represents the probability of a photon being absorbed once coupled to the active area, and readout efficiency ($\varepsilon_{\text{read-out}}$), which indicates the effectiveness of the detector's electronic signal processing.

SDE can be mathematically expressed as:

$$SDE = \varepsilon_{\text{coupling}} \cdot \varepsilon_{\text{QE}} \cdot \varepsilon_{\text{read-out}} \tag{2.1}$$

In TES detectors, quantum efficiency corresponds to the probability of a photon being absorbed, rather than reflected or transmitted, in the superconducting film. It is enhanced through antireflection (AR) coatings and reflective mirrors to minimize losses [100]. In Figure 2.6 (a), a bare Ti TES is visible at the top, while at the bottom, the same TES is embedded in the AR coating and mirror. The mirror is used together with a spacer to reduce the losses due to transmission forming a cavity and enaching the absorption in the Ti. Figure 2.6 (b) compares the absorption probability of a photon across the optical-IR range. For the bare Ti TES, absorption

remains below 50% throughout the entire range, whereas with the AR coating and mirror, absorption is enhanced above 95% at 930 nm. This approach, using thin-film constructive interference, has proven effective, with reported SDEs of 95% at 1556 nm [13] and 98 % at 850 nm [14].

In those two works, the alignment of the fiber with the active area (high $\varepsilon_{\text{coupling}}$) was obtained with mechanical clamping of the fiber housing [13] and UV-curable resin for adhesion [14]. Nowadays, the same groups use a more effective method consisting of the self-aligning fiber-coupled mounting package designed by Miller et al. [101], also used in SNSPD detectors, which has achieved record SDEs of 98% and 99.5% in the infrared range [46–48]. Alternatives to these methods include fiber arrays assembled on a Si V-groove [102], evanescent coupling through microfibers [103], alignment based on the interference of back-reflected light [104], and another method involving geometric structures on the chip [105]. As shown in Table 2.2, valid SDEs have been obtained with different TES materials such as W [13], Ti [14], TiAu [106], Hf [107], TiAg [108], and Ir [109].

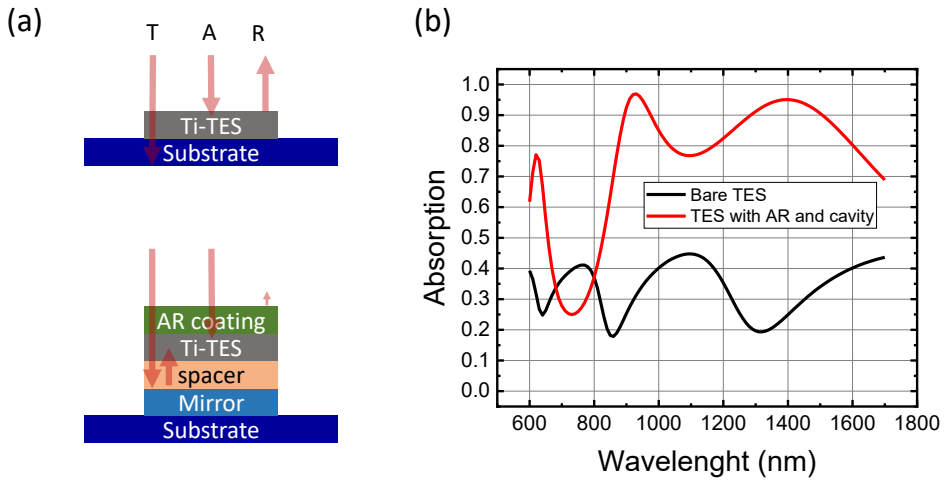

Fig. 2.6 (a) Schematic illustration comparing a bare Ti TES (top) and a Ti TES covered with anti-reflection coating and an optical cavity below (bottom). The cavity is made by having a dielectric spacer under the TES and then a mirror. Some portion of light going to the TES could be transmitted and, by tuning the spacer thickness, it is possible to optimize the absorption of the light in the TES after it is reflected back from the mirror. (b) Comparison of the absorption probability between the bare TES and one with AR coating and optical cavity in the optical-IR range. The AR coating and cavity significantly increase absorption, reaching over 95% at 930 nm.

2.3.2 Dark Count Rate (DCR)

Dark counts in a TES can originate from two primary sources: background counts and intrinsic dark counts. Background counts typically result from blackbody radiation, stray light coupled in the fiber, or high-energy particles, such as cosmic rays. Counts due to stray light can be significantly reduced at telecom wavelengths by tightly coiling the fiber around the device, increasing bend loss for long-wavelength photons compared to shorter signal wavelengths.

In contrast, intrinsic dark counts are those observed even in a perfectly shielded environment. In SNSPDs, intrinsic dark counts increase exponentially as the bias current nears the switching current. Remarkably, shielded SNSPDs have demonstrated exceptionally low dark counts, measuring only 4 to 5 counts over 180 hours of continuous operation at low bias currents [34].

For TES, intrinsic DCR on the order of mHz, making them ideal for applications requiring extremely low background noise, such as dark matter searches. The Quantum Haloscope for Dark Matter Search (QHalos) experiments and The Any Light Particle Search (ALPS II) experiment aim to utilizes TES detectors to identify photons generated by dark photons [16] or axion [15] respectively. In the ALPS experiment they measured intrinsic dark count rates are as low as 0.1 mHz at 1046 nm. When coupled with an optical fiber, the dark count rate was recorded at 8.6 mHz, predominantly due to blackbody photons from the 300 K blackbody spectrum at the other end of the fiber. In the QHalos experiment, with a first TES protopype, an intrinsic DCR of 0.36 mHz was measure for the all region of intrest of 0.8 eV-3 eV as will be discussed in Section 5.3.

2.3.3 Energy Resolution

In the realm of photon detection, the energy resolution often surpasses the performance metrics listed in Table 2.1 sor SSPDs. For instance, a commercial spectrometer's energy resolution depends on the diffraction grating and can reach down to a few millielectronvolts. However, such setups often exhibit low SDE and much higher DCR.

TESs inherently possess excellent energy resolution capabilities, enabling them to discriminate single photons with a resolution as fine as 67 meV [17, 18]. This

intrinsic property makes TESs exceptionally useful for applications requiring high precision in energy measurement, and allows them to achieve photon-number resolution when illuminated with monochromatic light. Recently, this property has also attracted interest in experiments where high energy resolution is required for electron detection. The PonteCorvo Tritium Observatory for Light, Early-Universe, Massive-neutrino Yield (PTOLEMY) project, for instance, requires TESs with excellent energy resolution for electron detection [26, 27]. One of the first challenges to address is to show that TESs can have similar performance with electrons as they do with photons. On this matter we recently submit a paper that shows that in the 100 eV range, this condition is met [110], the results will also be discussed in Section 5.2. Additionally, in the field of electron spectroscopy, TES performance as electron detectors is under investigation at higher energy (up to 2 keV) as showed in [111].

2.3.4 Photon-Number Resolution (PNR)

TES detectors generate an output signal proportional to the cumulative energy of multiple photon absorption events. Figure 2.7 (a) presents histograms of the TES response amplitude when illuminated with photons at 1540 nm (0.8 eV, black) and 1310 nm (0.85 eV, red). The first peak on the left in both histograms represents events where zero photons were detected per pulse. The second peaks correspond to the absorption of a single photon. The one-photon peak at 1310 nm is centered at a higher amplitude than the one-photon peak at 1540 nm, confirming that the TES response is proportional to the energy of the absorbed photon.

Due to their intrinsic energy resolution, TES detectors illuminated with a monochromatic pulsed laser generate a response proportional to the energy of a single photon multiplied by the number of photons in the pulse. Figure 2.7 (a) shows multiple peaks due to multiple photons per pulse, and the output of each detection event can be associated with an integer photon number. The energy resolution of TES detectors, however, is limited to a specific energy range. When the absorption event drives the TES completely into its normal state, the TES reaches its saturation energy. In Figure 2.7 (b), the persistence graph shows the TES response to a pulsed monochromatic laser with a number of photon per pulse that sometimes saturate the TES. Some pulses contain enough photons to saturate the detector, beyond which photon-number resolution deteriorates.

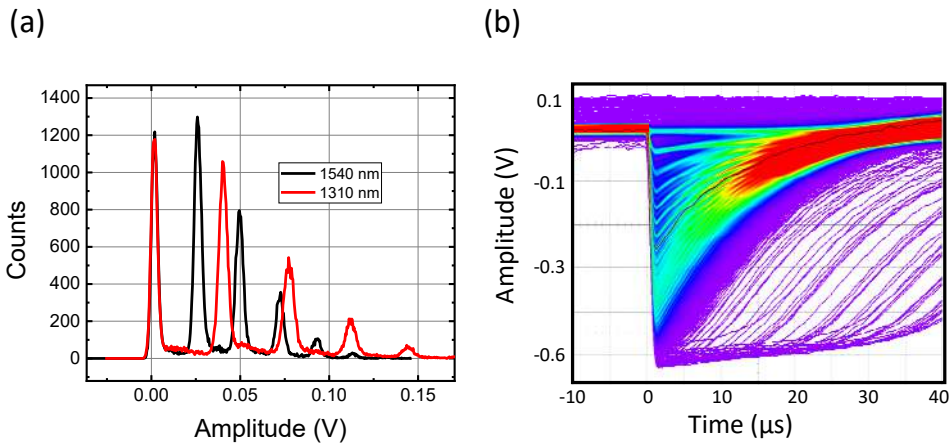

Fig. 2.7 (a) Histogram of the amplitude of the TES response at two different laser wavelengths (1540 nm and 1310 nm). The position of the peaks depends on the photon energy and the number of photons per pulse. (b) Persistence graph of TES response to a pulsed monochromatic laser. Some of the pulses contain enough photons to saturate the TES.

Recent advancements have shown TES devices capable of resolving up to 55 incident photons at 1540 nm [19], making TES an invaluable tool for quantum optics and photon-counting applications. In the field of X-ray detection, [112] demonstrated a TES capable of resolving more than 200 photons with 3 eV energy, showcasing an impressive photon-number resolving power.

2.3.5 Recovery Time

The recovery time of TESs is constrained by the weak thermal link between the electron and phonon systems. While this weak thermal link is vital for converting photons into detectable electrical signals, it results in longer recovery times compared to other single-photon detectors, such as SNSPDs (see Table 2.1) [7]. Notably, during its recovery time, the TES can continue to receive and detect photons, thus exhibiting no dead time, which is a unique feature among photon-counting detectors. However, if a photon is absorbed during the detector's recovery phase, signal pile-up may occur, requiring post-processing analysis of the detector response. Therefore, reducing the recovery time of TES devices is crucial for enabling high-repetition-rate experiments.

It is important to clarify that the metric "recovery time" differs from the rise time constant and the fall time constant typically shown in the literature. As will be de-

tailed in the next chapter, a TES pulse amplitude is proportional to $\left(e^{-t/\tau_+} - e^{-t/\tau_-}\right)$, and typically the fall time constant τ_- is approximated to the effective time constant (τ_{eff}) or the electrothermal feedback time constant (τ_{etf}) [1]. Since by recovery time we mean the time needed for the detector to return to the initial condition, a way to calculate is $5 \cdot \tau_-$. Therefore, the values in both Table 2.1 and Table 2.2 are calculated in this way from the time constant in the relative reference.

Decreasing the recovery time for optical TES detectors is an active area of research, and two approaches are possible to achieve this goal. The response time of the TES in the electron-phonon decoupling limit is inversely proportional to the cube of the operating temperature and independent of the sensor area, as will be detailed in Section 3.5.2. Leveraging the inverse dependence on the cube of the operating temperature, one option is employing superconducting materials with a high T_C, or tuning the transition temperature of a specific material or bilayer to a desired higher T_C. This can significantly accelerate the recovery of a TES detector but also deteriorate the energy resolution. For instance, Kobayashi et al. [22] utilized a TiAu bilayer as the TES superconducting material with a T_C of 314 mK, resulting in a recovery time of 380 ns ($\tau_- = 75$ ns), and an energy resolution of 0.42 eV (fwhm) at 940 nm wavelength. A similar approach is presented in [113] and [114], where with high T_C film they obtain time constants on the order of $\tau_- \sim 150$ ns.

An alternative method to reduce TES recovery time involves introducing a faster heat dissipation path. Calkins et al. [115] and Hummatov et al. [116] demonstrated that by adding Au pads on top of W TES devices, the recovery time was reduced to 1.1 µs ($\tau_- = 220$ ns), showing a significant improvement over devices without Au without changing the operating temperature and maintaining the energy resolution.

2.3.6 Maximum Count Rate (MCR)

As illustrated in Table 2.1 and Table 2.2, the maximum count rate for TES is attributed to the work of Kobayashi et al. [22] with a repetition rate of 2 MHz. This rate assumes the TES fully recovers after five times it fall time constant of 75 ns. Achieving a high counting rate in a TES requires not only minimizing the recovery time but also reducing the readout circuit inductance to decrease the rise time of the pulse. In fact, stabilizing the TES detector against electrothermal oscillations, which may arise from dynamic interactions between heat flow and electrical circuit

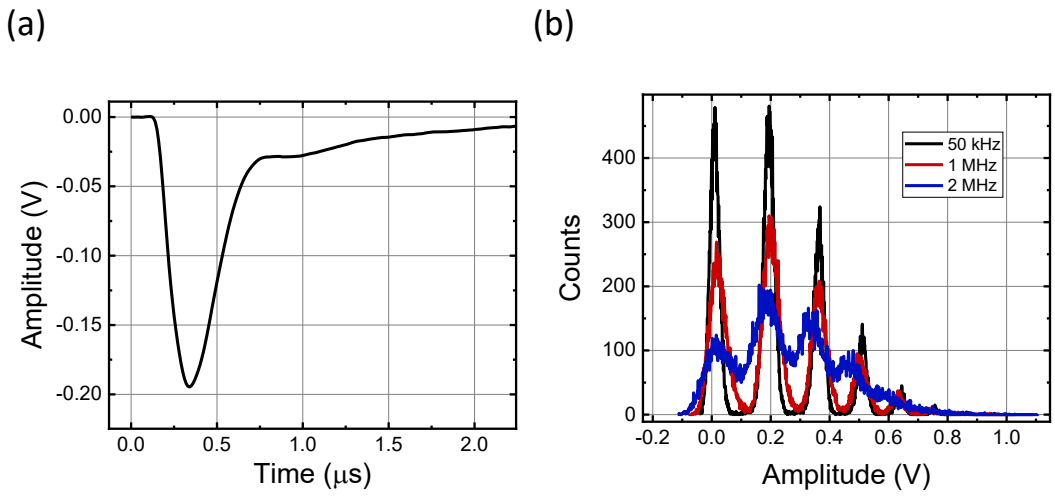

Fig. 2.8 (a) TES pulse with visible electrothermal oscillation in the tail, leading to a recovery time of 250 ns. (b) Histogram of TES counts per three pulse repetition rate. As the repetition rate increases above 1 MHz, the energy resolution deteriorates, making it challenging to resolve peaks.

components, is essential. These oscillations represent energy transfer between the inductor and the TES thermal heat capacity, which can affect detector stability and performance [117].

An example of such oscillations is shown in Figure 2.8 (a), where oscillations are visible at the tail of the pulse. In this case, the recovery time is $\sim 2\mu s$. Increasing the repetition rate of the laser results in a deterioration of the histogram of counts, as visible in Figure 2.8 (b). Especially above 2 MHz, the energy resolution worsens, and it's almost impossible to distinguish between the peaks.

2.3.7 Timing Jitter

Low timing jitter is a crucial performance characteristic for some single-photon detection experiments, as it represents the uncertainty in determining the precise arrival time of a photon [7]. The timing jitter or timing uncertainty for a pulse signal crossing a threshold is determined by the noise and the slope of the signal at the threshold crossing point. One way to overestimate the jitter time for the TES is by measuring the rise time constant, which, as I will discuss in Section 3.5.2, mainly depends on the electrical circuit, with the inductance L playing a crucial role. All

the values for the jitter time Δt_σ in Table 2.2 correspond to the rise time constant reported in the corresponding reference. The only exception is for the work done by Lamas-Linares et al. [23]. In this work, the authors conducted a comprehensive study of the jitter time for a TES and measured a jitter with full width at half maximum (fwhm) values of 4.1 ns for 1550 nm single photons and 2.3 ns for 775 nm photons in W TES devices, without significant degradation of the device's energy resolution (0.33 ± 0.02 eV). The observed lower timing jitter for higher energy photons is attributed to the higher amplitude of the TES output waveform.

Table 2.2 Figure of Merit for Different TESs

Ref	Material	T_C mK	λ nm	Efficiency %	ΔE_{fwhm} eV	PNR	Recovery time µs	Δt_σ ns	MCR Hz	DCR mHz	Active Area µm^2
[96]	W	80	850	9.7	/	/	300	100	10^4	/	**(18x18)x36 pixels**
[13]	W	100	1556	**95**	0.29	7	4	/	/	100	25x25
[14]	Ti	300	850	**98**	0.42	7	0.5	30	10^5	/	10x10
[115]	W	80	/	/	0.24	5	2.3	/	/	/	25x25
[118]	TiAu	100	1570	< 4.1	0.18	29	/	/	10^4	/	10x10
[113]	TiAu	300	1550	50	0.26	13	0.93	176	$5{\cdot}10^5$	100	10x10
[18]	TiAu	106	1550	30	0.113	5	/	/	/	/	10x10
[23]	W	100	775	/	0.33	4	3.8	**2**	10^5	/	/
[114]	Ti	**470**	1550	/	0.12	/	0.77	145	$5{\cdot}10^5$	/	1x1
[15]	W	80	1064	23	/	/	7.7	/	/	0.1	25x25
[112]	MoAu/Bi	75	405	/	0.7-1	**200**	/	/	/	/	120x120
[22]	TiAu	300	940	83	0.21	/	**0.38**	74	$\mathbf{2 \cdot 10^6}$	/	8x8
[97]	W	80	/	/	/	16	10	/	10^4	0.06	25x25
[17]	TiAu	115	1550	60	**0.067**	4	23	/	/	/	8x8
[116]	W	80	/	/	0.274	4	1.1	/	10^6	/	15x15
[19]	TiAu	95	1550	46	0.19	55	315	/	/	/	20x20
[108]	TiAg	190	1550	51	0.17	24	3.5	/	/	/	8x8
[16]	TiAu	90	1540-390	/	0.2	8	5	/	/	**0.36**	20x20
[110]	TiAu	83	406 nm	/	0.8-1.8	40	50	100	/	/	100x100

Chapter 3

Transition-Edge Sensors

Transition-edge sensors (TESs) are superconducting single-photon detectors with intrinsic energy resolution, allowing for photon-number resolution. Their functionality relay on the steep resistance change occurring at the superconducting transition, controlled via electrothermal feedback mechanisms to achieve exceptional sensitivity. This chapter explores the complex mechanisms underpinning TES operations, examining their electrothermal dynamics, and the resulting implications for the detector energy resolution and time properties.

The initial section introduces the fundamental thermal model of a superconductor, emphasizing the weak thermal link between the electron state and the thermal bath. Following this, the discussion shifts to the principles of electrothermal feedback, highlighting its pivotal role in enhancing sensor performance and stabilizing the TES at its superconducting transition. Integration with Superconducting Quantum Interference Device (SQUID) electronics is also detailed, clarifying how these sensors translate changes in TES current into electrical signals for readout.

The chapter further evaluates the theoretical performance limits of TES, concentrating energy resolution, and timing properties—crucial parameters that delineate the operational capabilities of these sensors. Through an extensive examination of these elements, this chapter aims to enhance the reader's understanding of TES technology, its operation, and the critical aspects to focus on for improving its performance in scientific research and practical applications.

3.1 Thermal Model of a Superconductor Coupled to a Thermal Bath

Below temperatures of one kelvin, a superconductor can be described by two independent systems: the electron and the phonon systems [1]. When coupled to a thermal bath, the thermal model is as shown in Figure 3.1. This model identifies the two components within the superconductor: the electronic (e) and the phonon (ph) systems, each characterized by its own temperature, T_e and T_{ph}. The thermal conductance between these sections is represented by $g_{e\text{-}ph}$, which enables heat transfer between them. Another thermal conductance, $g_{ph\text{-}sub}$, connects the phonon component to the substrate, which is then coupled to the cooling bath at temperature T_{bath} via $g_{sub\text{-}bath}$. The thermal conductance $g_{e\text{-}ph}$ is significantly lower than both $g_{ph\text{-}sub}$ and $g_{sub\text{-}bath}$, creating a bottleneck that restricts the rate at which heat from the electrons is transferred to the bath. When the superconductor absorbs energy, its electronic component heats up, leading to an increase in T_e. This heat is gradually transmitted to the thermal bath through the phonon system, allowing the

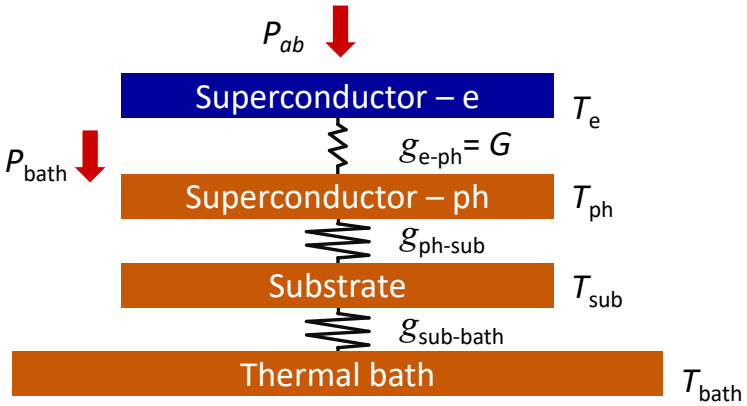

Fig. 3.1 Thermal model of a superconductor coupled to a thermal bath. The model identifies two primary components within the superconducting material: the electronic (e) and phonon (ph) systems, each with its own temperature, T_e and T_{ph}, respectively. The electron-phonon interaction is characterized by a thermal conductance, $g_{e\text{-}ph}$, which facilitates heat transfer between the two systems. Another thermal conductance, $g_{ph\text{-}sub}$, connects the phonon system to the substrate, which is coupled to the cooling bath at temperature T_{bath} through the conductance $g_{sub\text{-}bath}$. At temperatures below 1 K, the electron-phonon thermal conductance, $g_{e\text{-}ph}$, becomes the bottleneck for heat transfer to the bath, limiting the rate of cooling of the electronic system.

superconductor to revert to its baseline temperature. The duration of this process is governed by $\tau_{\text{th}} = \frac{C}{G}$, where τ_{th} denotes the thermal time constant, C represents the heat capacity of the superconductor, and G is the thermal conductance, which primarily depend on $g_{\text{e-ph}}$ below 1 K. By analyzing the thermal power balance, we can observe the temporal evolution of the superconductor's temperature as:

$$C\frac{\mathrm{d}T}{\mathrm{d}t} = P_{\text{ab}} - P_{\text{bath}} \tag{3.1}$$

where P_{ab} signifies any external power absorbed by the superconductor, and P_{bath} is the power the superconductor dissipates to the thermal bath. If the superconductor's temperature is proximal to that of the bath, the heat transfer through conductance G is modeled as:

$$P_{\text{bath}} = G(T(t) - T_{\text{bath}}) \tag{3.2}$$

Substituting P_{bath} into the thermal power balance equation and solving for $T(t)$ yields:

$$T(t) = T_{\text{bath}} + \Delta T(t), \quad \text{where} \quad \Delta T(t) = \Delta T_0 e^{-\frac{t}{\tau_{\text{th}}}} \tag{3.3}$$

This expression outlines the exponential decay of the temperature deviation, ΔT_0, back to the bath temperature, governed by the thermal time constant τ_{th}.

So far, I have outlined the dynamics of thermal variation in a superconductor when it absorbs energy, resulting in a rapid increase in temperature followed by a return to equilibrium. However, I have not yet highlighted why a superconductor can be used as a sensitive sensor. The steep transition from the superconducting to the normal state at the critical temperature of a superconductor is such that even small changes in temperature can significantly affect its electrical resistance, as illustrated in Figure 3.2(a). This property underpins the functionality of superconducting films as TES. To fully leverage this sensitivity, it is important to discuss the concept of electrothermal feedback (ETF), introduced by Irwin in 1995 [3]. This methodology involves the direct injection of electrical power (Joule heating) into the electronic component of the superconductor. By exploiting the weak thermal link, it is feasible to warm up the electronic component temperature such that $T_{\text{e}} \sim T_{\text{C}}$, while maintaining the phonon system, the substrate, and the thermal bath at much lower

temperatures. Consequently, external heat derived from photon absorption is directly transduced into an electrical signal by the sensor, mitigating the loss of heat through the phonon system.

3.2 Optimizing TES Performance with Electrothermal Feedback

The ability of TES detectors to detect single quanta of energy relies on the steep superconducting transition of a metallic film and the exploitation of electrothermal feedback (ETF). Figure 3.2 (a) illustrates the superconducting transition, while Figure 3.2 (b) shows the TES employing electrothermal circuit of the TES.

The TES is voltage-biased and characterized by its heat capacity (C), electrical resistance (R), and a temperature (T) that exceeds that of the thermal bath due to Joule heating. The thermal link connecting the TES to the substrate's phonon system is defined by thermal conductance (G). Both the phonons of the superconductor and the substrate maintain the temperature of the thermal bath (T_{bath}). When a voltage (V) is applied to the TES within an electrical circuit, the resultant current (I) produces heat, elevating the temperature of the TES.

The balance of power within this system is captured by the following equations:

$$C\frac{dT}{dt} = -P_{\text{bath}} + P_{\text{J}} = -\kappa(T^n - T_{\text{bath}}^n) + I^2R(T) \tag{3.4}$$

At equilibrium, where $\frac{dT}{dt} = 0$, the equation simplifies to:

$$\kappa(T^n - T_{\text{bath}}^n) = I^2R(T) \tag{3.5}$$

Here, P_{bath} represents the power dissipated through the substrate's thermal link, governed by the thermal exponent n (typically between 4 and 6) and the thermal coupling constant κ, with the thermal conductance G defined by [1]:

$$G = \kappa n T^{n-1} \tag{3.6}$$

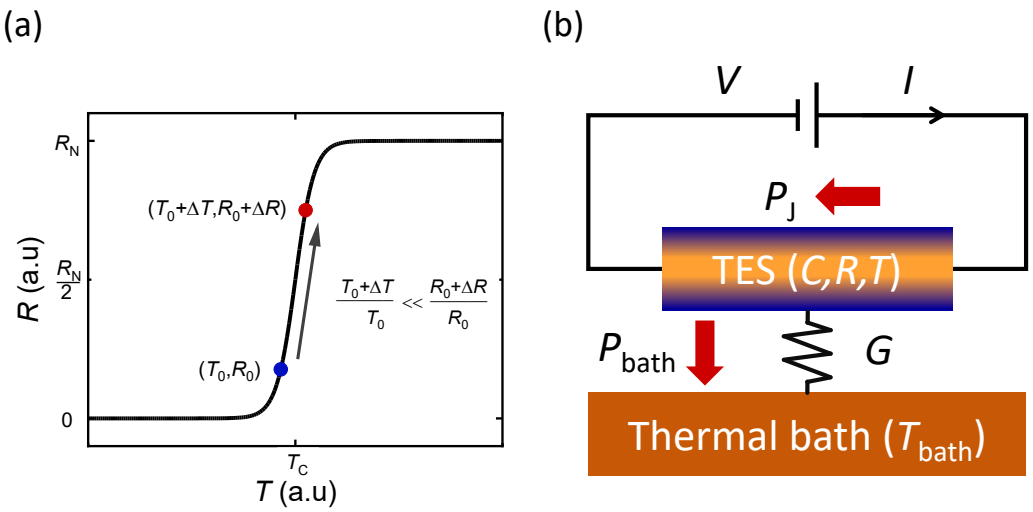

Fig. 3.2 (a) Resistance transition of a superconductor, showing the normal-state resistance (R_N) and the critical temperature (T_C), where the resistance is $R_N/2$. The TES is polarized on the transition at (R_0, T_0), a temperature change ΔT implies a significant change ΔR. (b) Electrical bias circuit of TES utilizing electrothermal feedback.

The term $P_J = I^2 R(T)$ denotes the Joule heating effect. These equations effectively describe the steady-state behavior of the TES, assuming no photon absorption occurs.

Upon the absorption of a photon by the TES, a rapid increase in temperature occurs. The energy of a typical infrared photon is around 1 eV, which corresponds to approximately 0.1 aJ. Given that the heat capacity of a TES could be limited to 1 aJ/mK, the absorption of one IR photon can raise its temperature by approximately 0.1 mK. Consequently, I can consider minor temperature deviations from the stable state, represented by $T = T_0 + \Delta T$. Initially, I assume the resistance R depends solely on temperature T, but later in Section 3.4, I will expand the analysis to include the dependence on current.

Expanding the differential equation 3.4 to the first order in ΔT yields:

$$C\frac{d\Delta T}{dt} = -\kappa(T^n - T_{\text{bath}}^n) + I^2 R - n\kappa T^{n-1}\Delta T - I^2 \frac{dR}{dT}\Delta T \tag{3.7}$$

Given that, according to Eq. 3.5, the first two terms cancel out at equilibrium, I define the temperature sensitivity at constant current as:

$$\alpha \equiv \frac{T}{R}\frac{\partial R}{\partial T}\bigg|_I, \tag{3.8}$$

Considering Eq. 3.6, I simplify the differential equation as follows:

$$\frac{d\Delta T}{dt} = -\left(\frac{G}{C} + \frac{\alpha I^2 R}{TC}\right)\Delta T \tag{3.9}$$

The solution to this equation is an exponential decay of the temperature deviation over time:

$$\Delta T(t) = \Delta T_0 e^{-\frac{t}{\tau_{\text{etf}}}} \tag{3.10}$$

Here, τ_{etf} represents the ETF recovery time constant, characterizing the exponential decay of ΔT:

$$\tau_{\text{etf}} = \left(\frac{G}{C} + \frac{\alpha I^2 R}{TC}\right)^{-1} = \frac{\tau_{\text{th}}}{1+\frac{\alpha I^2 R}{GT}} = \frac{\tau_{\text{th}}}{1+\mathscr{L}}, \tag{3.11}$$

This time constant determines how the TES returns to thermal equilibrium after photon absorption when operated in ETF. This calculation indicates that τ_{etf} can be significantly shorter than the thermal recovery time $\tau_{\text{th}} = C/G$, depending on the value of the loop gain $\mathscr{L}$, defined as:

$$\mathscr{L} \equiv \frac{\alpha I^2 R}{GT}, \tag{3.12}$$

This loop gain, $\mathscr{L}$, plays a critical role in the dynamics of electrothermal feedback, affecting how swiftly the TES system responds to a disturbance, such as the absorption of a photon, and subsequently returns to its steady state.

The efficiency of energy transfer from a photon (E_γ) to the electron system is less than one, I incorporate the efficiency factor ε, representing the fraction of photon energy converted to thermal energy in the electron system. This adjustment modifies the expression for the temperature change:

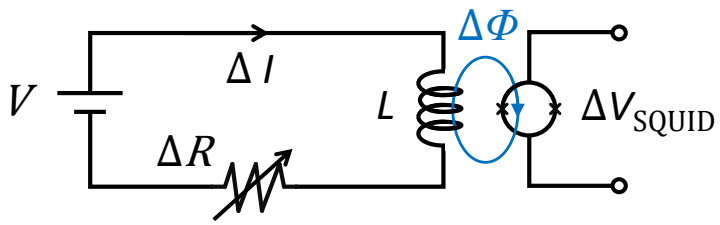

Fig. 3.3 Circuit diagram showing a TES in series with an inductance, coupled with a dc-SQUID. Any change in the current through the TES generates a corresponding change in magnetic flux, which is coupled to the SQUID via the inductance.

$$\Delta T(t) = \varepsilon \frac{E_\gamma}{C} e^{-\frac{t}{\tau_{\text{etf}}}} \tag{3.13}$$

In the case of strong ETF, where $T_{\text{bath}} \ll T$, the loop gain can be simplified as as follows:

$$P_{\text{bath}} = \frac{G}{nT^{n-1}} \left(T^n - T_{\text{bath}}^n\right) \approx \frac{GT}{n} = I^2 R \tag{3.14}$$

This approximation allows to express the loop gain $\mathscr{L}$ as:

$$\mathscr{L} \approx \frac{\alpha}{n} \tag{3.15}$$

Consequently, Eq. 3.11 can be further simplified to:

$$\tau_{\text{etf}} \approx \frac{\tau_{\text{th}}}{1 + \frac{\alpha}{n}} \tag{3.16}$$

Given that n typically ranges between 4 and 6 and considering that α can attain much higher values, in the regime of strong ETF the ETF recovery time constant can be further simplified to:

$$\tau_{\text{etf}} \approx \frac{n}{\alpha} \tau_{\text{th}} \tag{3.17}$$

ETF not only enhances the recovery of TESs but also stabilizes their operation and facilitates the readout of signals. The resistance change within a TES—and consequently the change in current—is proportional to the absorbed energy. Given

the low impedance of TES, it is crucial to pair them with an amplifier such as a Superconducting QUantum Interference Device (SQUID) to effectively detect resistance changes. SQUIDs convert variations in magnetic flux, caused by changes in current through an inductor in series with the TES, into measurable voltage signals. This conversion process is illustrated in Figure 3.3. A detailed examination of the SQUID electronics is essential to fully understand this amplification process.

3.3 Dc-SQUID as a Transimpedance Amplifier in TES Signal Readout

The Superconducting QUantum Interference Device (SQUID) is highly sensitive to changes in magnetic flux and converts these changes into measurable voltage signals. It consists of a superconducting loop containing two Josephson junctions. These junctions appear at the boundary between two superconductors, separated by an insulating layer that allows Cooper pairs to tunnel through, as shown in panel (a) of Figure 3.4. The phenomenon of tunneling Cooper pairs was first predicted by Brian D. Josephson in 1962 [59], resulting in a supercurrent (I_s) that is mathematically described by:

$$I_s = I_0 \sin(\phi) \tag{3.18}$$

where I_0 represents the critical supercurrent, and ϕ is the phase difference across the superconductors' wavefunctions. The relationship between the phase evolution and the voltage (V) across the junction follows as:

$$\frac{d\phi}{dt} = \frac{2\pi V}{\Phi_0} \tag{3.19}$$

Where $\Phi_0 = \frac{h}{2e}$ is the magnetic flux quantum, h is Plank constant and e the elementary charge. This fundamental constant bridges quantum mechanics and electromagnetism.

As current flows through the SQUID, it splits equally between the two junctions. The total critical current of the SQUID is therefore twice that of a single junction. Under no external magnetic flux, the superconducting wavefunction across the loop

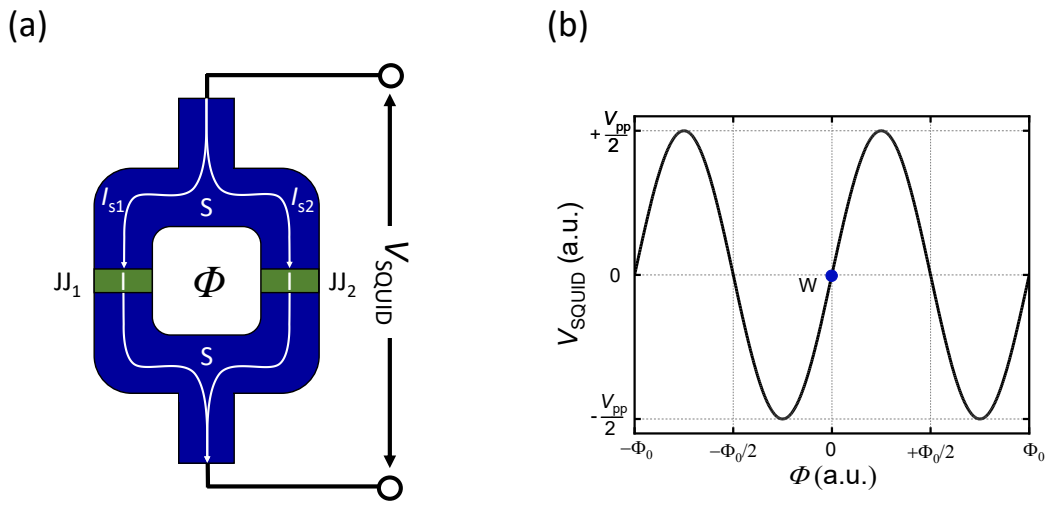

Fig. 3.4 Panel (a) is a schematic of a SQUID highlighting the placement of Josephson junctions (JJ_1 and JJ_2) within the superconducting loop. Panel (b) shows the modulation of voltage across the SQUID (V_{SQUID}) due the variation of magnetic flux (Φ) in the superconducting loop of panel (a).

maintains a uniform phase. However, when exposed to a magnetic field while biased below its critical current, the SQUID generates a screening current to counteract the applied flux, disrupting this symmetry.

The additional screening current adjusts as the magnetic field increases, reaching a threshold where it drives one junction into a normal (non-superconducting) state. This continues until a flux quantum penetrates the loop, resetting the superconductivity of the junctions. The SQUID's response to magnetic flux is thus periodic with a period of one flux quantum, illustrated in Figure 3.4 (b). The device's voltage output linearly correlates with the applied magnetic field over a wide range, enabling precise measurement of even minute flux changes.

3.3.1 Flux-Locked Loop Mode for SQUID Operation

To utilize a SQUID as a current sensor, it must be integrated into an appropriately designed circuit. This setup involves biasing the SQUID and extracting readable voltage outputs corresponding to the TES currents. A schematic of such a read-out is presented in Figure 3.5, which includes the SQUID, the TES input circuit, feedback

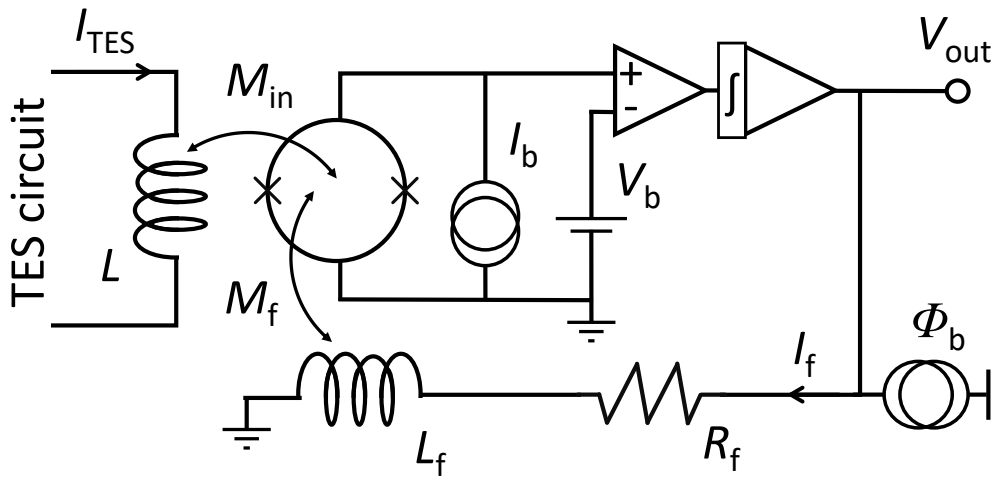

Fig. 3.5 Schematic of the Flux-Locked Loop (FLL) mode in SQUID operation, showcasing the TES circuit integration. The diagram highlights the inductive coupling via mutual inductances M_{in} and M_f, and the feedback system used to stabilize and enhance the SQUID's response to changes in TES current (I_{TES}). The feedback loop actively adjusts the magnetic flux to maintain the SQUID at its optimal working point.

loop, bias sources, and additional electronic components essential for the read-out process.

The TES circuit, incorporating an input coil (L), is inductively coupled to the SQUID. The current flowing through this coil (I_{TES}) generates a magnetic flux (Φ_{in}) coupled to the SQUID. This coupling effect depends on the geometric arrangement and proximity of the coil to the SQUID and is quantitatively described by the inverse mutual inductance ($1/M_{in}$), .

$$\frac{1}{M_{in}} = \frac{\delta I_{TES}}{\delta \Phi_{in}} \tag{3.20}$$

The feedback circuit includes a feedback resistor (R_f) and an inductance(L_f) inductively linked to the SQUID. The strength of this inductive coupling is characterized by the mutual inductance (M_f):

$$\frac{1}{M_f} = \frac{\delta I_f}{\delta \Phi_f} \tag{3.21}$$

where I_f represents the feedback current and Φ_f the magnetic flux generated in the feedback coil. The feedback loop is such that any signal generated by the input is directed back to the SQUID, providing negative feedback that serves to linearize the SQUID's response and extend its dynamic range. Operating in flux-locked loop (FLL) SQUID is locked in the working point W shown in Figure 3.4 (b) to enhances the stability and accuracy of the SQUID. The DC bias current (I_b) is applied to bias the SQUID, ensuring proper modulation of the V-Φ curve. The voltage bias (V_b) creates a voltage offset, adjusting the operating point along the voltage axis (y-axis) in Figure 3.4. The working point is chosen such that the V-Φ curve is around its inflection point at the intercept with the flux axis (x-axis), ensuring maximum sensitivity. The magnetic flux bias (Φ_b), applied as a current source, modulates the flux through the feedback loop. This compensates for changes in flux due to the input inductance, maintaining the SQUID at a consistent working point.

When a change in TES current occurs, it generates a corresponding change in magnetic flux $\delta\Phi$ through the SQUID loop. This change in flux induces a voltage across the SQUID, the resulting voltage is then amplified and integrated before being fed back to the SQUID through the feedback loop. The output voltage in FLL mode δV_{out} is thus proportional to the feedback current δI_f, multiplied by the feedback resistance R_f. Due to the negative feedback mechanism, the feedback flux change $\delta\Phi_f$ balances out the initial flux change $\delta\Phi$ caused by the TES current. This relationship is expressed by:

$$\delta\Phi_f = \frac{\delta V_{out}}{R_f M_f^{-1}} \equiv \delta\Phi \tag{3.22}$$

Combining Equations 3.20 and 3.22, the relationship between the TES current change and the output voltage is:

$$\delta V_{out} = \delta I_{TES} \frac{R_f M_f^{-1}}{M_{in}^{-1}} \tag{3.23}$$

By fine-tuning these parameters, the SQUID is able to accurately amplify the TES current changes into voltage outputs, enabling high-precision current measurements crucial for TES applications. The SQUIDs utilized in this research, known for their precision and reliability, are the result of sophisticated design and fabrication processes at Physikalisch-Technische Bundesanstalt (PTB) of Berlin, and are detailed

in the work by Drung et al. [119]. The electronics to opertate the system, from the TES current bias to the SQUID feedback loop is providede by Magnicon, a PTB spinoff company [120].

3.4 Comprehensive Analysis of Photon Absorption Dynamics in TES

With the principles of electrothermal feedback from Section 3.2 and the basics of SQUID operation in FLL mode from Section 3.3 explained, I shift focus to their practical application: the detection of a single photon.

The comprehensive circuit for TES operation and readout is shown in Figure 3.6. Experimentally, the TES is voltage biased with a current source parallel to a shunt resistor, as illustrated in Panel (a). For effective voltage biasing of the TES, the shunt resistance (R_{sh}) must be significantly lower than the TES resistance (R_{TES}) ($R_{\mathrm{sh}} \ll R_{\mathrm{TES}}$). Here, R_{par} represents the parasitic resistance, which could arise from wiring and connections. Thus, in the Thevenin equivalent with the voltage generator (panel (b)), the load resistance (R_L) is the sum of R_{sh} and R_{par}.

Using the chapter by Irwin and Hilton in "Cryogenic Particle Detection" by Ch. Enss [1] as a reference for this section, the TES thermal and electrical system response is described by the two differential equations:

$$C\frac{dT}{dt} = -P_{\mathrm{bath}} + P_{\mathrm{J}} + P_{\mathrm{inc}} \tag{3.24}$$

$$L\frac{dI}{dt} = V - IR_L - IR(T,I) \tag{3.25}$$

Equation 3.24 governs the thermal circuit, as shown in Figure 3.2 (b), and Equation 3.25 dictates the electrical behavior depicted in Figure 3.6 (a). These equations contain nonlinear terms that can be linearized for small deviations from the steady-state, denoted as R_0, T_0, and I_0, where the conductance and heat capacity are considered constant. For the power flow to the substrate, a power-law dependency is assumed and expanded around T_0 for small signals:

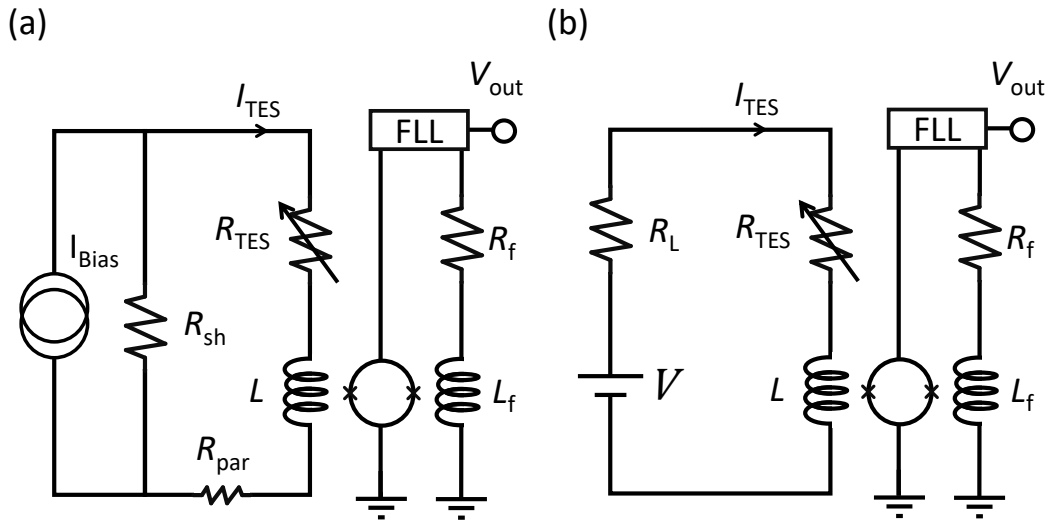

Fig. 3.6 The complete TES and SQUID circuit (a) and its Thevenin equivalent (b), the bias is applied using a current source (I_{Bias}) and a shunt resistor (R_{sh}) in parallel to the TES. Inductance (L) couples the TES to the SQUID electronics, detailed in Figure 3.5.

.

$$P_{\text{bath}} = \kappa(T^n - T_{\text{bath}}^n) \approx P_{\text{bath0}} + G\delta T \tag{3.26}$$

where $G = n\kappa T^{n-1}$ and $\delta T = T - T_0$. In steady state:

$$P_{\text{bath0}} = P_{e0} + P_0 = I_0^2 R_0 + P_0 \tag{3.27}$$

where P_0 is the steady-state signal power. Unlike the simplified model in Section 3.2, where the TES resistance was considered primarily temperature-dependent, I now extend the analysis to account for the resistance's dependence on both temperature an current. The resistance of the TES in the small-signal limit is expanded as:

$$R(T,I) \approx R_0 + \left.\frac{\partial R}{\partial T}\right|_{I_0} \delta T + \left.\frac{\partial R}{\partial I}\right|_{T_0} \delta I \tag{3.28}$$

Here I recall the temperature sensitivity α from Eq. 3.8 and I define current sensitivity β:

$$\beta \equiv \frac{I_0}{R_0} \left. \frac{\partial R}{\partial I} \right|_{T_0}, \tag{3.29}$$

this allow Equation 3.28 to be rewritten in terms of α and β:

$$R(T,I) \approx R_0 + \alpha \frac{R_0}{T_0} \delta T + \beta \frac{R_0}{I_0} \delta I, \tag{3.30}$$

and so expand the Joule power to first order around the steady-state values R_0, T_0, and I_0:

$$P_{\mathrm{J}} = I^2 R \approx I_0^2 R_0 + 2 I_0 R_0 \delta I + \alpha \frac{P_{\mathrm{J0}}}{T_0} \delta T + \beta \frac{P_{\mathrm{J0}}}{I_0} \delta I. \tag{3.31}$$

This enables to express the system's differential equations as:

$$\frac{d\delta I}{dt} = -\frac{R_L + R_0(1+\beta)}{L} \delta I - \frac{\mathscr{L} G}{I_0 L} \delta T + \frac{\delta V}{L}, \tag{3.32}$$

$$\frac{d\delta T}{dt} = \frac{I_0 R_0 (2+\beta)}{C} \delta I - \frac{1-\mathscr{L}}{\tau_{\mathrm{th}}} \delta T + \frac{\delta P}{C}, \tag{3.33}$$

where δI, δP, and δV represent small deviations in current, power, and voltage from their steady-state values I_0, P_0, and V_0, respectively. In this experssion appear again the loop gain $\mathscr{L}$ defined in Eq.3.12 in Section 3.2.

Following the solution approach presented in [1] and applying the Lindeman method from [121], I present the time-dependent solutions for $\delta I(t)$ and $\delta T(t)$. For a TES response to a delta-function temperature impulse at $t = 0$, the solutions are:

$$\delta I(t) = \left(\frac{\tau_I}{\tau_+} - 1 \right) \left(\frac{\tau_I}{\tau_-} - 1 \right) \frac{C \delta T}{(2+\beta) I_0 R_0 \tau_I^2} \frac{\left(e^{-\frac{t}{\tau_+}} - e^{-\frac{t}{\tau_-}} \right)}{\left(\frac{1}{\tau_+} - \frac{1}{\tau_-} \right)}, \tag{3.34}$$

$$\delta T(t) = \left(\left(\frac{1}{\tau_I} - \frac{1}{\tau_+} \right) e^{-\frac{t}{\tau_-}} + \left(\frac{1}{\tau_I} - \frac{1}{\tau_-} \right) e^{-\frac{t}{\tau_+}} \right) \frac{\delta T}{\left(\frac{1}{\tau_+} - \frac{1}{\tau_-} \right)}. \tag{3.35}$$

These equations are valid for $t \geq 0$. From these solutions, it can be identified that the current response of the TES is proportional to $\left(e^{-t/\tau_+} - e^{-t/\tau_-}\right)$, where τ_+ and τ_- are the "rise time" and "fall time", respectively. The time constants are given by [1]:

$$\frac{1}{\tau_\pm} \equiv \frac{1}{\tau_{\text{el}}} + \frac{1}{2\tau_I} \pm \frac{1}{2}\sqrt{\left(\frac{1}{\tau_{\text{el}}} - \frac{1}{2\tau_I}\right)^2 - 4\frac{R_0}{L}\frac{\mathscr{L}(2+\beta)}{\tau_{\text{th}}}}. \tag{3.36}$$

In the expression above I have use the electrical time constant and the current-biased constant defined as follow:

$$\tau_{\text{el}} = \frac{L}{R_L + R_0(1+\beta)}, \tag{3.37}$$

$$\tau_I = \frac{\tau_{\text{th}}}{1-\mathscr{L}}. \tag{3.38}$$

If the rise and fall time constants $\tau_\pm$ are real, the solution of Equation 3.34 is critically damped or overdamped. If they are complex, the response is underdamped; if the real part is negative, the response is unstable.

When L is sufficiently small such that $\tau_+ \ll \tau_-$, then the time constant can be approximated to:

$$\tau_+ \approx \tau_{\text{el}} = \frac{L}{R_L + R_0(1+\beta)}, \tag{3.39}$$

$$\tau_- \approx \tau_{\text{th}} \frac{1+\beta+\frac{R_L}{R_0}}{1+\beta+\frac{R_L}{R_0}+\left(1-\frac{R_L}{R_0}\right)\mathscr{L}} = \tau_{\text{eff}}. \tag{3.40}$$

In case of strong ETF, meaning that the TES is voltage bias ($R_{\text{L}} \ll R_0$) and $T_{\text{bath}} \ll T_0$ then the following simplification are possible :

$$P_{\text{bath}} = \frac{G}{nT_0^{n-1}}\left(T_0^n - T_{\text{bath}}^n\right) \approx \frac{GT_0}{n} \rightarrow \mathscr{L} \approx \frac{\alpha}{n} \gg \beta, 1 \tag{3.41}$$

and Eq. 3.40 is futher simplified to:

$$\tau_{\text{eff}} \approx \frac{\tau_{\text{th}}}{1+\frac{\alpha}{n}} = \tau_{\text{etf}} \tag{3.42}$$

Which is the time constant define in Equation 3.11 found in Section 3.2. The solutions 3.34 can be rewritten as:

$$\delta I(t) = \frac{2\alpha}{(2+\beta)} \frac{E_\gamma}{\tau_{\text{th}} n I_0 R_0} \frac{1-\frac{\tau_{\text{el}}}{\tau_{\text{th}}}}{1-\frac{\tau_{\text{el}}}{\tau_{\text{etf}}}} \left(e^{-\frac{t}{\tau_{\text{el}}}} - e^{-\frac{t}{\tau_{\text{etf}}}} \right), \tag{3.43}$$

and considering Eq. 3.23 then the output voltage from the amplifier will be :

$$\delta V(t)_{\text{out}} = \frac{R_{\text{f}} M_{\text{f}}^{-1}}{M_{\text{in}}^{-1}} \frac{2\alpha}{(2+\beta)} \frac{E_\gamma}{\tau_{\text{th}} n I_0 R_0} \frac{1-\frac{\tau_{\text{el}}}{\tau_{\text{th}}}}{1-\frac{\tau_{\text{el}}}{\tau_{\text{etf}}}} \left(e^{-\frac{t}{\tau_{\text{el}}}} - e^{-\frac{t}{\tau_{\text{etf}}}} \right), \tag{3.44}$$

With the quantitative analysis of TES response to photon absorption complete, now is possible to present a qualitative description of the photon detection process. The stages illustrated in Figure 3.7 provide a visual representation that complements the mathematical model. In (a), the TES is voltage-biased to a steady state on its superconducting transition $0 < R_0 < R_{\text{N}}$. The equilibrium between the electrical power dissipated by the TES and the heat removed to the bath maintains the TES into a steady state, as a consequence output from the SQUID electronics is constant. This corresponds to the situation where the differential equation 3.24 and 3.25 can be simplified with $P_{\text{bath}} = P_{\text{J}}$ and $V = I_0 R_L + I_0 R_0$.

When a photon is absorbed (b), the TES experiences a rapid increase in temperature, causing its resistance to rise. Consequently, the current through the inductor L decreases, while the current through R_{sh} increases. This process occurs on the time scale dominated by the electrical time constant τ_{el}. Meanwhile, the change in current is promptly detected by the SQUID electronics. The FLL counteracts the change in flux within the SQUID by adaptively altering the feedback current. The output voltage from the amplifier is then proportional to the energy released in the TES, as shown in Eq. 3.44.

As this is happening, the cooling process of the TES begins. The reduced current flowing through the TES results in decreased joule heating, allowing the TES to cool

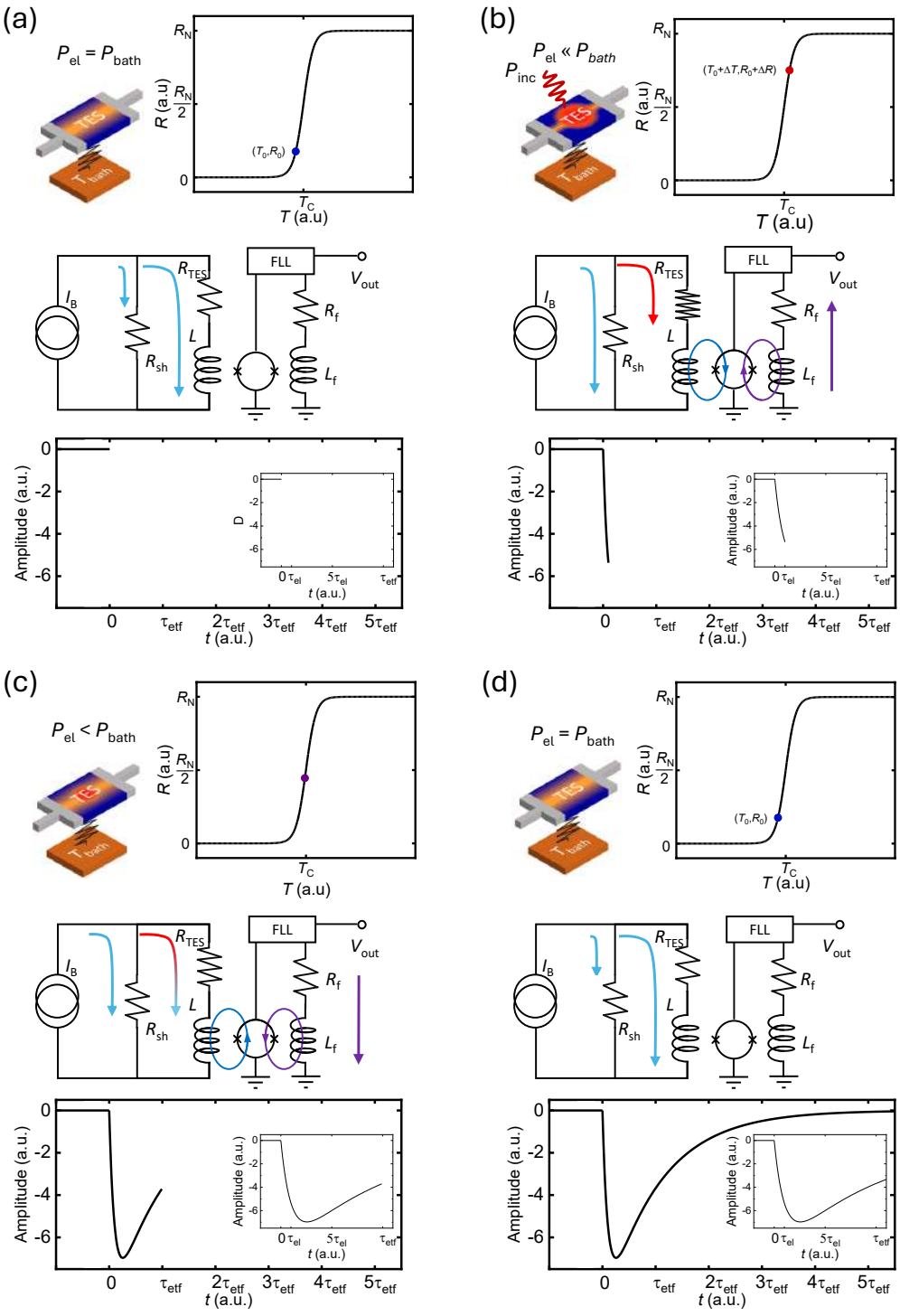

Fig. 3.7 Schematic of the photon detection process in a TES. (a) TES is in a stable state with no photon absorption, (b) depicts the absorption of a photon and the subsequent increase in resistance, (c) TES cools and returns towards its baseline. (d) restabilization to the steady state, completing the detection cycle.

down with a time constant τ_{etf} in the case of strong ETF. The ETF mechanism enables the system to self-regulate its temperature back to the initial condition. During this period, the FLL electronics provide continuous dynamic feedback.

Finally, the TES returns to its initial equilibrium state (d) after approximately $\sim 5\tau_{\text{etf}}$, ready for subsequent photon detection events.

3.5 Theoretical TES figure of Merit

In this section, I aim to introduce the theoretical performance of a TES. The focus will be on the key aspects of energy resolution and time response. Particular attention will be given to how the last two parameters—energy resolution and recovery time—are influenced by the working temperature T_0 and the active area A of the device.

The thermal capacity C of a superconductor is critical for understanding these relationships and can be approximated by the following expression [122]:

$$C = (2.43 + \gamma T_0 + \zeta T_0^3) t \cdot A \propto T_0 \cdot A \tag{3.45}$$

Here, t represents the thickness of the detector, and the constants γ and ζ are material-dependent parameters detailed further in [122].

Regarding thermal conductance, it was previously defined in Eq. 3.6. Additionally, the thermal coupling can be expressed using the electron-phonon coupling constant $\sigma_{\text{e-ph}}$ and the detector's volume. Consequently, the conductance G can be reformulated as:

$$G \approx n\sigma_{\text{e-ph}} T_0^{n-1} t \cdot A \propto T_0^{n-1} \cdot A \tag{3.46}$$

This framework allows to predict how modifications in T_0 and A affect the TES's performance, underscoring the interconnectedness of material properties, detector geometry, and operational conditions.

3.5.1 Energy Resolution

The energy resolution of a TES is a critical parameter that determines its effectiveness in detecting low-energy photons and particle. This parameter is highly sensitive to temperature, influencing heat capacity, thermal conductance, and various

noise components. Optimizing the energy resolution involves understanding the fundamental noise sources and their contributions.

An important figure of merit for a TES is the the noise-equivalent power, which is the square root of the power spectral density of the power-referred noise [1]:

$$NEP(\omega) = \sqrt{S_{P_{\rm tot}}(\omega)} \tag{3.47}$$

The theoretical energy resolution is given by the integrate of the NEP :

$$\Delta E_{\rm fwhm} = 2\sqrt{2ln(2)} \left(\int_0^\infty \frac{4}{S_{P_{\rm tot}}(f)} df \right)^{-\frac{1}{2}}, \tag{3.48}$$

where $f = \omega/2\pi$ is the frequency, and $S_{P_{\rm tot}}(\omega)$ denotes the power spectral density of the total noise. The thermodynamic noise sources, include Johnson noise (Nyquist noise) and thermal fluctuation noise (TFN). Additional noise sources, such as quantum fluctuations and fluctuations in the superconducting order parameter, can also contribute but are often negligible in TES applications.

Noise contributions is very well detailed in [1], here I will summarized the expressions for the four major contributions: Johnson noise from the TES resistance, Johnson noise from the load resistance, TFN due to thermodynamic fluctuations associated with the thermal conductance G and the amplifier noise from the SQUID.

One important parameter that is derived in [1] by solving the differential equation (3.32,3.33) is the power-to-current sensitivity $s_{\rm I}(\omega)$:

$$s_I(\omega) = -\frac{1}{I_0 R_0 (2+\beta)} \left(\frac{1-\tau_+/\tau_I}{1+i\omega\tau_+} \right) \left(\frac{1-\tau_-/\tau_I}{1+i\omega\tau_-} \right), \tag{3.49}$$

where $\omega = 2\pi f$. The power-to-current sensitivity $s_{\rm I}(\omega)$ is used to express noise components in spectral current density in units of A^2/Hz. The Johnson noise for the TES polarized at the working point (R_0, I_0) is:

$$S_{\rm I_{TES}} = 4kT_0 R_0 I_0^2 \frac{\xi(I_0)}{\mathscr{L}^2} (1+\omega^2\tau_{\rm th}^2) |s_{\rm I}(\omega)|^2, \tag{3.50}$$

where k is the Boltzmann constant, and $\xi(I_0)$ represents the spectral density reflecting the current-dependent non-linearity. Similarly, the current noise due to Johnson noise in the load resistor is expressed as:

$$S_{\mathrm{I_L}} = 4kT_L I_L^2 R_L \frac{(\mathscr{L}-1)^2}{\mathscr{L}^2}(1+\omega^2\tau_{\mathrm{I}}^2)|s_{\mathrm{I}}(\omega)|^2. \tag{3.51}$$

The term due to thermal fluctuation noise in the conductance can be expressed as:

$$S_{\mathrm{I_{TFN}}} = 4kT_0 G \times F(T_0, T_{\mathrm{bath}})|s_{\mathrm{I}}(\omega)|^2, \tag{3.52}$$

where $F(T_0, T_{\mathrm{bath}})$ is a dimensionless function encapsulating the dependence on the thermal conductance exponent and the nature of phonon scattering at the boundaries between the TES and the bath. The value of $F(T_0, T_{\mathrm{bath}})$ typically ranges between 0.5 and 1 [123], reflecting the spectrum of possible boundary scattering behaviors from diffuse to specular reflections.

Finally, the noise introduced by the SQUID amplifier, often referred to as current-referred amplifier noise $S_{\mathrm{I_{amp}}}(\omega)$, must be considered. It contributes to the total noise in a manner inversely proportional to the square of the power-to-current responsivity:

$$S_{\mathrm{amp}}(\omega) = \frac{S_{\mathrm{I_{amp}}}(\omega)}{|\, s_{\mathrm{I}}(\omega)\,|^2}. \tag{3.53}$$

The power spectral density of the total noise $S_{P_{\mathrm{tot}}}(\omega)$ is therefore:

$$S_{P_{\mathrm{tot}}}(\omega) = \frac{1}{|\, s_{\mathrm{I}}(\omega)\,|^2}(S_{\mathrm{I_{TES}}} + S_{\mathrm{I_L}} + S_{\mathrm{I_{TFN}}} + S_{\mathrm{I_{amp}}}). \tag{3.54}$$

In the important limit where the amplifier noise $S_{\mathrm{I_{amp}}}$ is negligible, $\mathscr{L} \gg 1$, strong ETF ($T_{\mathrm{bath}} \ll T_{\mathrm{C}}$), $\xi(I_0) = 1+2\beta$, and $F(T_0, T_{\mathrm{bath}}) = 1$, the integration of these noise contributions in Eq. 3.48 gives:

$$\Delta E_{\mathrm{fwhm}} \approx 2\sqrt{2\ln(2)}\sqrt{4kT_0^2\frac{C}{\alpha}\sqrt{\frac{n(1+2\beta)}{2}}}, \tag{3.55}$$

The electronic heat capacity is pivotal in determining device behavior, as described in Eq. 3.55. A high heat capacity leads to negligible temperature changes during an event, making it challenging to distinguish these changes from the device's thermal fluctuations. Conversely, a low heat capacity may cause the temperature to rise excessively during an event, exceeding the superconducting transition's width and causing device saturation. The maximum energy saturation, defined as [124]:

$$E_{\text{sat}} \equiv C\Delta T \approx \frac{CT_0}{\alpha}, \tag{3.56}$$

represents the peak energy that the electrothermal feedback (ETF) mode can dissipate in conditions of strong electrothermal feedback. Consequently, Eq. 3.55 simplifies to:

$$\Delta E_{\text{fwhm}} \approx 2.355\sqrt{4kT_0E_{\text{sat}}\sqrt{\frac{n}{2}}}, \tag{3.57}$$

Considering Eq. 3.45, the energy resolution is expressed as proportional to the square root of the device's area and a power of the operating temperature:

$$\Delta E_{\text{fwhm}} \propto T_0^{\frac{3}{2}} \cdot A^{\frac{1}{2}}. \tag{3.58}$$

This relationship highlights the significant influence of the operating temperature, T_0, on determining the energy resolution of the device. For example, lowering T_0 from 0.3 K to 0.1 K can improve the intrinsic resolution by a factor of two. This improvement demonstrates the critical role of the working point temperature in enhancing device performance. Furthermore, the dependence on the square root of the area implies that for a square-shaped TES, the energy resolution has a linear dependency on the length of the side, underscoring the geometric influence on performance.

3.5.2 Timing Properties

Recovery Time and Maximum Detection Rate

The maximum detection rate (MDR) of a TES is directly influenced by its recovery time. According to [40], the "recovery time of a single-photon detector is the total amount of time required after a detection event for the detection efficiency to return to its nominal steady-state". When a photon is absorbed, the TES signal evolves over time as:

$$\delta I \propto \left(e^{-\frac{t}{\tau_+}} - e^{-\frac{t}{\tau_-}}\right) \tag{3.59}$$

Under conditions of strong electrothermal feedback (ETF), these time constants can be approximated as:

$$\tau_+ \approx \tau_{\text{el}} = \frac{L}{R_L + R_0(1+\beta)},$$

$$\tau_- \approx \tau_{\text{etf}} \approx \frac{n}{\alpha}\frac{C}{G},$$

Since TES detectors do not have dead time or reset time, signals can be detected even when the TES has not fully recovered. However, as discussed already in section 2.3.5 the recovery time is the time it takes for the current pulse to return to zero, which can be approximated as $5\tau_{\text{etf}}$. In the case of periodic signals (such as a pulsed laser or a single-photon emitter stimulated at a fixed frequency), the MCR of a TES can be defined as:

$$MCR = \frac{1}{5\tau_{\text{etf}}} \tag{3.60}$$

Therefore, to operate the TES at a high detection rate, it is crucial to minimize the time constant τ_{etf}. However, the stability of the detector must also be considered. According to [117], stability is ensured if:

$$\frac{\tau_{\text{etf}}}{\tau_{\text{el}}} > 5.8 \tag{3.61}$$

This impose that both time constant must be minimize. The electrical time constant, τ_{el}, is primarily influenced by the input inductance, which can be as low as 3 nH [119]. This enables typical electrical time constants to range from 10 ns to 100 ns [95, 22].

For the fall time τ_{etf}, using Eqs. 3.45 and 3.46, the dependence on temperature and area is given by:

$$\tau_{\text{etf}} \approx \frac{n}{\alpha}\frac{C}{G} \propto T_0^{-(n-2)} A^0 \tag{3.62}$$

This means that, contrary to the energy resolution, the maximum detection rate improves if the TES is operated at a higher temperature. Therefore, one way to improve the MDC is to work at higher temperatures, though this comes at the cost of reduced energy resolution. Since the dependency of the active area cancels out, reducing the area could compensate for this, but one must then consider the issue of coupling efficiency.

Another way to reduce τ_{etf} is to directly improve the conductance by enhancing the TES design. An example of this approach is shown in [116], where the use of gold pads on top of their tungsten TES enhanced the conductance and thus the time constant, while keeping the operating temperature and energy resolution relatively constant.

Jitter

The timing jitter, or timing uncertainty, for a pulse signal crossing a threshold is determined by the noise and the slope of the signal at the threshold crossing point. For TES signals, the timing jitter can be expressed as [23]:

$$\Delta t_\sigma = \frac{\sigma}{\frac{dV}{dt}\Big|_t} \approx \frac{\sigma}{V_{\text{max}}}\tau_+, \tag{3.63}$$

where V_{max} is the maximum amplitude of the signal and σ represents its standard deviation. This approximation holds for a linear rise of the pulse. The standard deviation is proportional to the energy resolution, and the rise time constant can be approximated with the electrical time constant τ_{el}.

The standard deviation of the maximum amplitude depends on the power noise and is proportional to the energy resolution. Therefore, the timing jitter is given by:

$$\Delta t_\sigma \propto \frac{T_0^{\frac{3}{2}} \cdot A^{\frac{1}{2}} \cdot L}{V_{\max}}. \tag{3.64}$$

In summary, the theoretical performance metrics of TES detectors highlight the critical trade-off between energy resolution and timing properties, emphasizing the significant impact of operating temperature and active area on optimizing these detectors for high-precision physics experiments. In the next chapter, I will provide a detailed overview of the experimental apparatus and methodologies used to characterize and study TESs, showcasing the practical implementations of the theoretical concepts discussed.

Chapter 4

Experimental setup

This chapter describes the various experimental setups used throughout my PhD thesis. The majority of my research activities were carried out at the Innovative Cryogenic Detectors Laboratory in the Istituto Nazionale di Ricerca Metrologica (INRiM), the National Metrology Institute of Italy. INRiM has extensive facilities and expertise in the fabrication and testing of TESs, which were fundamental to the successful outcome of my PhD work. The setups detailed in this chapter were integral to the experiments and results presented in subsequent chapters.

The chapter begins with a description of the low-temperature setups essential for the operation of TES, given their superconducting nature. Specifically, we focus on the cryogenic systems used at INRiM, including the Pulse-Tube Driven Adiabatic Demagnetization Refrigerator (ADR) cryostat. This is followed by an explanation of the TES readout system using dc-SQUIDs and the fiber alignment setup for sample preparation.

Additionally, the chapter includes details on the low-temperature setup at the Physikalisch-Technische Bundesanstalt (PTB) in Braunschweig, where I conducted part of my research. This setup is used to measure the SDE of TES devices. Finally, the chapter covers the characterization of the DCR and the low-energy electron source setup using carbon nanotubes (CNTs).

INRiM's advanced facilities and expertise in superconducting technology provided the foundation for the experimental work presented in this thesis. The fabrication of TES devices at INRiM, particularly those made from Titanium-Gold (TiAu)

bilayers, allowed for precise control over the superconducting properties essential for my research.

4.1 INRiM Low-Temperature setup

As discussed in earlier sections, TESs should be operated at temperatures lower than their critical temperatures. Since TESs operate in the sub-Kelvin range, an environment capable of reaching such low temperatures is essential. The low-temperature setup described here employs two cooling methods: a pulse tube refrigerator and an Adiabatic Demagnetization Refrigerator (ADR). The pulse tube refrigerator brings the ADR temperature below 3 K, and the ADR further cools a section of the cryostat to below 100 mK.

As a reference for this section, we will describe the cryostat used in the INRiM laboratory, which is the Pulse-Tube Driven ADR Cryostat Model 103-RC Rainier from HPD [125]. However, some of the measurements that will be presented were performed using a different cryostat with similar technology: an ADR cryostat from Entropy (see section 4.4).

The Cryostat Model 103-RC Rainier from HPD is a cryogen-free, pulse-tube-driven cryostat that employs ADR to reach temperatures below 100 mK. The cryostat stages operate at approximately 60 K, 3 K, 500 mK, and 30 mK. The model includes a Cryomech pulse-tube refrigerator (PTR), which provides cooling for the 60 K and 3 K stages. The PTR consists of a compressor package, remote motor, cold head, bellows, and helium flex lines. It is a closed-loop system that offers reliable cooling without using any liquid cryogens.

The ADR generates the coldest stage temperatures (500 mK and 30 mK). It is made by a superconducting 4 T magnet, a Gadolinium Gallium Garnet (GGG) paramagnetic salt pill, a Ferric Ammonium Alum (FAA) paramagnetic salt pill, a Hiperco 50 magnetic shield, Kevlar suspension system, and a coold finger for the experiment. The ADR cools through the adiabatic demagnetization of the paramagnetic salt pills. The Kevlar suspension isolates the salt pills from warmer stage temperatures. The ADR is connected to the 3 K stage via a heat switch that allows the pills to be isolated when the switch is open.

The cryostat frame, shown in Figure 4.1, consists of three stage plates (room temperature, 60 K, and 3 K) connected by thermally isolating supports. Each plate includes a series of pass-throughs for experimental and thermometer wiring. Radiation shields connected to the 60 K and 3 K plates block blackbody radiation from reaching the low-temperature experimental volume. The PTR is attached to the cryostat frame with bellows and copper jumper cables to reduce vibrations and allow for differential thermal contraction. A vacuum jacket attaches to the 300 K plate and encloses the cryostat. An additional magnetic shield made of Amumetal 4K (A4K) [126] is mounted inside the 3 K radiation shields to minimize the effect of external magnetic fields on the 500 mK and 30 mK stages. The cryostat temperature is monitored with a thermometer for each temperature stage. The 30 mK stage thermometer is a Ruthenium Oxide Thermal Sensor with an accuracy of ± 5 mK from 30 mK to 150 mK [127]. Besides the thermometers and the operational system, the cabling mounted in the system for experimental purposes allows for the transmission of electrical signals through two different connectors with 12 twisted pairs each. One connector is dedicated to R vs T measurements of the superconducting film. This cabling passes through a series of RC and RF filters to improve thermalization by reducing noise-related heating. The second connector with 12 twisted pairs is used to operate the SQUIDs with the Magnicon XXF-1 electronics, described in Section 4.2.

At the 300 K stage, a vacuum feedthrough is used to bring optical fibers inside the cryostat. Each temperature stage includes a small pipe to guide the fibers down to the 30 mK stage.

This cryostat model also allows for rapid cooldown using liquid nitrogen flowing through heat exchangers to accelerate the cooldown from room temperature, providing shorter turnaround times for experiments. In the INRiM setup, a standard pulse tube cooldown takes about 48 hours to go from 300 K to 3 K, while the rapid cooldown system shortens the cooldown to 3 K to about 20 hours.

The rapid cool system consists of an integrated liquid nitrogen line that enters the cryostat through a vacuum port in the 300 K plate, travels through a heat exchanger on the 60 K plate, through another heat exchanger on the 3 K plate, and then exits the cryostat through another port in the 300 K plate. During cooldown, liquid nitrogen flows continuously through this heat exchange system to quickly cool both the 60 K and 3 K plates directly. The liquid nitrogen is flowed in its dedicated line from

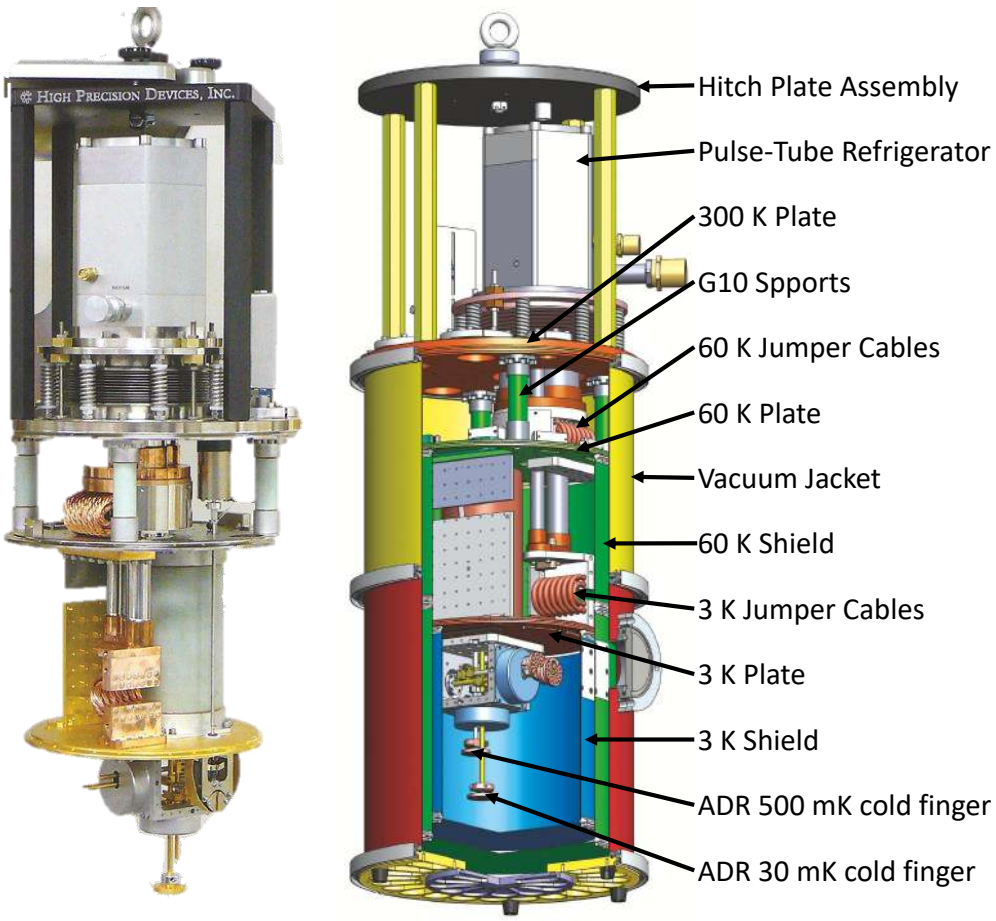

Fig. 4.1 Schematic and picture of the HPD cryostat [125]. The chassis is made to support the two stage pulse-tube cryocooler and ADR, to reduce the thermal load on the ADR, and to provide a structure to mount and heat sink wiring and other components. The cryostat frame has three stage plates: 300 K, 60 K, and 3 K. The 60 K and 3 K stages are cooled by the 1st stage and 2nd stage of the pulse-tube, respectively. Low thermal conductivity supports connect the stage plates. High thermal conductivity radiation shields attach to, and hang from, the 60 K and 3 K stages creating a series of volumes to reduce the heat load on the ADR stages. A vacuum jacket hangs from the 300 K plate creating the vacuum envelope

300 K to 80 K, which takes approximately 3 hours and 30 minutes, after which the temperature continues to decrease with the pulse tube alone. Warming up the system takes approximately 48 hours.

In the next section, we will describe the ADR system, which enables the operation of the TESs below 100 mK.

4.1.1 Adiabatic Demagnetization Refrigerator (ADR)

The Adiabatic Demagnetization Refrigerator was historically the first method that enabled reaching temperatures below 1 K. Proposed in 1926 by P. Debye and W. F. Giauque, it was practically realized by W. F. Giauque and D. P. MacDougall in 1933. Modern ADRs can reach temperatures around 2 mK. Despite being a "one-shot" cryostat and requiring a strong magnetic field during the cooling process, ADRs are advantageous as nowadays they can be operated without cryogenic liquids and can operate in zero gravity conditions [122].

The ADR, shown in Figure 4.2, generates the two coldest stages of the cryostat through the adiabatic demagnetization of paramagnetic salt pills. It contains two paramagnetic salt pills: a GGG pill generating a 500 mK stage and a FAA pill generating a 30 mK stage. The pills are situated in the bore of a cylindrical 4 T superconducting magnet that provides the magnetic field necessary for ADR operation. The magnet lies within a Hiperco 50 magnetic shield to prevent most of the magnetic field from escaping to the rest of the cryostat. A gold-plated copper thermal shield reduces the radiative load on the Hiperco 50 shield and magnet. The salt pills are semi-rigidly held in place and thermally isolated from other stages with a Kevlar thread suspension system.

Let us consider a solid containing paramagnetic ions with an electronic magnetic moment μ. Suppose that, within a certain temperature range, the interaction energy ε_{m} between the magnetic moments and an external magnetic field is small compared with kT. At temperatures relevant for ADR refrigeration, the magnetic entropy (a few J/mole) is much larger than other system entropies. Cooling the salt to a certain temperature brings the interaction among magnetic moments to the order of kT, resulting in spontaneous magnetic alignment. An external magnetic field partially aligns the magnetic moments along its direction, reducing entropy at a fixed temperature.

Figure 4.3 illustrates the magnetic cycle. The process starts from point A. The first step involves isothermally magnetizing the pill from zero field to 4 T, ending at point B. The heat produced along the path AB is delivered to the 3 K plate cooled by the cryocooler. In the second step, the pill is thermally isolated from the 3 K stage by opening the heat switch. The crystal is then adiabatically demagnetized (line BC). During this process, some heat is absorbed from the surrounding ballast mass,

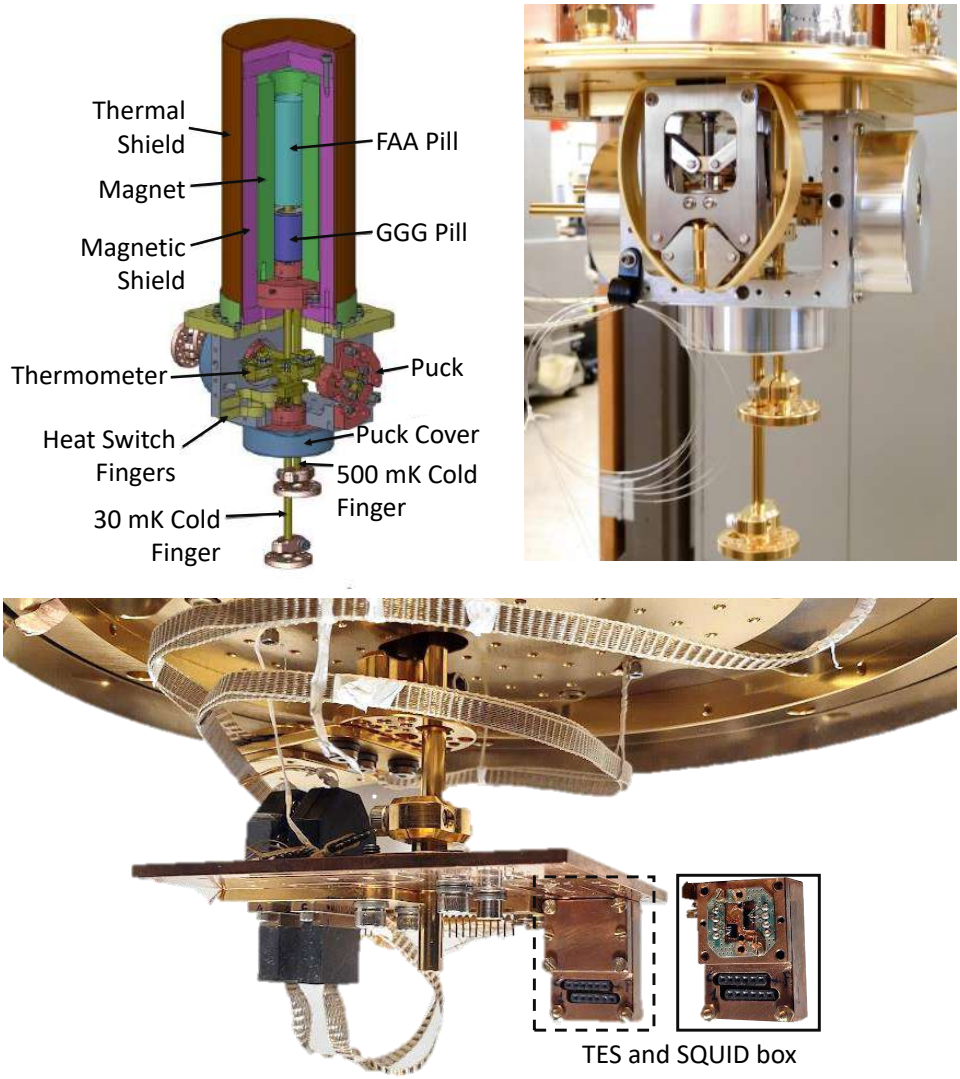

Fig. 4.2 Schematic of the Adiabatic Demagnetization Refrigerator (ADR) and photograph of the setup. The schematic and the photograph on top right shows the ADR system before mounting the rest of the experimental apparatus. The photograph on the bottom shows the square (20 cm $\times$ 20 cm) OFHC copper plate, which is connected to the FAA pill through the 30 mK cold rod. The devices are mounted on this plate. The photograph also shows a copper box where two SQUIDs are mounted on the back and two TESs can be mounted on the front.

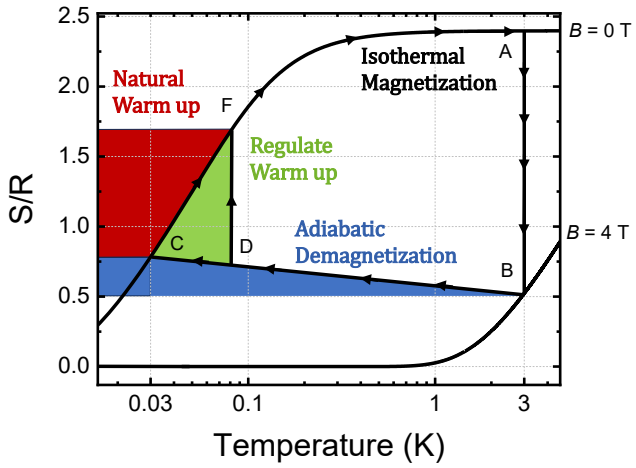

Fig. 4.3 Magnetic cycle for adiabatic demagnetization refrigeration, The vertical axis is Entropy, in a unitless form created by dividing the specific entropy by the gas constant R. (A-B) Isothermal magnetization of the paramagnetic salt pill from zero to 4 T, releasing heat to the 3 K stage. (B-C) Adiabatic demagnetization, where the pill absorbs heat from the surrounding ballast mass, represented by the area shaded in blue. (C-D) Optional temperature stabilization through magnetic field regulation, allowing the ADR to maintain a stable temperature. The area shaded in red represents the cooling power during natural warm-up, while the area shaded in green represents the "bonus" entropy gained by regulated warm-up.

represented by the area shaded in blue. After reaching a minimum temperature, the system can either gradually warm up naturally along the entropy curve ($B = 0$) or can be stabilized at a higher temperature, like point D, by regulating the magnetic field. In this way, the ADR can maintain a stable temperature until the applied magnetic field reaches zero. During natural warm-up, the pill's cooling power is represented by the area shaded in red. During regulated warm-up, the cooling power is given by the red area plus the green area. The green area is the "bonus" entropy gained by regulating the temperature instead of letting the system warm up naturally. Practically speaking, the magnetic cycle needs to be repeated every time the operating temperature of the experiment is to be reached again.

For this system, a typical magnetic cycle takes about 2 hours. After one week at full regime with one cycle per day, the cryostat is capable of maintaining a stable temperature of 40 mK for approximately 20 hours.

4.2 INRiM TES read-out setup with dc-SQUID

The operation of a TES relies on electrothermal feedback, and its readout is done via a dc-SQUID transimpedence amplifier. In Chapter 3, these two aspects were thoroughly discussed. Here, we will explain how they are integrated into the low-temperature setup discussed above. Figure 4.4 displays the schematic of the TES-SQUID circuit (top) and the schematic of the installation in the cryostat (bottom).

All measurements presented in this thesis were obtained using SQUID chips provided by the Physikalisch-Technische Bundesanstalt (PTB), as described by Drung et al. in [119]. Each 3 mm $\times$ 3 mm chip contains two SQUID circuits, each capable of reading out one TES device. Each circuit comprises a SQUID array of 16 SQUIDs, an input coil, a feedback coil, and four resistors.

On one end, the chip is connected via wiring up to the 300 K stage, where it interfaces with the Magnicon XXF-1 electronics [120]. The electronics allow biasing the SQUID (I_b and V_b in the top circuit, $\pm V$ in the bottom), the TES circuit (I_Bias in the top circuit, $+R, -INR$ in the bottom), and the feedback circuit (Φ_b in the top circuit, $\pm F$ in the bottom). The other end of the chip connects the TES to the input coil. A series of built-in resistances in the SQUID chip allows selection of the shunt resistance value (R_sh).

The connections are facilitated through a sample holder where TES chips are mounted and wire-bonded to a PCB. This PCB then connects to the copper box shown in Figure 4.2, where the SQUID chips are housed. Although SQUIDs can operate from 3 K, the ones in use are suitable to be operated also at 30 mK, in such a way that they can be mounted on the ADR cold finger in order to to minimize parasitic resistance and stray inductance using shorter wiring connections.

To further improve performance, the SQUID and TES chips could be mounted nearby, allowing for direct wire bonding between them. This setup minimizes both stray inductance and parasitic resistance, as described in Section 4.4 for the PTB setup. However, in the INRiM setup, the connection is mediated via a PCB to enable the replacement of TES chips without dismounting the SQUID chip from the cryostat. SQUIDs are highly sensitive to electrostatic discharge, which can occur during transportation, wire bonding, and mounting. By separating the TES from the SQUID chip, the risk of damaging the SQUID during these processes is minimized.

The characteristics values of INRiM TES read-out setup are listed in table 4.1, the valued refer a single SQUID chip with two circuits labeled *Channel 1* and *Channel 2*.

Together with the XXF-1 electronics, Magnicon provides software for controlling the bias sources (I_b, I_B, Φ_b) and other electronic parameters such as the feedback resistance (R_f) and the option to operate in Flux Locked Loop (FLL) mode. As discussed in Section 3.3.1, operating the SQUID in FLL mode ensures stable operation over a wide dynamic range. The optimal working parameters for FLL mode, such as I_b and V_b, were studied at 30 mK prior to this thesis and remained unchanged throughout the experiments. The output of the XXF-1 electronics (V_{out}), one per channel, exits via a BNC cable, which is connected to either a Lecroy oscilloscope

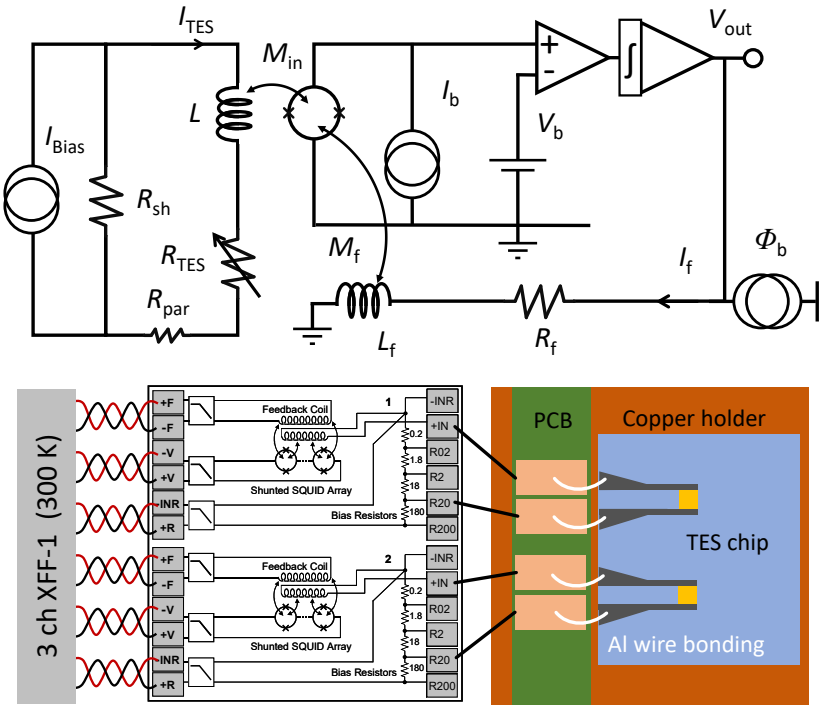

Fig. 4.4 (Top) Circuit diagram of the TES-SQUID setup. The TES is biased with a current generator I_B in parallel with a shunt resistance. Changes in the current through the TES are read by the SQUID circuit. The SQUID is used in FLL mode, providing an output proportional to the TES response. (Bottom) Schematic of the installation in the INRiM low-temperature setup. The TES chip is wire-bonded to a PCB, which is then connected to the copper box housing the SQUID chip. The TES and SQUID chips are mounted at the 30 mK stage.

Table 4.1 Table of the properties of the two SQUID channel used in the INRiM low-temperature setup

Parameter (30 mK)	Channel 1	Channel 2
L_{in}	~ 3 nH	~ 3 nH
L_{stray}	~ 7 nH	~ 7 nH
R_{sh}	20 mΩ	20 mΩ
R_{par}	10 mΩ	10 mΩ
M_{in}^{-1}	24.61 μAΦ_0^{-1}	24.66 μAΦ_0^{-1}
M_{f}^{-1}	66.31 μAΦ_0^{-1}	66.11 μAΦ_0^{-1}
Transimpedance amplification ($R_{\text{f}} = 100k\Omega$)	269 443 VA^{-1}	268 085 VA^{-1}

model WaveRunner 620Zi or a digitizer from National Instruments model PXIe-5122 during the experiment.

4.3 INRiM Fiber Alignment setup

The samples fabricated at INRiM are aligned with optical fibers in a setup that consists of an inverted microscope with objective magnifications of 5×, 20×, and 100×, connected to an IR camera from New Imaging Technologies. As shown in the left photograph in Figure 4.5, the TES chip is placed on a 100 µm thick glass microscope slides, which can be positioned on top of the microscope objective. Illuminating the TES chip from above with an incandescent light is sufficient to exploit the IR components of the emission and obtain an image of the chip.

The chip substrate, made of silicon nitride, silicon oxide, and silicon, is transparent to IR light, while the TES and wiring, made of metal, reflect most of the IR light. This feature allows for good contrast between the bare substrate and the substrate with metal deposition on top, providing clear visibility of the sample layout as showon in the image in Figure 4.5. Once the TES area is centered and above the objective, a fiber is clamped to a micro-motion controller above the chip. One end of the fiber (typically 1 m long) is manually pre-aligned in front of the TES, while the other end is spliced to another fiber connected to a commercial IR continuous-wave laser. By turning on the laser and achieving good pre-alignment, a light spot from

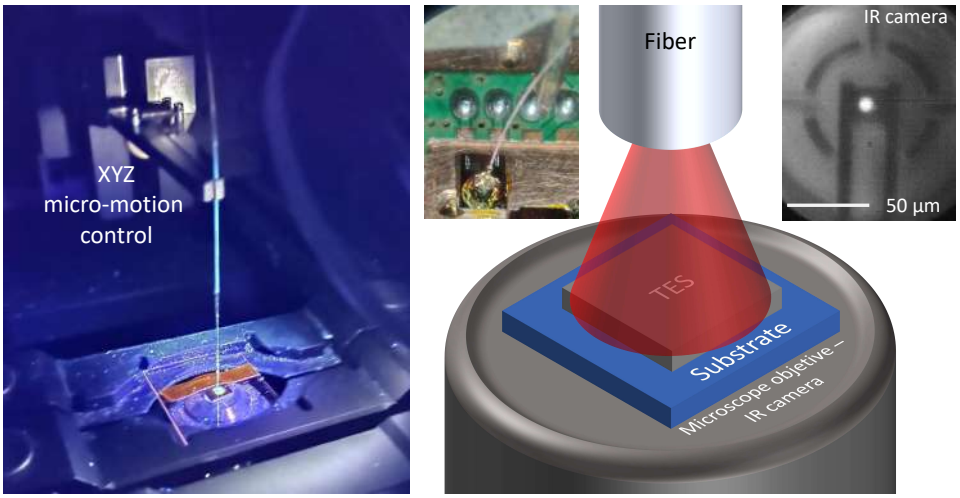

Fig. 4.5 Alignment setup featuring the inverted microscope, fiber alignment system, and IR view. The fiber above the TES chip is aligned using XYZ micro-motion control and a live image with an IR camera. Once the fiber is aligned is glued to the substrate with uv curable resin.

the fiber core will appear on the TES chip. With the micro-motion controller, it is possible to move the spot so that it stays within the TES active area.

Once the alignment is complete, a drop of UV-curable resin glue (Norland 68) [128] is used to attach the TES chip to the fiber. The glue is cured for 24 hours at 50 °C. The alignment method presented here is similar to the one used in [14], which demonstrated that high system detection efficiency can be achieved. Unlike the self-alignment system described in [101], our method does not rely on the chip shape, making it more flexible for various chip and sample holder designs. However, this approach is less reproducible and depends on the experience of the person performing the alignment.

Once the glue is cured, the TES and the fiber are mounted in the copper box shown at the bottom of Figure 4.2. The TES chip is either glued with Varnish glue or clamped to the copper plate. Thermalizing the fiber before the TES chip is crucial and is achieved by taping it to the 30 mK plate approximately 10 cm away from the TES chip. Thermalizing the fiber away from the TES reduces stress due to the different thermal contraction coefficients of the fiber and the copper. From that anchor point to the chip, copper tape is used to prevent radiation from the 3 K plate from warming up the TES-fiber system.

This configuration is the result of a series of trials and errors. Poor thermalization of the fiber caused heating effects on the TES, and creating an anchor too close to the TES resulted in excessive stress, causing the fiber to detach from the chip.

4.4 PTB Low-Temperature and System Detection Efficiency Setup

In this section, I describe the setup present at the laboratory of Physikalisch-Technische Bundesanstalt (PTB) in Braunschweig. As part of my PhD activity, I had the opportunity to spend four months as a guest researcher at PTB. Within the SEQUME project mentioned in section 1.1.3, one of the activities I followed at PTB was the setting up of a cryo-optical facility for single-photon source characterization and measure the system detection efficiency (SDE) of TES devices.

The low-temperature setup at PTB is similar to the one described in section 4.1, consisting of a cryostat driven by a pulse tube with an ADR to reach temperatures below 1 K, all provided by the company Entropy. The coldest stage of the cryostat, attached to the FAA salt pill, can reach around 100 mK, and magnetic shielding is provided by a superconducting aluminium shield. At the cold stage, wiring connections for SQUID control with XXF-1 electronics are present, as well as fiber access points. The left image in Figure 4.6 show the open aluminium magnetic shield box with two sample holders mounted on the FAA cold finger. The image with the blue frame is a photograph under the microscope of two TES chips fabricated at INRiM before wire bonding with the 3 mm $\times$ 3 mm SQUIDs chip, which is in the middle. The two TES chips with optical fibers aligned and glued using the method described in section 4.3 are visible at the bottom. The image with the red frame shows a zoomed view of two TES chips fabricated at the National Institute of Advanced Industrial Science (AIST) in Japan. The fiber alignment for these chips is done using the alignment technique described in [101]. Both INRiM and AIST TES chips are mounted closer to the SQUID chip compared to the setup described in section 4.2 in order to minimize stray inductance. Recall from equation 3.37 that the electrical time constant τ_{el} has an inverse dependence on inductance. By reducing stray inductance, we contribute to lowering τ_{el}. A low τ_{el} is crucial for one of the goals of the SEQUME project, which was discussed in section 1.1.3, aims to operate TESs with detection rates above 2 MHz.

Another goal of the project is to set up a facility for single photon source characterization with a system detection efficiency above 90%.

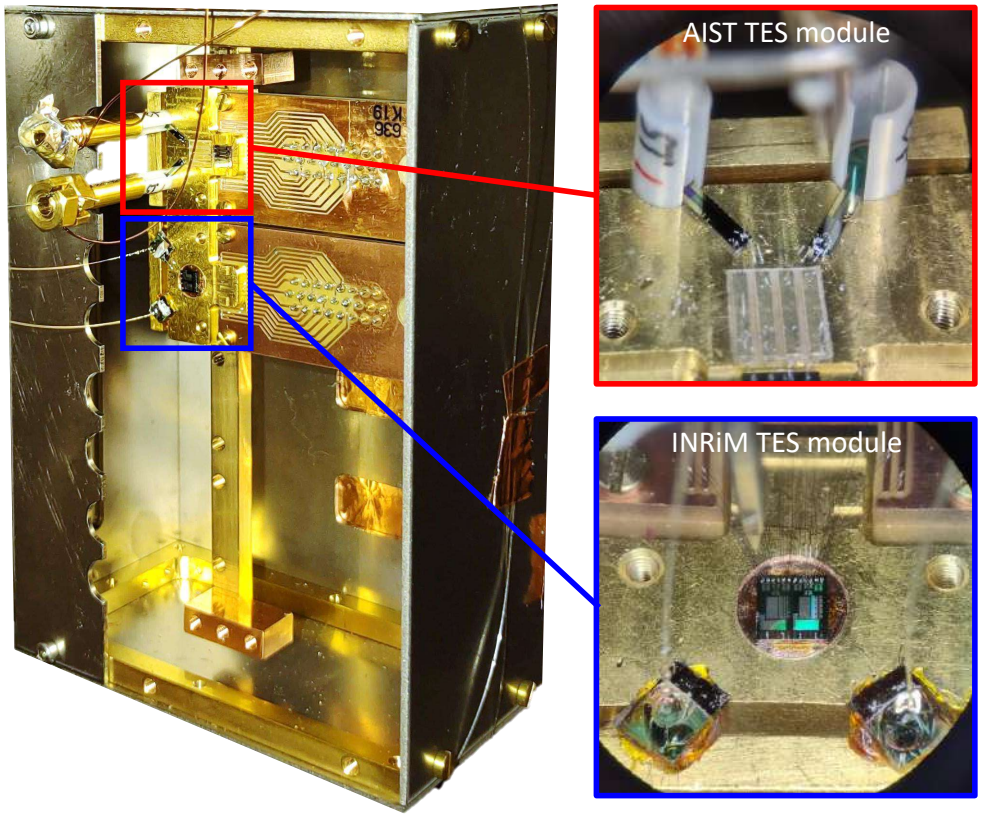

Fig. 4.6 Low-temperature setup at PTB featuring the open aluminum magnetic shield box, two sample holders mounted on the FAA cold finger, and images of TES chips. The red box highlights two samples from AIST. The chips are inside ceramic sleeves where a fiber can be placed using the self-alignment method described in [101]. The blue box provides a close-up of the INRiM TES with the fiber glued on top using the method described in Section 4.3.

4.4.1 Setup for System Detection Efficiency measurement

The setup used to measure the system detection efficiency is similar to the one described in [129], following an approach similar to that described in [130]. It consists of a light source, optical fibers, a monitor diode, and an optical attenuator. In this setup with the measurement of the SDE we refers to the probability of photon detection once the photon enters the fiber connector mounted on the vacuum shield of the cryostat, thus accounting for losses in the fiber inside the cryostat, misalignment losses between the fiber and TES, and the internal losses of the TES.

Figure 4.7 shows the schematic of the setup. A pulsed laser head emitting around 1550 nm (precisely 1548 nm) with a pulse duration of less than 100 ps is

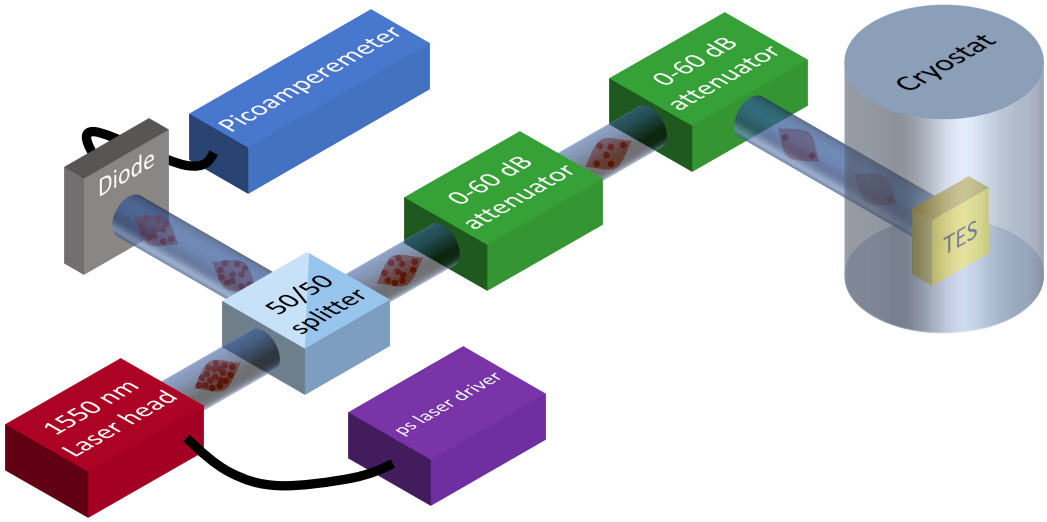

Fig. 4.7 Schematic of the setup to measure the System Detection Efficiency featuring laser source, a monitor optical paths, and attenuated path that goes to the TES inside the cyrostat.

connected to ps-laser driver. An external trigger from a waveform generator regulates the emission rate. The output of the laser head is coupled to a standard telecom single-mode fiber. This fiber is connected to a 50/50 fiber beam splitter; one output of the splitter is monitored by an InGaAs photodiode calibrated at PTB against a cryogenic radiometer. The photocurrent is measured by a picoammeter . The second output is connected in series to two attenuators. The output from the second attenuator connects to the input of the cryostat. The cryostat's input consists of a vacuum feedthrough fiber connector. From there, approximately 2 meters of fiber pass through the various stages of the cryostat until reaching the TES. The SDE is calculated starting from that connection, therefore it includes the losses in the vacuum feedthrough, the losses in the fiber, and the alignment of the fiber with the TES. A fine characterization of this setup allows converting the photocurrent measured by the picoammeter into the number of photons per pulse expected at the input of the cryostat with a relative uncertainty of $\sim 1\%$. The ratio between the number of photons per pulse measured by the TES and this input photon number per pulse represents the SDE.

4.5 Low-Temperature Low-Energy Electron Source Setup

In this section, we describe the setup used to study the TES response to low-energy electrons. The simple and compact setup relies on the emission of electrons from carbon nanotubes (CNTs) via field emission. With this setup, we are capable of producing monochromatic electrons at low temperatures in the range from 50 to 300 eV.

Electron field emission was first discovered by Wood in 1897 [131]. Following the discovery of CNTs by Iijima in 1991 [132], Chernozatonskii et al. demonstrated in 1995 that CNTs can be used as electron sources via field emission [133].

The current density of electrons emitted by a CNT is described by the Fowler-Nordheim formula [134]:

$$J = 1.54 \times 10^{-6} \frac{(\gamma E)^2}{\Phi} \exp\left(-6.79 \times 10^7 \frac{\Phi^{3/2}}{\gamma E}\right) \tag{4.1}$$

where E is the electric field, γ is the enhancement factor, and Φ is the work function of the material. Considering typical values of γ between 10^3 and 10^4, field emission with CNTs can start with $E < 10^3$ V/mm. The CNTs used in this setup consist of chips of vertically aligned CNTs and were synthesized in the INFN laboratory 'TITAN' at Sapienza University of Rome [135–138]. The nanotubes were grown through chemical vapor deposition on a 500 µm silicon substrate, and are approximately 120 µm in length, while covering a surface of roughly 3 mm × 3 mm, a imagine made with a scanning electron microscope of this type of sample is visible in Figure 4.8 (a).

A single setup for both the characterization of CNT emission at low temperatures and electron counting with TES was designed, as shown in Figure 4.8(b). The setup consists of three square copper plates stacked one on top of the other, using sapphire (A_2O_3) substrates 500 µm thick and 0.5 cm × 0.5 cm in size as spacers, as shown in Figure 4.8(c). One copper plate serves as the base and can be screwed to the cryostat. The other two plates are used as the anode and cathode for measurement when only the CNTs are mounted, and no TES chip is used. The sapphire spacers ensure a fixed distance, thermal conductivity, and electrical isolation. The CNTs

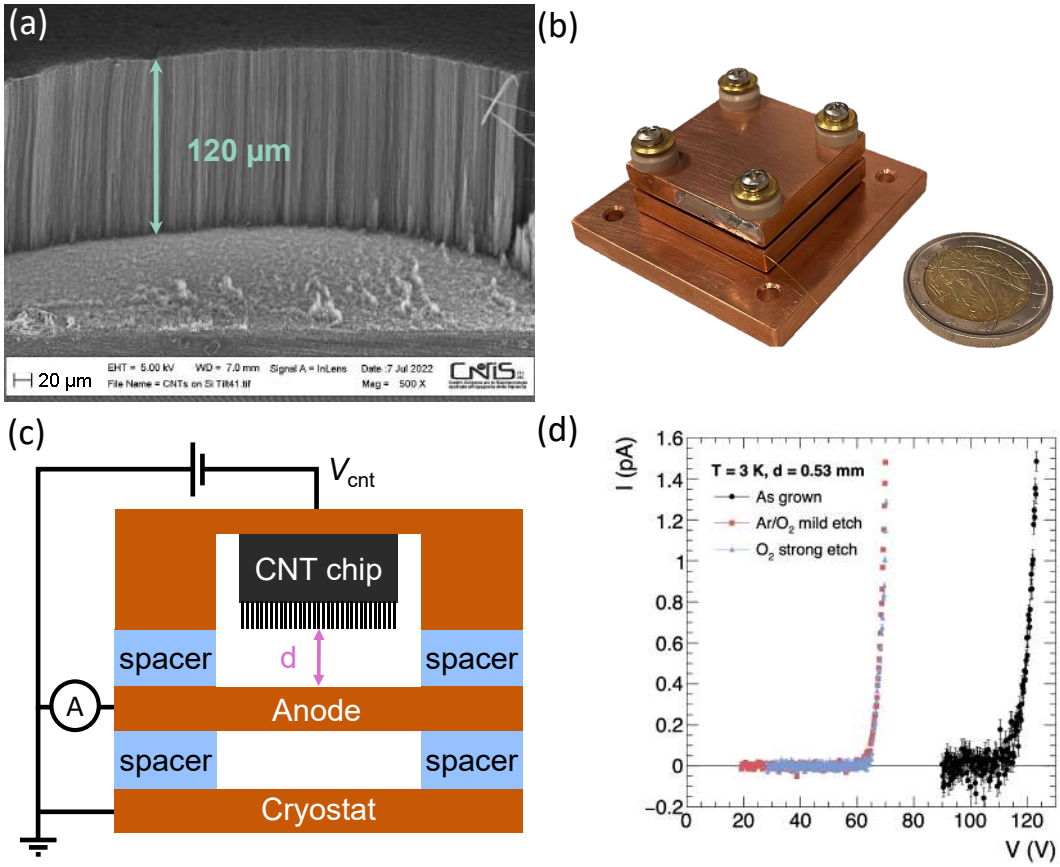

Fig. 4.8 Setup for the characterization of CNT field emission. (a) SEM image of vertically aligned CNTs. (b) Photograph of the MIC setup: three copper plates stacked on top of each other where the CNT and the TES can be hosted. (c) The schematic shows a section of the MIC setup with the circuit elements for the CNT emission characterization. When negative voltage is applied to the CNT chip and the electric field exceeds the threshold, a current is measured from the copper plate in front of the CNTs. (d) Emission current from CNTs measured in the MIC at 3 K for three different samples.

chip is glued inside a groove on one of the copper plates, making the tips of the CNTs level with the copper plate. The distance between the two copper plates can be varied depending on the number of sapphire spacers used.

The shape of this mounting resembles the traditional Italian dish called "Mozzarella in Carrozza," so from now on, we will refer to it as MiC.

As shown in the schematic in Figure 4.8(b), for the characterization of the current emitted by the CNTs, one of the two plates is connected to a variable voltage source while the other is connected to an ammeter. Both voltage and current measurements are performed with the same instrument, the Keithley 6487. Since the silicon substrate becomes an insulator at low temperatures, the electrical contact between the CNTs and the copper plate is made via Al wire bonding.

This simple setup can be mounted on the 3 K plate as well as on the 30 mK plate. Moreover, in the same setup, a TES chip can be mounted with wire connections to the SQUID box for TES reading. An example of three different emission curves from three different samples is shown in the plot in panel (d) of Figure 4.8. Different samples have been tested, and the study at 3 K will be the subject of an upcoming paper. From the 3 K characterization, we achieved emission from CNTs from 50 V to 500 V.

The integration of the CNT with the TES device will be further discussed in Section 5.2.

4.6 Fabrication Facility at INRiM

The working principle of TES is based on the superconducting transition of a metallic film. The fabrication of superconducting metallic films is a complex process that requires a cleanroom environment and an Ultra-High Vacuum (UHV) deposition system. As shown in Table 2.2, various materials have been used as superconducting films for TESs, each necessitating specific deposition techniques and careful handling. During my PhD, I did not actively participate in the fabrication of the TES devices I used, so I will only outline the main aspects of the fabrication process here.

At the QR Lab in INRiM, the available deposition system and extensive experience focus on the fabrication of Titanium-Gold (TiAu) TES [139]. Titanium serves as the superconducting material, while gold acts as a normal metal. A TiAu bilayer is used to exploit the proximity effect and tune the critical temperature of titanium [140]. Pure titanium has a critical temperature of approximately 510 mK [141]; by depositing a layer of gold on top of titanium, this value can be tuned down to a point where the superconducting state is no longer reached [28].

The deposition of TiAu TES at the INRiM facility is performed in a UHV chamber by thermal evaporation, at a pressure lower than 5×10^{-9} mbar, on silicon substrates covered with 140 nm of thermal silicon oxide and 500 nm of LPCVD silicon nitride. Before introducing the substrate into the deposition system from the load-lock, its surface is ion milled to remove contaminants. After the deposition of titanium, a waiting time of less than 10 seconds is used before the deposition of gold to minimize oxidation on the titanium surface [139].

The TES requires wiring to connect to the SQUID readout. Superconducting wiring with a higher T_C than the TES bilayer is used. Niobium (Nb) and aluminium (Al) are two materials with bulk critical temperatures of 9.2 K and 1.2 K, respectively. The Nb or Al films are deposited in a UHV DC magnetron sputtering system at a base pressure of 10^{-8} mbar. Before deposition, in situ cleaning of the substrate by sputter-etching removes contaminants from its surface. Sputtering is performed at an argon pressure of 5×10^{-3} mbar.

Chapter 5

Results

This chapter presents the key findings and advancements made in the development and characterization of TES at INRiM and PTB Braunschweig. The research focuses on enhancing the performance of TES in different aspects such as energy resolution, electron detection, dark counts rate, and system detection efficiency.

The first section, **Energy Resolution**, details the progress at INRiM in improving the energy resolution of TES devices. These efforts are crucial for the PTOLEMY project, which aims to detect relic neutrinos by achieving an electron energy resolution as low as 0.11 eV. We investigate two TES samples with different active areas, Lito20 (20 μm × 20 μm) and Lito50 (50 μm × 50 μm), and provide a comprehensive analysis of their performances.

The second section, **Detection of Low-Energy Electrons**, describes the first single-electron counting in the sub-100 eV range with an energy resolution of a few eV for fully-absorbed electrons. TES devices were operated in a cryostat setup with a cold electron source based on field emission from vertically-aligned carbon nanotubes. This section highlights the direct comparison between photon and electron energy resolutions, demonstrating the versatility and high resolution of TES devices for low-energy particle detection.

The third section, **Study of Dark Counts for Rare Event Searches**, investigates the dark count rates (DCR) of TES devices, which is crucial for applications in rare event searches such as dark matter detection. This study, conducted in collaboration with the Astroparticle Physics Group from New York University Abu Dhabi (NYUAD), examines the sources of dark counts and their implications for TES

performance. Various experimental setups and simulations were used to understand the impact of cosmic rays and natural radioactivity on the TES dark counts.

The fourth section, **System Detection Efficiency Measurement**, presents the results of the system detection efficiency (SDE) measurements conducted at PTB Braunschweig. During a four-month research visit, significant progress was made in setting up a cryo-optical facility and optimizing TES devices for high detection efficiency at 1550 nm. The TES devices achieved an impressive 98% SDE, demonstrating their potential for high-efficiency photon detection in quantum metrology.

The fifth section, **Preliminary Results for Fast TES**, presents the efforts to achieve TES devices with short recovery times. Two approaches were followed: working at higher temperatures and improving the thermal conductance of the TES. The use of Al TES and gold pads on TiAu TES showed promising outcomes. Al TES demonstrated potential for very short recovery times, but challenges in stability and energy resolution need to be addressed. Au pads on TES helped improve thermal conductance and recovery times, with ongoing research to optimize these designs for better performance.

The results presented in this chapter highlight the advancements in TES technology and their applications in high-precision measurements. These developments pave the way for further research and potential breakthroughs in detecting low-energy electron, achieving high-efficiency photon detection, and exploring rare event phenomena.

5.1 Energy resolution

In this section, I present the significant progress made at INRiM in enhancing the energy resolution of transition-edge sensors (TES). This work is crucial for the PTOLEMY project, which aims to detect relic neutrinos for the first time. The goal for TES in this context is to achieve an electron full width half max (fwhm) energy resolution as low as 0.11 eV [26]. Our current objectives focus on two main aspects: optimizing the energy resolution of TES while maintaining the largest possible active area and demonstrating the capability of TES detectors to detect electrons, which will be detailed in Section 5.2.

Here, I present results from two TES devices with different areas: one with 20 μm × 20 μm and another with 50 μm × 50 μm. While optical TES devices with energy resolutions of 0.11 eV or better have already been fabricated [17, 18], they typically have smaller active areas of 8 μm × 8 μm and 10 μm × 10 μm, respectively.

A larger TES area is advantageous for the PTOLEMY project because it simplifies the development of TES arrays. For instance, to cover the same area, only one 50 μm × 50 μm TES is needed compared to 25 10 μm × 10 μm TES devices. This significantly reduces the complexity and increases the feasibility of deploying large-scale TES arrays.

As discussed in Section 3.5.1, the energy resolution of a TES scales with the critical temperature and active area as $T_C^{3/2}A^{1/2}$. Thus, our strategy involves lowering the critical temperature to compensate for the larger active area [28]. This section summarizes the results obtained from two samples: 'Lito20' with an area of 20 μm × 20 μm and 'Lito50' with an area of 50 μm × 50 μm. Both Lito20 and Lito50 do not have any anti-reflection coatings because, in the context of the PTOLEMY project, enhancing photon absorption is unnecessary. Moreover, any dielectric on top of the TES would prevent electron detection. Therefore, the TES devices we are developing are composed solely of the TiAu bilayer.

5.1.1 Lito20 TES

We fully characterized a TiAu TES with an area of 20 μm × 20 μm made by depositing 30 nm of Au on top of 12 nm of Ti, as discussed in Section 4.6. The first

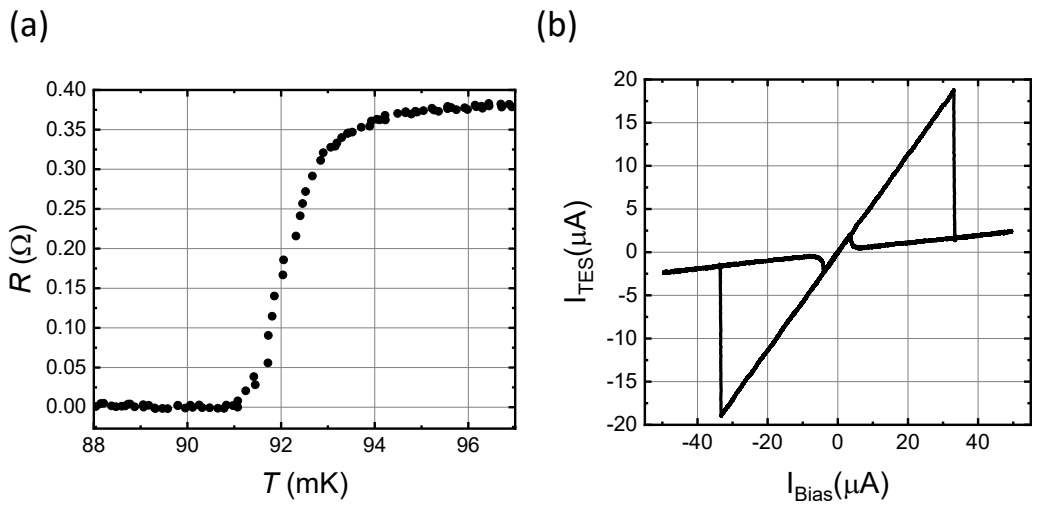

Fig. 5.1 Electrical characterization of the Lito20 TES. Panel (a): R vs T curve with a constant current of 1 μA. Panel (b): Complete I_{TES} vs I_{Bias} curve at 67 mK.

step involved measuring the superconductive transition using a 4-wire circuit with an AC-resistance bridge at a constant current of 1 μA. The data of the superconducting transition are displayed in Figure 5.1(a). We measured a $T_{\mathrm{C}} = 92$ mK and a $\Delta T_{\mathrm{C}} = 2$ mK, where ΔT_{C} is defined as the temperature range between the TES being at 90% and 10% of its R_{N}.

The second step in the characterization involved installing the TES in the SQUID setup described in Section 4.2. Before this step the TES was coupled with a single mode fiber (SMF) with a core diameter of 9 μm using the alignment system described in section 4.3. With the TES in the SQUID setup, we were able to proceed with the electrical characterization. We acquired a full I_{TES} vs. I_{Bias} curve for both negative and positive bias currents at 67 mK, as shown in Figure 5.1(b). The curve was obtained using the current source (I_{Bias}) provided by the Magnicon electronics [120] with a triangular AC signal between -50 μA and +50 μA at a frequency of $\sim$ 20 Hz. The values of I_{TES} were calculated from the output of the SQUID electronics with the transimpedance amplification reported in Table 4.1. From this curve, it is evident that the response is symmetric, suggesting that the residual magnetic field perpendicular to the TES area is negligible. Given this, we continued the characterization by measuring the curve at different bath temperatures, but only for the normal branch with positive current to avoid the saturation of the FLL electronics. These curves, shown in Figure 5.2 (a), allow the calculation of the power dissipated by the TES to

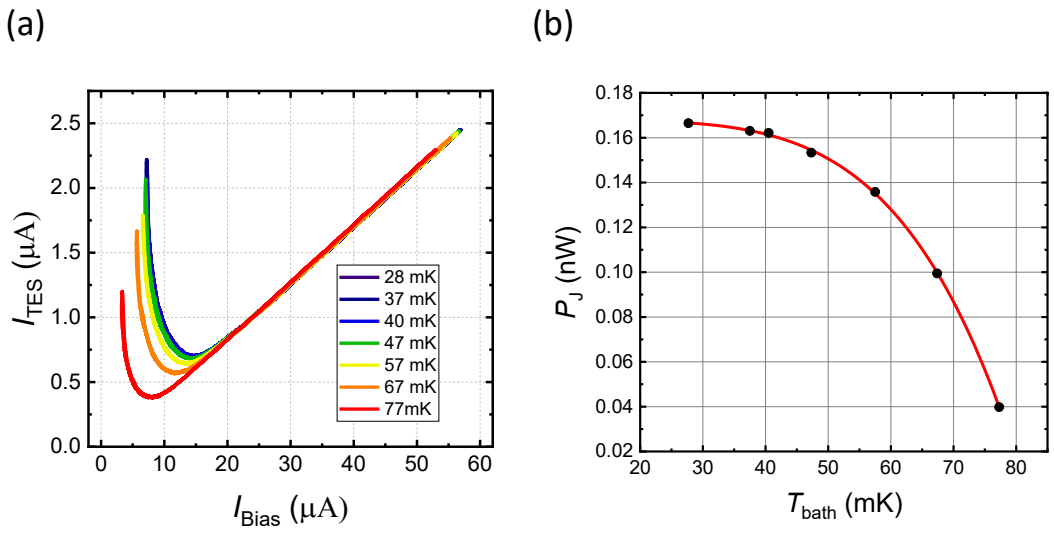

Fig. 5.2 Panel (a): Normal barnch for postive current of the I_{TES} vs I_{Bias} curves at different bath temperatures. Panel (b): Joule power dissipated to the thermal bath when the TES is operated at $R_0 = 20\%\ R_N$.

the thermal bath at different bath temperatures for a fixed working point. An example of the power curve is shown in Figure 5.2 (b). The black dots are the experimental data measured for $R_0 = 20\%\ R_N$. The red curve represents the fit results using the power dissipation model to the substrate described in Section 3.2, equation 3.4:

$$I_0^2 R_0 = P_J = \kappa(T_C^n - T_{bath}^n) \tag{5.1}$$

From the fit, we obtained $\kappa = (1.7 \pm 0.4) \times 10^{-9}$ W/K^n and $n = 4.6 \pm 0.1$, corresponding to a thermal conductance $G = n\kappa T_C^{n-1} = 9.6 \pm 0.5$ pW/K.

Photon Number Resolution Capability

To measure the energy resolution and verify the photon number resolution capability of the Lito20 TES, we coupled light from a monochromatic pulsed laser emitting at 1540±10 nm into the fiber. The laser pulses had a duration of approximately 70 ps and were emitted at a repetition rate of 1 kHz, which is sufficiently low to allow the TES to fully recover between pulses. Before entering the cryostat, the light passed through an attenuated path to reduce the power to a few fW, ensuring only a few photons per pulse.

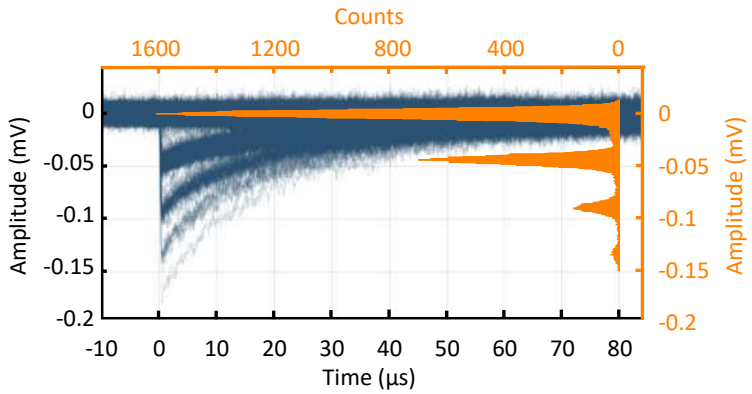

Fig. 5.3 Photon number resolution characterization. The blue traces represent 1000 waveforms recorded with the oscilloscope in persistence mode, showing quantized amplitude levels corresponding to different numbers of absorbed photons. The flat line at 0 V corresponds to no photon absorption by the TES, while the thicker pulses with minima around -0.05 V, -0.1 V, and so on, correspond to the absorption of one, two, and three photons, respectively. The orange plot shows the histogram of counts for the minimum value of each recorded waveform over 50,000 waveforms. The histogram reveals four Gaussian peaks corresponding to $i = 0, 1, 2, 3$ photons. The amplitude of these peaks follows Poisson statistics, and the fwhm is proportional to the energy resolution of the device.

The TES was operated with the bath temperature stabilized at 40 mK or lower, and it was biased at its transition to a working point (R_0, I_0). The SQUID was used in FLL mode, with its output connected to an oscilloscope. The oscilloscope was triggered by the TTL output of the laser. When the laser output is enabled, each oscilloscope trigger corresponds to a pulse reaching the TES. Since the photons arrive at the TES within 70 ps of each pulse, we can assume the absorption of n-photons is simultaneous, as the arrival time separating photons from the same pulse is much shorter than the shortest characteristic time of the TES.

The probability distribution for a number of photons i in a pulse, given an expected mean number μ, is described by the Poisson distribution:

$$P(i,\mu) = \frac{\mu^i}{i!} e^{-\mu} \tag{5.2}$$

The energy absorbed by the TES from each laser pulse is directly proportional to the number of photons in the pulse. Since photons are discrete quanta of energy, the amplitudes of the signal output from the SQUID amplifier should also be discrete, reflecting the number of absorbed photons. The blue traces in Figure 5.3 represent

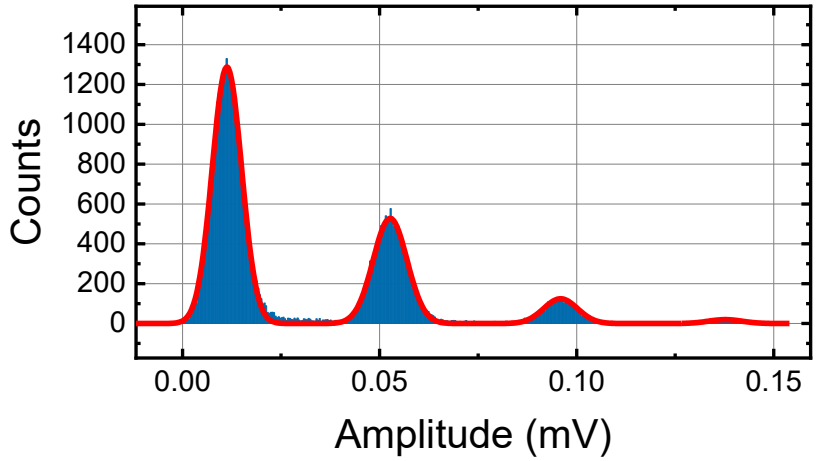

Fig. 5.4 Histogram of amplitude signals form the TES generated by a 1540 nm pulsed laser without filtering. the red line is the fit from equation 5.3, the mean photon is $\mu = 0.5$.

1000 waveforms recorded by the oscilloscope in persistence mode. The quantized maximum amplitude of the waveforms is visible in the darker ragion of the plot where most of the waveforms overlap. The flat line at 0 V corresponds to waveforms recorded when no photons were absorbed by the TES. The darker peak with a minimum around -0.05 V corresponds to the absorption of one photon. The peak with a minimum around -0.1 V corresponds to the absorption of two photons, and so on. The orange plot in the same figure shows the histogram pulse amplitude using the minimum of each waveform recorded by the oscilloscope for 50,000 waveforms. The histogram reveals four Gaussian peaks corresponding to $i = 0, 1, 2, 3$ photons. The amplitude of the peaks follows Poisson statistics, and the fwhm is proportional to the energy resolution of the device. To measure the energy resolution, we fit the histogram with a function that is a sum of Gaussians with amplitudes depending on Poisson statistics:

$$\text{Count}(V) = A\frac{e^{-\mu}}{\sqrt{2\pi}}\sum_{i=0}^{3}\frac{\mu^i}{i!}e^{\frac{-(V-x_i)^2}{2\sigma_i^2}} \tag{5.3}$$

where μ is the expected number of photons according to Poisson statistics, i is the number of photons, x_i is the center of the Gaussian peak for the i-th photon, and σ_i is its standard deviation. Since only four Gaussian peaks are visible, the summation goes from $i = 0$ to $i = 3$. An example of this fit is shown in Figure 5.4.

The data were taken with the TES at $R_0 = 0.15R_N$ and no filter applied. From the fit parameters, we calculate the energy resolution at the energy of the i-th photon

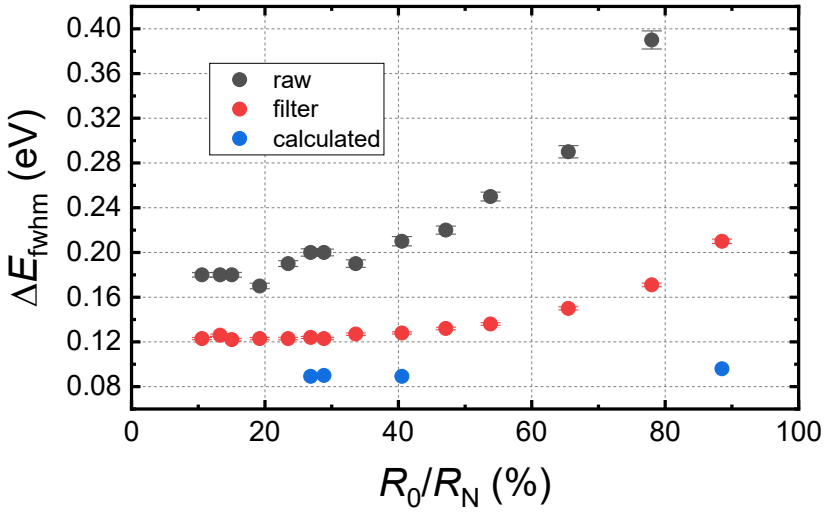

Fig. 5.5 Energy resolution of Lito20 at 0.8 eV as a function of the working point R_0.

number as:

$$\Delta E_{\text{fwhm}}(\text{at } E = \frac{hc}{\lambda} i) = 2\sqrt{2\ln 2}\frac{hc}{\lambda}\frac{\sigma_i}{(x_{i+1} - x_i)} \tag{5.4}$$

For this case, at the energy corresponding to 1 photon ($i = 1$), $E = \frac{hc}{\lambda} \cdot i = 0.805$ eV with the fit parameters:

$$x_1 = 0.05266 \pm 0.00004 \text{ V},$$
$$x_2 = 0.0959 \pm 0.0001 \text{ V},$$
$$\sigma_1 = 0.00428 \pm 0.00004 \text{ V},$$

The energy resolution is calculated to be:

$$\Delta E_{\text{fwhm}}(\text{at } E = 0.8 \text{ eV}) = 0.188 \pm 0.002 \text{ eV}$$

The uncertainty on this value is calculated as discussed in [18].

As discussed in Section 3.5.1, the energy resolution depends on the chosen working point. The black dot in Figure 5.5 shows the change in energy resolution for varying working points when no filter was applied. The energy resolution can be improved by filtering the waveform; for this sample, the most effective filter was found to be a low-pass filter at 200 kHz built into the oscilloscope. The red point in Figure 5.5 represents the energy resolution measured after applying the

low-pass filter. The improvement is around 35% for low R_0 but can be as much as 65% for higher R_0. The blue dot in the graph represents the expected energy resolution calculated from the noise measurement. This calculation, detailed in the next section, involves measuring the complex impedance of the TES to extract important parameters such as α, β, and the loop gain $\mathscr{L}$.

Impedance and Noise Measurements

The technique of measuring the complex impedance to extract TES parameters is well established [142–145, 17, 146, 147]. The complex impedance can be expressed as [1]:

$$Z_{\mathrm{TES}}(\omega) = R_0(1+\beta) + \frac{R_0\mathscr{L}}{1-\mathscr{L}} \frac{2+\beta}{1+\mathrm{i}\omega\frac{\tau_{\mathrm{th}}}{1-\mathscr{L}}} \tag{5.5}$$

The measurement is performed by injecting a small amplitude signal with a lock-in amplifier up to 250 kHz and reading the output through the SQUID amplifier. The analysis method involves first measuring the complex impedance in both the superconducting and normal states to extract the transfer function, similar to the approach described in [146].

Considering the circuit in Figure 3.6, the Thevenin equivalent voltage across the bias circuit is given by:

$$V_{\mathrm{th}}(\omega) = (Z_{\mathrm{TES}} + R_{\mathrm{L}} + \mathrm{i}\omega L) I_{\mathrm{TES}} \tag{5.6}$$

where R_{L} is the load resistor and L is the inductance in series with the TES. Since it is difficult to build an equivalent circuit from the input of the lock-in to isolate V_{th}, a transfer function is used:

$$V_{\mathrm{th}}(\omega) = F(\omega) V_{\mathrm{in}}(\omega) \tag{5.7}$$

where $F(\omega)$ is the transfer function and $V_{\mathrm{in}}(\omega)$ is the input voltage from the lock-in amplifier. Assuming that the transfer function is independent of the working point, we use the superconducting and normal states of the TES to extract R_{L} and L [147]:

$$\frac{V_{\mathrm{S}}}{V_{\mathrm{N}}} = \frac{R_{\mathrm{N}} + R_{\mathrm{L}} + \mathrm{i}\omega L}{R_{\mathrm{L}} + \mathrm{i}\omega L} \tag{5.8}$$

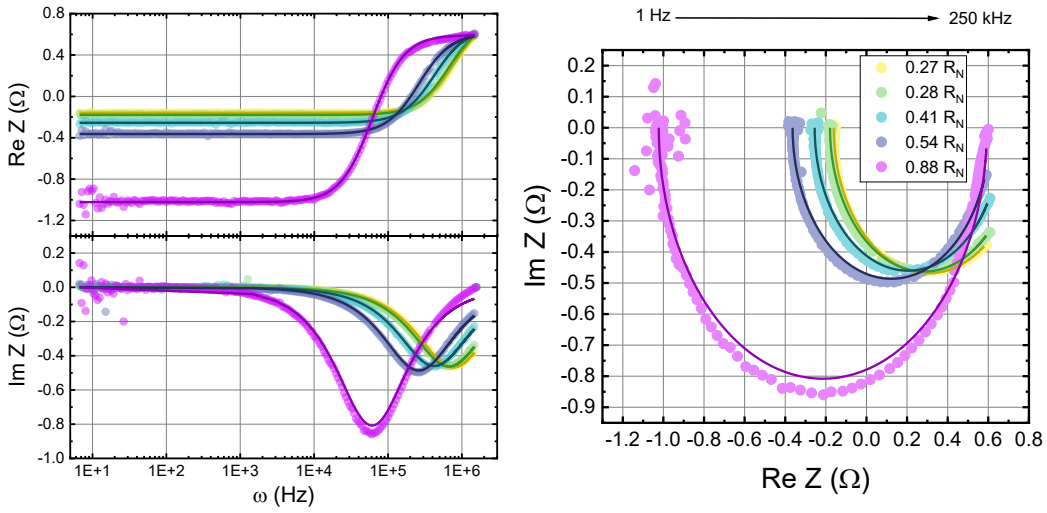

Fig. 5.6 Complex impedance measurement results up to 250 kHz: The dots represent the measured data for different TES working points, and the lines represent the fits using Equation 5.5.

where V_S and V_N are the outputs read from the lock-in amplifier in the superconducting and normal states, respectively. The transfer function is therefore:

$$F(\omega) = \frac{(R_N + R_L + i\omega L)I_N}{V_{in}} \tag{5.9}$$

where I_N is the current flowing in the TES in the normal state. The results of the measurement are shown in Figure 5.6. The dots represent the measured data for different TES working points, while the lines represent the fits using Equation 5.5.

From the fits, we obtained the current sensitivity β, the loop gain $\mathscr{L} = \alpha \frac{R_0 I_0^2}{G T_0}$ from which we can extract α, and the thermal time constant $\tau_{th} = \frac{C}{G}$ from which we obtain C. The calculated values of α and β are visible in 5.7(a) while the measured and calculated values of the effective time constant τ_{eff} are shown in Figure 5.7(b). The calculated values of τ_{eff} are obtained using the formula:

$$\tau_{eff} = \frac{C}{G} \frac{1 + \beta + \frac{R_L}{R_0}}{1 + \beta + \frac{R_L}{R_0} + (1 - \frac{R_L}{R_0})\mathscr{L}} \tag{5.10}$$

while the measured data were obtained by fitting the single photon pulse with the following function from Equation 3.44:

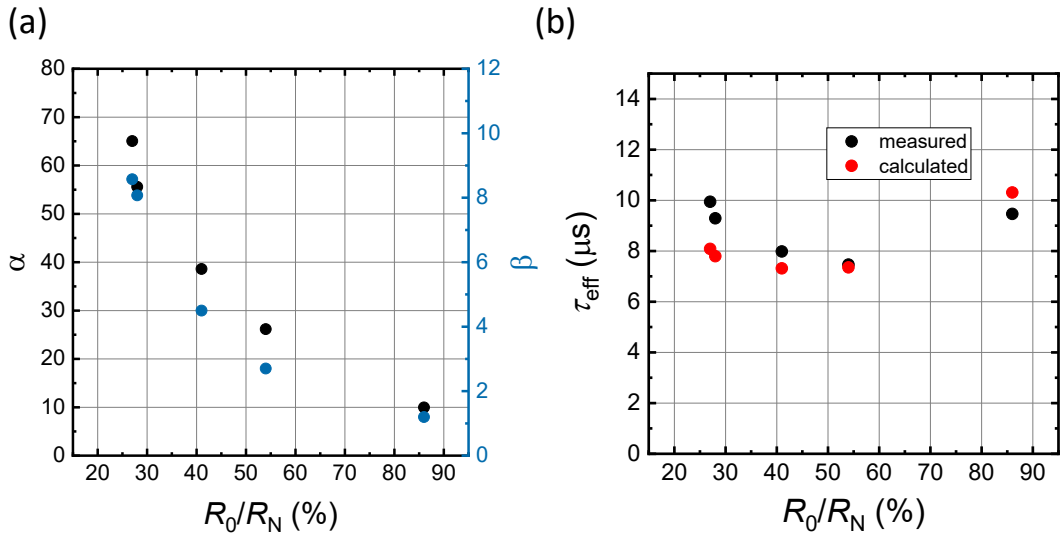

Fig. 5.7 Panel (a): Dependence of the parameters α and β on the TES working point. Panel (b): Measured and calculated values of the effective time constant τ_{eff} as a function of the TES working point.

$$V_{\text{out}}(t) = A\left(e^{-\frac{t}{\tau_{\text{el}}}} - e^{-\frac{t}{\tau_{\text{eff}}}}\right) \tag{5.11}$$

The measured and calculated values of τ_{eff} differ by up to 20% at lower R_0. While this discrepancy suggests that the model used for the impedance measurement might not fully capture the behavior of this device, the deviation is within a reasonable range. Therefore, it remains valuable to proceed with the analysis. Recalling Equation 3.48 from Section 3.5.1, the energy resolution can be estimated from the NEP as [1]:

$$\Delta E_{\text{fwhm}} = 2\sqrt{2\ln 2}\left(\int_0^\infty \frac{4}{S_{\text{P}_{\text{tot}}}(f)}\,df\right)^{-\frac{1}{2}} = 2\sqrt{2\ln 2}\left(\int_0^\infty \frac{4|s_{\text{I}}(f)|^2}{S_{\text{I}_{\text{tot}}}(f)}\,df\right)^{-\frac{1}{2}} \tag{5.12}$$

where the power-to-current sensitivity $|s_{\text{I}}(\omega)|$ in the limit of $\tau_{\text{el}} \ll \tau_{\text{eff}}$ is given by [143]:

$$|s_{\text{I}}(\omega)| = \frac{\mathscr{L}}{I_0 R_0 \sqrt{(1+\beta+\mathscr{L})^2 + \omega^2 \tau_{\text{th}}^2 (1+\beta)^2}} \tag{5.13}$$

By measuring the current noise from the TES at the same working point as the

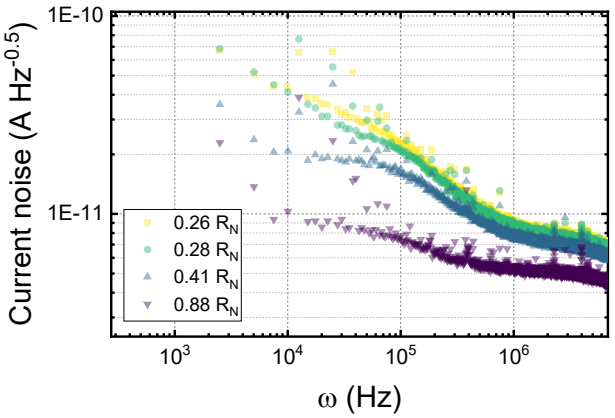

Fig. 5.8 Current noise spectra for the Lito20 TES at the same working point as the impedance measurement.

impedance measurement, we can calculate the expected energy resolution of the device. The current noise spectra is shown in Figure 5.8, where the points represent the raw data and the lines represent the smoothed data. The calculated energy resolution is shown in Figure 5.5 with the blue dots. From this data, we expect an energy resolution in the range of:

$$0.07 \text{ eV } (R_0 = 0.27R_\text{N}) < \Delta E_\text{fwhm} < 0.12 \text{ eV } (R_0 = 0.86R_\text{N})$$

Lito 20 best Energy resolution

Given the potential to achieve an energy resolution on the order of 0.07 eV, we conducted further measurements to optimize the working point, ground loop, and minimize noise sources. Ultimately, the best energy resolution we were able to obtain with the Lito20 TES was:

$$\Delta E_\text{fwhm}(\text{at } E = 0.8 \text{ eV}) = 0.114 \pm 0.001 \text{ eV}$$

The TES was biased at the 20% of its R_N, and the waveform filtered with the 200 kHz low-pass filter from the built into the oscilloscope. The histogram in Figure 5.9 (a) demonstrates this excellent energy resolution. At the same working point we measured the time constant of the TES, figure 5.9 (b) shows the average of the waveforms from one photon absorption (black dots), the red line is the fit equation

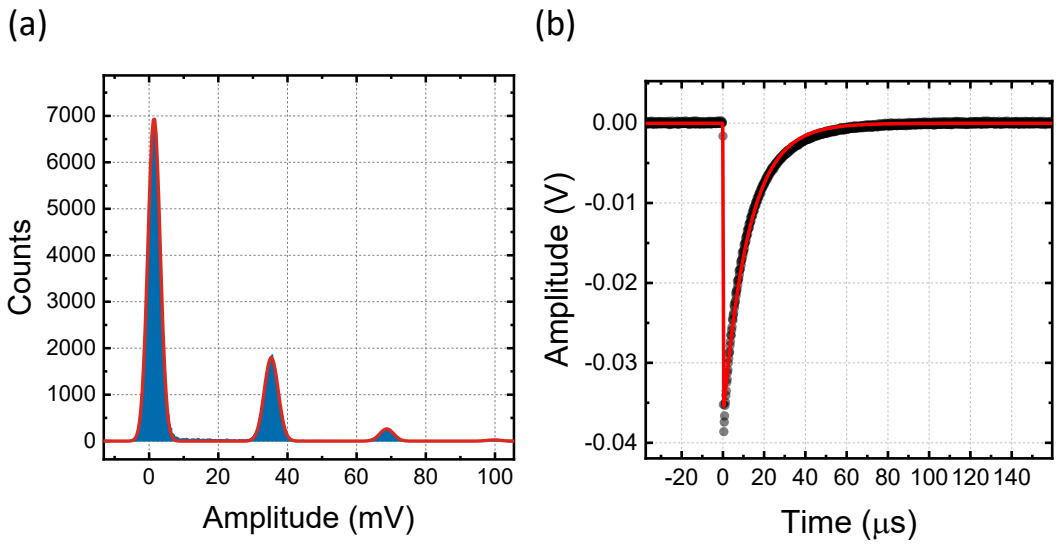

Fig. 5.9 Panel (a): Best energy resolution measured with the Lito 20. The laser wavelength was 1540 nm, and the energy resolution calculated was 0.114 eV for a single photon (0.8 eV), with a mean value (μ) of 0.47. Data was collected from 50,000 waveforms. Panel (b): Average waveform of a single photon pulse (black dots) fitted with a double exponential decay (red line). The fit yielded $\tau_{el} = 80$ ns and $\tau_{eff} = 12.5$ μs.

5.11 , the resulting time constant are:

$$\tau_{el} = 80 \pm 4 \text{ ns}$$

$$\tau_{eff} = 12.5 \pm 0.1 \text{ μs}$$

5.1.2 Lito50 TES

Here, I present the results on the energy resolution of a 50 μm × 50 μm TiAu TES named Lito50. Like Lito20, it consists of a deposition of 30 nm of Au on top of 12 nm of Ti. However, the critical temperature of this device was different, around 50 mK. The deposition of TiAu on the Lito50 chip was done the day before the chip with Lito20. We attribute this difference in T_C to the better quality of the vacuum during the Lito20 deposition, resulting in an overall better quality of Ti and Au. Additionally, this sample did not maintain the transition at the same temperature over time. Figure 5.10 (a) shows the R vs T curve of the sample at two different cooldowns. In the first cooldown (black curve), the transition was at 52 mK, while

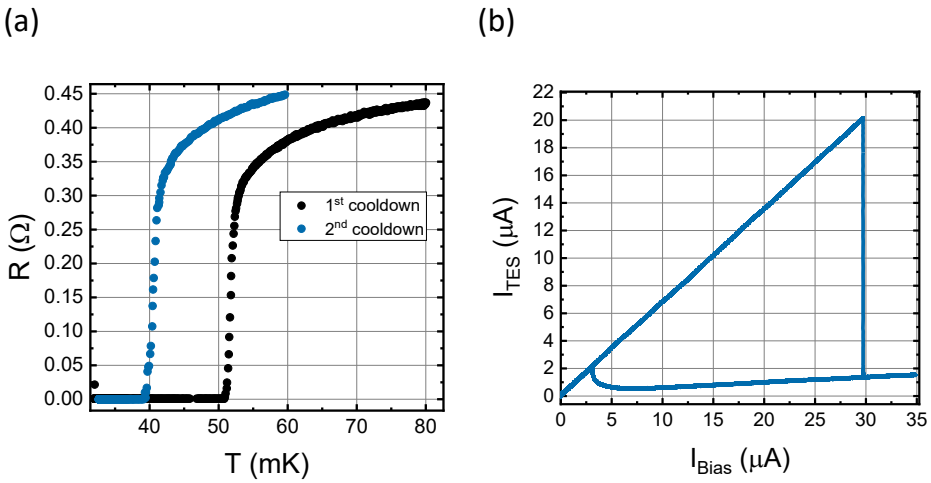

Fig. 5.10 (a) R vs T curve of Lito50 at two different cooldowns. The black curve represents the first cooldown, and the blue curve represents the second cooldown. (b) I_{TES} vs I_{Bias} curve at a bath temperature of 30 mK during the second cooldown.

in the second cooldown (blue curve), the transition was 10 mK lower, at 40.5 mK. This shift in the transition can be attributed to oxidation of the Ti or interdiffusion of the Au into the Ti [148].

Despite the observed changes over time, the very low transition temperature made this sample very promising for its energy resolution. However, the limitations of the ADR, with a minimum temperature around 30 mK, prevented operation in a strong ETF regime. Nevertheless, it was still possible to operate and partially characterize the device. The I_{TES} vs I_{Bias} curve measured in the second cooldown at a bath temperature of 30 mK is shown in Figure 5.10 (b). The TES was biased at 10% of its R_{N} and characterized with the same 1540 nm pulsed laser as in the previous section. The histogram of counts is shown in Figure 5.11 (a), along with the fitted curve. The best energy resolution was obtained filtering the raw waverfom with a winer filter as described in [149].

The energy resolution is calculated to be:

$$\Delta E_{\mathrm{fwhm}}(\text{at } E = 0.8 \text{ eV}) = 0.158 \pm 0.001 \text{ eV}$$

This value of energy resolution for a TES with this active area is unprecedented, considering also that the TES is operated near its critical temperature. The energy resolution of the device could be even better. Unfortunately, the degradation of the

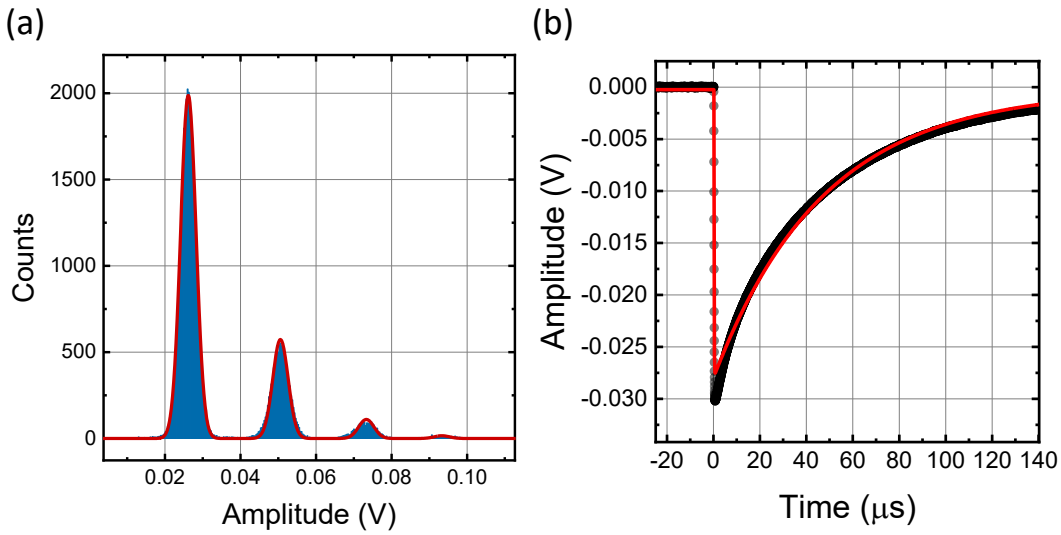

Fig. 5.11 Panel (a): Best energy resolution measured with the Lito50. The laser wavelength was 1540 nm, and the energy resolution calculated was 0.158 eV for a single photon (0.8 eV), with a mean value (μ) of 0.5. Data was collected from 50,000 waveforms and then filtered with a Wiener filter. Panel (b): Average waveform of a single photon pulse (black dots) fitted with a double exponential decay (red line). The fit yielded $\tau_{\text{el}} = 82$ ns and $\tau_{\text{eff}} = 47.3$ μs.

device was rapid and did not allow for more detailed characterization. At the same working point we measured the time constant of the TES, figure 5.11 (b) shows the average of the waveforms from one photon absorption (black dots), the red line is the fit equation 5.11 , the resulting time constant are:

$$\tau_{\text{el}} = 82 \pm 2 \text{ ns}$$

$$\tau_{\text{eff}} = 47.3 \pm 0.1 \text{ μs}$$

5.1.3 Conclusion

This section highlights the latest advancements in enhancing the energy resolution of Transition-Edge Sensors (TES) at INRiM, focusing specifically on two samples, Lito20 and Lito50. These efforts are part of the PTOLEMY project, which aims to detect relic neutrinos by achieving an electron energy resolution as low as 0.11 eV.

The Lito20 TES, with an area of 20 μm × 20 μm, demonstrated exceptional performance in line with the PTOLEMY project's goals. The device underwent comprehensive characterization, including measurements of its superconductive

transition and power dissipation. The photon number resolution capability was confirmed using a monochromatic pulsed laser at 1540 nm, resulting in an energy resolution of 0.114 ± 0.001 eV at 0.8 eV. These findings were further corroborated by complex impedance and noise measurements, ensuring the reliability of the expected energy resolution.

The Lito50 TES, with an area of 50 μm × 50 μm, also showed remarkable results. Despite experiencing degradation over time and variations in its critical temperature, it achieved an energy resolution of 0.158 ± 0.001 eV at 0.8 eV. This is a groundbreaking achievement for a TES with such a large active area, indicating the potential for even greater performance if the degradation issues can be mitigated.

Overall, the outcomes from these TES devices signify a significant advancement in developing high-resolution detectors for the PTOLEMY project and other applications requiring precise energy measurements of low-energy particles. The next critical step is to demonstrate that this level of energy resolution can also be attained for electron detection. In the subsequent section, I will discuss the results of the initial characterization of TES devices used for electron detection, revealing that in the 100 eV energy range, the energy resolution for photons and electrons is equivalent.

5.2 Detection of Low-Energy Electrons

TES devices are widely used for single-photon detection, but they can, in principle, also be used for electron detection. However, research on the use of TES devices for electron detection is currently very limited, except for a recently published result [111]. Low-energy electrons have been detected with other detection schemes, such as micro-channel plates [150], which suffer from poor energy resolution and geometrical inefficiencies due to their non-unitary fill factor. Silicon detectors, including avalanche photo-diodes [151] and silicon drift detectors [152], are characterized by the presence of a dead layer at the detector entrance, where low-energy electrons are absorbed before generating a signal.

In contrast, TES devices offer a detection scheme without dead layers and with a unitary fill factor, potentially providing high efficiency and excellent intrinsic energy resolution for low-energy electrons. This capability is of great interest for a wide range of experiments, such as the PTOLEMY project [153, 26, 27], which aims to search for the cosmic neutrino background by analyzing the endpoint of the beta decay of tritium with unprecedented electron energy resolution.

In this section, I present the first single-electron counting in the sub-100 eV range with an energy resolution of a few eV. The TES detectors were operated on the 30 mK stage of the cryostat described in Section 4.1. The electrons are produced by field emission from vertically-aligned, multi-wall carbon nanotubes (CNTs), as described in Section 4.5. This "cold-cathode source" solution overcomes the issues associated with interfacing standard hot-filament-based electron sources with TES devices operating at cryogenic temperatures, thus allowing the source to be placed directly inside the cryostat close to the TES. The measurements were carried out at the INRiM laboratory in collaboration with Dr. Francesco Pandolfi and colleagues from INFN Rome and Sapienza University of Rome within the PTOLEMY project. At the time of writing, the results presented in this section are under peer review, and a preprint can be found in [110].

5.2.1 TES Chip Design for Electron Detection

The TES device used has an area of 100 μm × 100 μm, and is a TiAu bilayer device, composed of a 15 nm layer of titanium covered by a 30 nm layer of gold, fabricated

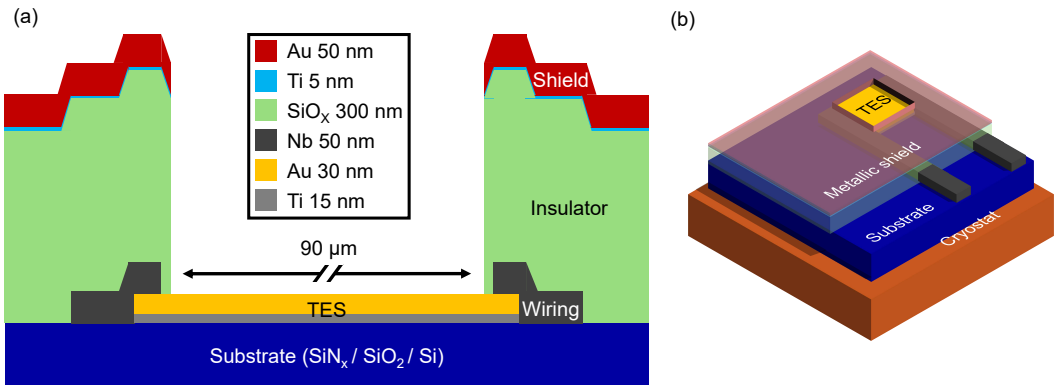

Fig. 5.12 TES layout for electron detection. (**a**): Schematic view of the TES device and its shielding layer (y-axis is to scale, x-axis is not to scale). (**b**): 3D model of the TES chip.

as described in Section 4.6. The TES has a critical temperature $T_C = 84$ mK. This TES design was adapted for electron detection by adding a shielding layer, which is necessary because the electron source has a significantly larger area (approximately 3 mm $\times$ 3 mm) compared to the TES active area (100 µm $\times$ 100 µm). The shielding layer is produced by thermal evaporation, depositing an insulating layer consisting of 300 nm of amorphous silicon oxide (SiO_x) [154], followed by a thin (5 nm) layer of titanium, and finally a 50 nm layer of gold. The thin titanium layer is necessary for optimal adhesion of gold to the SiO_x. A schematic cross-section of the layers composing the TES and the shield is shown in panel (a) of Figure 5.12, while panel (b) presents a schematic 3D model of the setup.

5.2.2 Optical Characterization

The TES was characterized with 406 nm photons. The optical characterization was performed using free space alignment. The fiber was placed in front of the TES, passing through a hole in the top copper plate of the MiC setup described in Section 4.5, as shown in the left panel of Figure 5.13. The results of this characterization, within the energy range relevant to this work, are displayed in the right panel of Figure 5.13: the peaks corresponding to photon numbers $N_\gamma = 31$, 32, 33, and 34 are clearly distinguishable and have been fitted with a sum of Gaussian functions, the energy resolution for photons is in the 2.5-3 eV range. During the optical characterization, a negative voltage was applied to the plate in front of the TES to

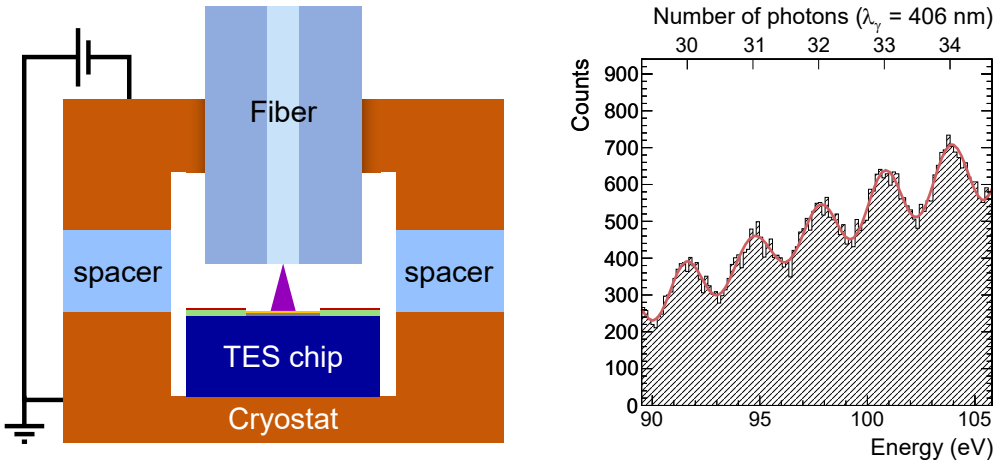

Fig. 5.13 Left panel: Schematic of the MiC setup used for optical characterization, with the fiber aligned in front of the TES. Right panel: Results of the TES optical characterization with $\lambda_\gamma = 406$ nm photons. The histogram of the pulse amplitudes shows peaks corresponding to photon numbers $N_\gamma = 31$, 32, 33, and 34, which are distinguishable and fitted with a sum of Gaussian functions (red line). The energy resolution for photons is in the 2.5-3 eV range.

test the effect of the electric field on TES performance. No significant difference was observed.

5.2.3 Single Electron Counting

Following the optical characterization, the TES and CNTs were arranged on the MiC setup. The two copper plates facing each other, were separated by 0.5 mm sapphire spacers, ensuring electrical insulation and good thermal conductance. The top copper plate, hosting the CNTs, was connected to a power supply and provided with a negative voltage V_{cnt} to produce field-emission electrons. The bottom plate was in thermal contact with the cryostat and electrically grounded through it. The distance between the tips of the CNTs and the TES surface was ~ 0.5 mm. A schematic view of the setup is shown in Figure 5.14.

In field emission electrons tunnel through the potential barrier, and are therefore emitted at a potential ϕ_{cnt} below the vacuum level, where ϕ_{cnt} is the work function of the CNTs [155]. Additionally, the difference between the work functions of the CNTs and the TES will create an effective field which will further correct the kinetic

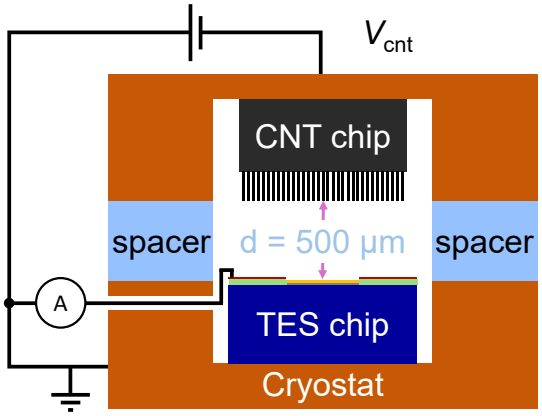

Fig. 5.14 MiC setup with the CNTs in the top copper plate,the tips are positioned 500 µm from the TES mounted on the bottom plate. The voltage to the CNTs is supplied by the Keithley 6487. The picoammeter port of the same instrument is wired to the metallic shield surrounding the TES.

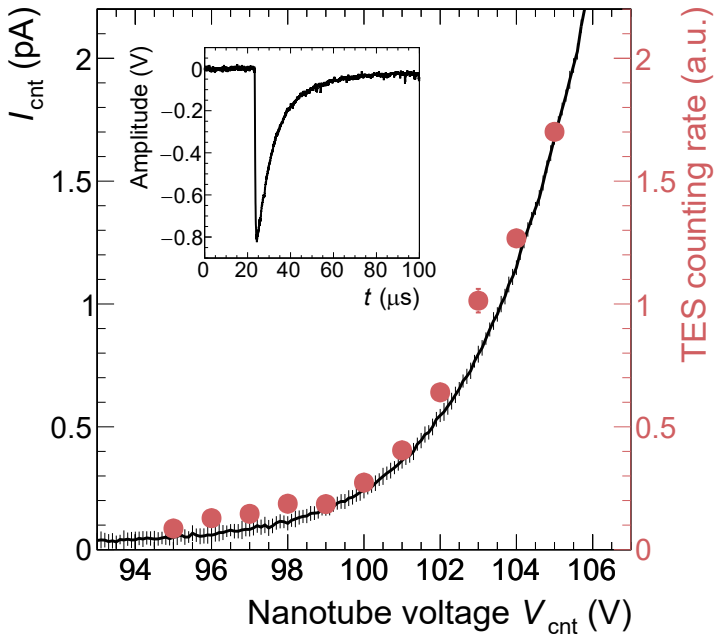

Fig. 5.15 Current I_{cnt} emitted by the nanotube source (black curve, left vertical scale) as a function of the negative voltage V_{cnt} applied to it, while reading the TES and the shield in anode configuration. This is compared to the rate of counts (red markers, right vertical scale) recorded by the TES in counting configuration. The error bars for the black curve represent the standard deviation of 20 current acquisitions at each V_{cnt}, while for the red markers, they are propagated from $\sqrt{\text{Counts}}$. The inset shows a typical TES pulse shape for $V_{cnt} = 100$ V with a recovery time of approximately 100 µs.

energy of the electrons E_e. In formulas:

$$E_e = eV_{cnt} - \phi_{cnt} + (\phi_{cnt} - \phi_{tes}) = eV_{cnt} - \phi_{tes} \tag{5.14}$$

where e is the elementary charge. The TES work function was measured with ultraviolet photoemission spectroscopy in Roma Tre University's LASEC lab, obtaining $\phi_{tes} = 4.38 \pm 0.03$ eV. Moreover, the source is monochromatic, as the energy spread of the field-emitted electrons is negligible with the values of temperature and electric field of our setup [156].

The electron emission from the CNTs was read out in two configurations. In the 'anode' configuration, the TES was short-circuited to the metallic shield layer, and both were used as a large-area metallic plate connected to the Keithley 6487 picoammeter to measure the current I_{cnt} emitted by the nanotubes. As shown in Figure 5.14, the shield is connected to the picoammeter before going to ground.

In the 'counting' configuration, the TES was biased at working point $R_0 = 0.35R_N$ and read out with the DC-SQUID transimpedance amplifier. In this condition, the TES is sensitive to single electron events.

The results from the anode configuration are illustrated by the black curve in Figure 5.15, showing the current I_{cnt} emitted by the nanotubes as a function of V_{cnt}. The current I_{cnt} exhibits an exponential increase, consistent with the Fowler-Nordheim theory of field emission [134]. Superimposed on this plot with red markers is the count rate recorded by the TES in counting mode. The count rate also increases exponentially with V_{cnt}, mirroring the behavior of I_{cnt}. This correlation confirms that the signals detected by the TES are indeed due to electron emissions. The inset in Figure 5.15 shows a typical TES signal for $V_{cnt} = 100$ V, characterized by an electrical time constant $\tau_{el} \approx 200$ ns, and a recovery time $\tau_{eff} \approx 10$ µs.

5.2.4 Effect on the local temperature near the TES

A feature of Fowler-Nordheim emission is that the electron current depends on the electric field $|\vec{E}|$, which in our planar configuration is approximated by $|\vec{E}| = V_{cnt}/d$. Moreover, the kinetic energy of these electrons is also determined by V_{cnt}, as shown in Equation (5.14). Therefore, in our setup, the signal rate and energy are not independent parameters, as they both depend on V_{cnt}.

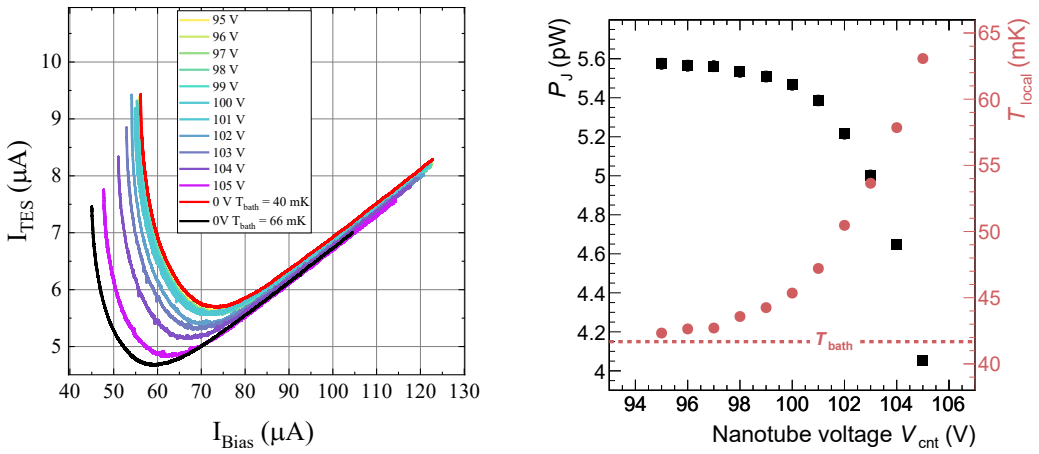

Fig. 5.16 Left Panel: I_{TES} vs I_{Bias} curve for different V_{cnt} and T_{bath}. Right Panel: Power needed to bring the TES to its working point (black markers, left vertical scale) and local temperature around the TES device (red markers, right vertical scale) for different values of V_{cnt}. The bath temperature is indicated by the red dashed line.

The electrons are emitted from a relatively large area compared to the TES, and the additional heating caused by the electrons hitting its nearby environment must be considered. When the CNTs are off ($V_{\mathrm{cnt}} = 0$) or at low V_{cnt}, the electron rate and energy deposition are minimal, keeping the temperature around the TES at the cryostat bath temperature ($T_{\mathrm{bath}} \sim 41$ mK). In this condition, the Joule power required to bring the TES to its critical temperature T_{C} is given by $P_{\mathrm{J}} = I_{\mathrm{TES}}^2 R_0 = \kappa(T_{\mathrm{C}}^n - T_{\mathrm{bath}}^n)$. For this device, the exponential parameter is $n = 4.78 \pm 0.07$ and the coupling constant $\kappa = (10 \pm 1) \cdot 10^{-7}$ WK^{-n}. However, as V_{cnt} increases, the rate of electrons and the associated energy deposition near the TES increase, raising the local temperature above the bath temperature. As a result, the local temperature T_{local} becomes higher than T_{bath} and closer to T_{C}. Consequently, less Joule power is needed to bring the TES to its working point. This effect is shown in Figure 5.16. The left panel displays the I_{TES} vs I_{Bias} curves for different CNT voltages (yellow to purple), along with two curves (red and black) where the CNTs were off, and the bath temperatures were 40 mK and 66 mK, respectively. The right panel highlights the consequence of this shift: the black markers represent the power needed to bring the TES to its nominal working point, and it can be seen that this power decreases as V_{cnt} increases. The reduction in dissipated power is interpreted as an increase in the local temperature near the TES, shown with red markers. When operating the

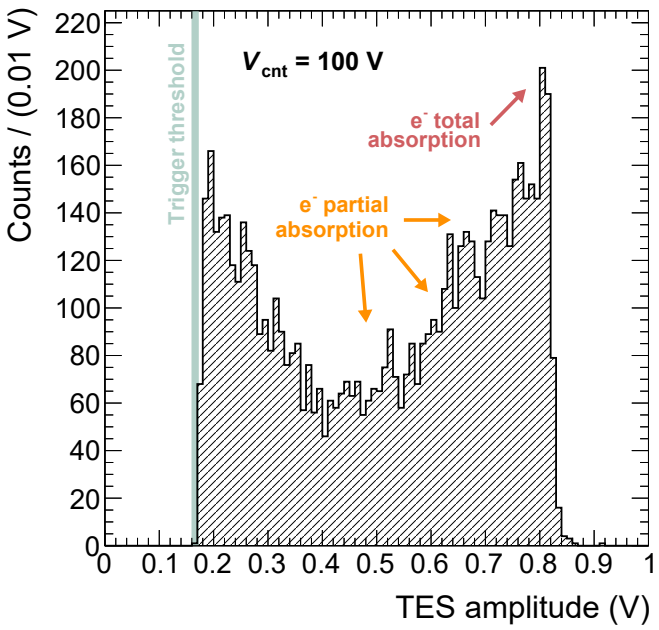

Fig. 5.17 Typical spectrum of TES signal amplitudes obtained with $V_{cnt} = 100$ V.

electron source at $V_{cnt} = 105$ V, the local temperature exceeds 60 mK, compared to the initial 41 mK before electron emission. This implies that results at different V_{cnt} values are not strictly comparable, as the TES operates under slightly different conditions.

5.2.5 Electron Spectrum and Energy Resolution

For each value of V_{cnt}, the amplitude of the TES signals were analyzed. A typical spectrum, obtained for $V_{cnt} = 100$ V, is shown in Figure 5.17: it presents a high-amplitude peak, corresponding to the full absorption of the electrons in the TES; a marked tail to the left of the peak, due to partial absorption of electrons, most likely due to electrons which fail to be stopped by the thin TES bilayer (45 nm); and a low-amplitude peak, truncated by the trigger threshold of 166 mV, compatible with electrons back-scattered out of the TES after exciting an internal mode in the Au layer.

We fit the high-amplitude peaks of these distributions with an asymmetric Gaussian function, described by its peak position x_c and its left (σ_L) and right (σ_R) tails. Fits example for $V_{cnt} = 97$, 101, 103, and 105 V are shown in Figure 5.18.

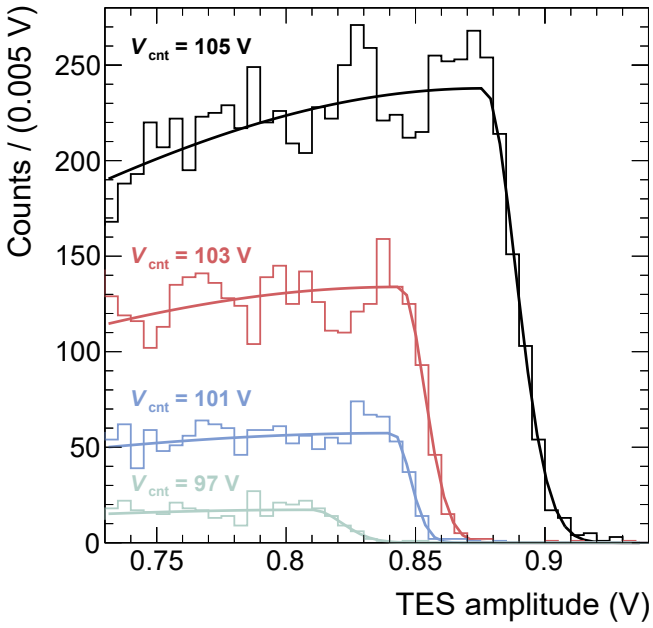

Fig. 5.18 Fits example of the high-amplitude peak histograms with the asymmetric Gaussian function for four different values of V_{cnt}.

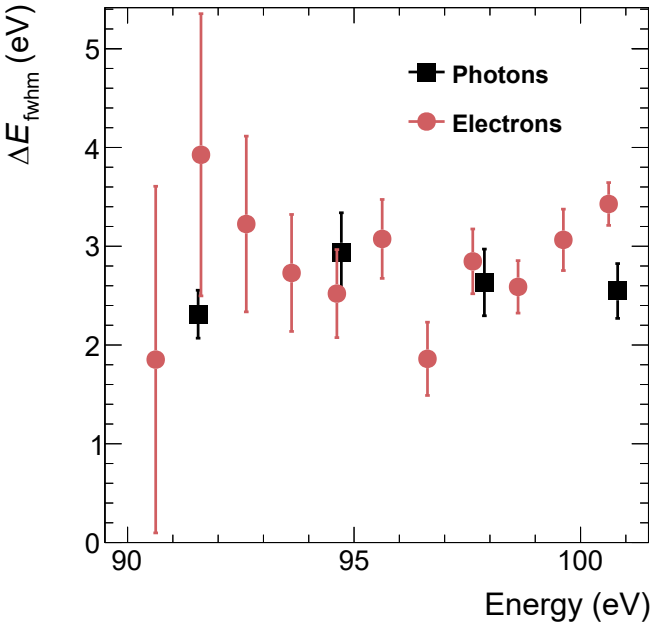

Fig. 5.19 TES energy resolution for photons (black square markers) and electrons (red circular markers) as a function of the particle energy.

Figure 5.19 shows the TES energy resolution for fully-absorbed electrons (red circular markers) and photons (black square markers) as a function of the incoming particle energy. The electron energy resolution is defined as $\Delta E_{\mathrm{fwhm}} = (2.355 \cdot \sigma_{\mathrm{R}}/x_{\mathrm{c}}) \cdot E_{\mathrm{e}}$. The parameter σ_{R} describes the uncertainty in the energy measurements for the fully-absorbed electrons. While the left tail σ_{L} is dominated by electron non-containment effects, the right tail σ_{R} is dominated by the energy resolution of the device, plus negligible effects due to the non-monochromaticity of the source. The photon energy resolution is obtained from the characterization shown in Figure 5.13. As can be seen, there is no significant difference in TES energy resolution between fully-absorbed electrons and photons in this energy range. The electron resolution, in particular, is measured to be $1.8 < \Delta E^{e}_{\mathrm{fwhm}} < 4$ eV for electrons in the $90 \leq E_{\mathrm{e}} \leq 101$ eV energy range. This is a non-trivial result, as at such low energy these particles have different interactions with matter, and suggests that the heat-based detection mechanism in the TES is the same for electrons and photons.

5.2.6 Conclusion

To conclude, this section reports the detection of low-energy electrons with a transition-edge sensor device. This achievement was made possible using a cold electron source based on field emission from vertically-aligned carbon nanotubes. We obtained an energy resolution between 1.8 and 4 eV for fully-absorbed electrons in the $90-101$ eV energy range. Notably, this resolution is comparable to the energy resolution of the same TES device for photons in the same energy range, demonstrating for the first time a direct comparison between photon and electron energy resolutions. This casts optimism on the PTOLEMY target of $\sigma_{\mathrm{e}} = 50$ meV, because this has already been achieved by these devices with photons (see Secion 3.5.1 and [18]). Clearly, to develop a high-resolution low-energy electron detector, significant work will be needed to understand the processes which broaden the left side of the absorption peak, and find solutions to limit their impact. Nevertheless, this work marks the beginning of high-resolution electron spectroscopy with TES devices.

5.3 Study of dark counts for rare event searches

It is estimated that approximately 85% of the matter in the universe consists of dark matter, a yet-to-be-discovered particle beyond the Standard Model. Dark photons, arising from extensions of the Standard Model, are one of the potential candidates for dark matter. These particles could be detected through their interaction with ordinary matter via a process known as kinetic mixing [32].

The aim of the QHaloS experiment, an upgrade of the MuDHI experiment [33], is to search for dark matter, specifically dark photons, by converting them into standard photons using a stack of alternating dielectric layers. The conservation of momentum prevents a non-relativistic dark photon from converting directly into a photon, which is inherently relativistic. However, if the medium is modified to break translational invariance, this conversion becomes possible. This detection technique is known as a "dielectric haloscope" [30]. Once a photon is generated, it can be directed to a detector and since the rate of this conversion is expected to be low, ideally the experiment should use a device capable of single-photon detection with high quantum efficiency and low dark count rate (DCR). TESs are ideal candidates for this role due to their low DCR, near unite quantum efficiency, and ability to provide information on the energy of absorbed photons.

In this section, I present the study of the dark count of TES devices conducted at the INRiM laboratory in collaboration with the Astroparticle Physics Group from New York University Abu Dhabi (NYUAD), led by Francesco Arneodo and Laura Manenti. These results are available in [16] and are currently under review for publication in the journal *Physical Review Applied*.

5.3.1 Calibration

The TES device used in this study has an area of 20 μm × 20 μm. It consists of a 12 nm layer of titanium with a 30 nm layer of gold deposited on top, on a silicon nitride substrate, as described in Section 4.6. The TES exhibits a critical temperature of approximately 90 mK and is operated inside the ADR cryostat described in Section 4.1, maintaining a stable bath temperature of 43 mK.

Calibration of the TES device was carried out using attenuated laser diodes emitting at 1540 nm, 850 nm, and 406 nm. These calibrations were performed with

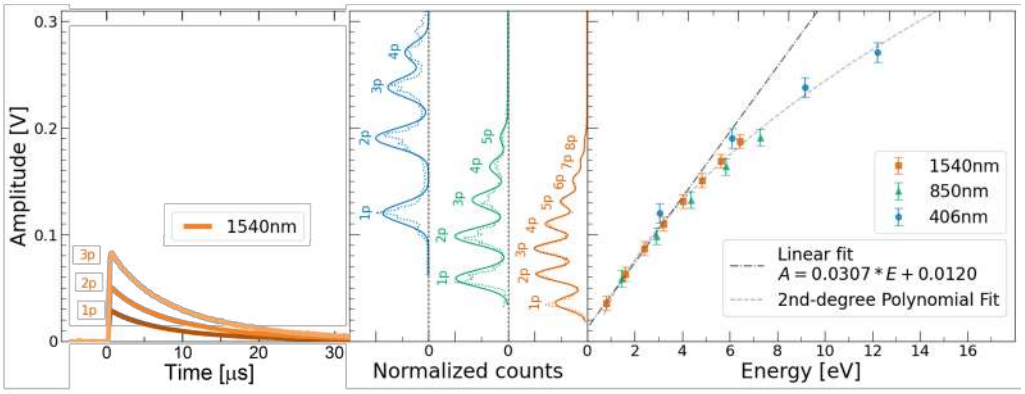

Fig. 5.20 Calibration of TES E using optically coupled, attenuated laser diodes. Left: Average pulses for the first 3 photons at 1540 nm. Center: Histograms showing the count distribution versus amplitude for each wavelength. The total number of counts in each histogram is normalized to 100. A multi-Gaussian fit (solid line) is overlaid on the raw data (dotted line). Peaks correspond to different photon multiplicities at each wavelength, with their mean values aligning with the data points in the calibration plot. The TES response is linear from 0 to 5 eV, which matches the TES's operational range. Beyond 5 eV, the response becomes non-linear. For completeness, a second-degree polynomial fit to the full energy spectrum is also shown.

free-space illumination, as the fiber was not glued in front of the TES to allow for the sensors to be fully enclosed in a box later. The sensor is referred to as "TES E". In Fig. 5.20, the calibration curve is shown on the right, where we plot the measured signal amplitude from the TES against the known energy of the impinging photon(s). The left side of the figure displays the histograms of counts versus amplitude for each laser wavelength used.

We took the absolute minimum value as the pulse amplitude from the unfiltered waveforms, intentionally avoiding any filtering during the calibration process to match the unfiltered oscilloscope conditions during data acquisition. This calibration was crucial for attributing an energy value to a pulse amplitude and for providing a reference for a typical photon-event pulse. I remained that the data acquisition was performed with the TES fully enclosed in a copper box at the 30 mK stage of the cryostat, with no optical fiber in front, in what we called dark mode (Figure 5.21).

Signals detected by a single-photon detector without any input optics are referred to as "intrinsic detector dark counts" by Ref. [40]. However, even without optics, the TES might generate signals due to external factors that can be identified and

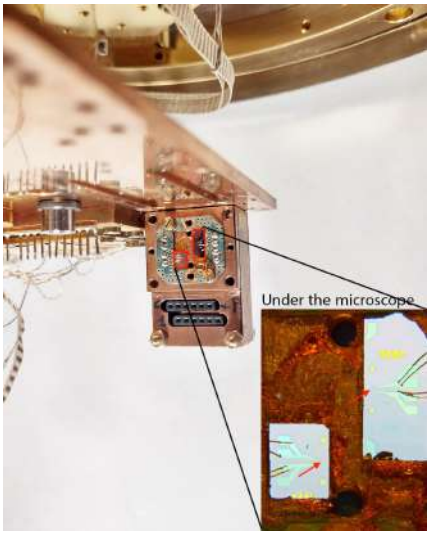

Fig. 5.21 Attached vertically to the 30 mK the TES mounted in a copper box connetect to the SQUID. On the right is a microscope zoom-in of the area within the green printed circuit board, with two TESs indicated by two red arrows, the top-right is the TES E. The TES can be closed with a copper top screwed to the box.

excluded. During preliminary observations with the TES in dark mode, we observed signals that could be categorized into three distinct types: photon-like, high-energy, and electrical noise events. Although these pulses are visually distinguishable, we have automated the categorization process using a pipeline developed in Python.

5.3.2 Classification

Our goal is to categorize each waveform from an experimental run in dark mode into three primary categories:

- **Photon-like events**: These events are similar to the signals produced by the TES when illuminated by a laser. They have amplitudes between 0 and 0.3 V, with rise and fall times consistent with those of photon signals, suggesting they are likely generated by single photons in the optical-IR range.
- **High-energy events**: These are characterized by longer rise and fall times and typically saturate the TES.
- **Electrical noise events**: These are identified by fast oscillations around the baseline, fluctuating between negative and positive values.

To classify each event in a dataset, we start by applying a second-order Butterworth filter with a frequency of 1/30 using the SciPy module [157]. We then compute several variables for each waveform, such as maximum amplitude, area, full width at half maximum, standard deviation, average positive and negative gradient, and cross-correlation with a reference photon-like event. This process maps each TES pulse recorded by the oscilloscope to a point in an n-dimensional space.

Next, we perform Principal Component Analysis (PCA) on the matrix of these n-dimensional points [158]. PCA identifies the two axes that maximize the variance among the points, allowing us to plot the pulses on these axes and typically observe distinct clusters, facilitating the differentiation of photon-like, high-energy, and electrical noise events.

We then apply K-means clustering to group pulses that are close together in the n-dimensional space [159]. This combination of PCA and K-means clustering, along with manual reanalysis of selected pulse subgroups if necessary, enables efficient pulse shape discrimination on large datasets within approximately ten minutes.

The software was developed in Python at NYUAD and is available at Ref. [160]. A graphical user interface (GUI) aids the review process by allowing the selection of a cluster center and displaying all associated waveforms for quick verification. An example of K-means clustering is shown in the top panel of Figure 5.22, where we identified nine types of events, with an example of each shown at the bottom.

Photon-like events, represented by the green points in group A in Figure 5.22, were identified by rerunning the classification algorithm on clusters 8 and 9. These signals are characterized by a sharp rise time ($\leq$1 µs) and resemble those observed when the TES is illuminated by the laser.

Signals in clusters 1–7 in Figure 5.22 exhibit long rise and fall times, suggesting they result from significant energy depositions near the TES, likely from cosmic ray particles or naturally occurring radioactive decays. We refer to these as "high-energy events." This classification aligns with the observed long rise time, attributed to the slow diffusion of energy from the surrounding area into the TES.

Electrical noise events (orange cluster B in Figure 5.22, obtained by reanalyzing clusters 8 and 9) exhibit voltage spikes oscillating between positive and negative values and have a pulse area close to zero. We attribute these events to electromagnetic

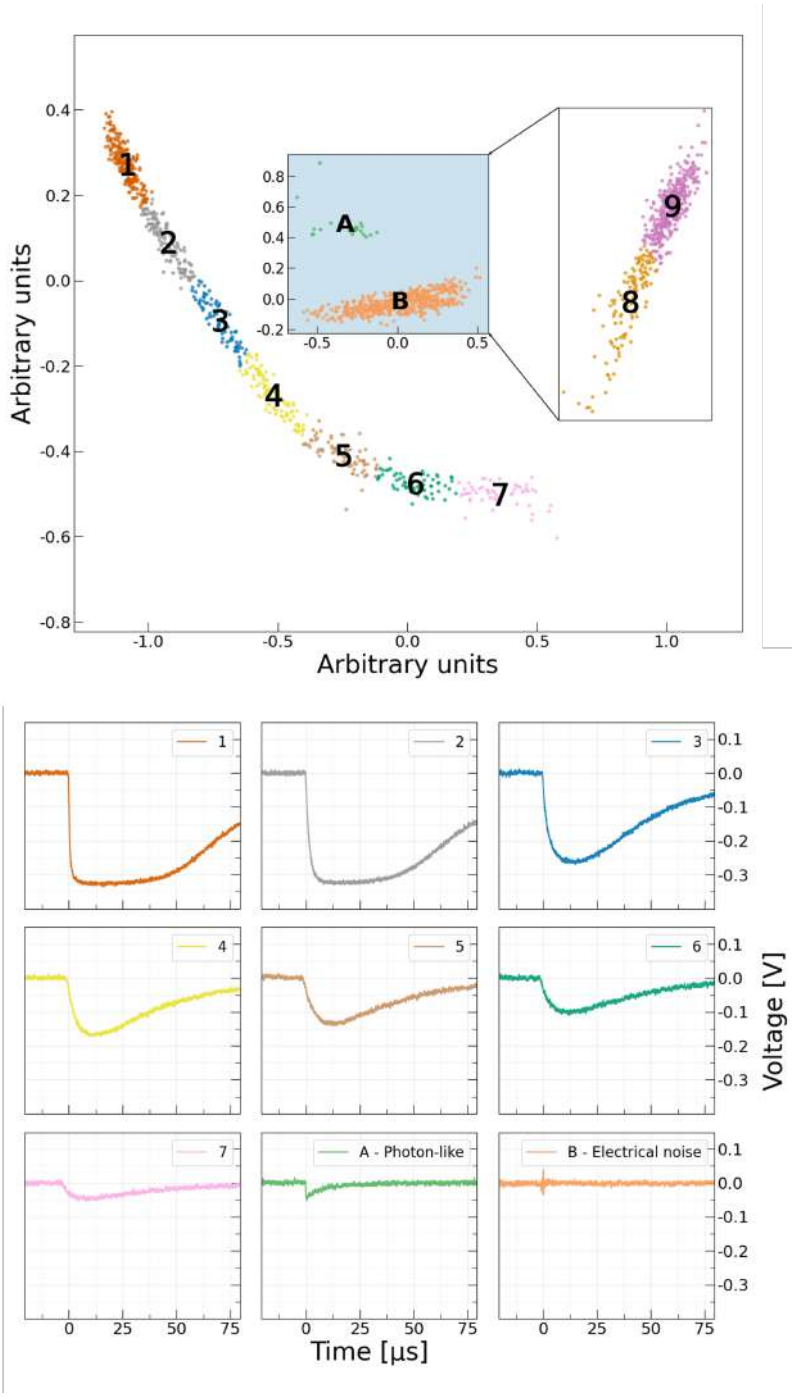

Fig. 5.22 Top panel: K-means clustering of signals from a background run after principal component analysis. The inset zooms in on clusters 8 and 9, which were reanalyzed to improve the separation of noise from photon-like events. Bottom panel: Sample signal waveforms from each of the refined clusters.

interference with the readout apparatus. Their detection even when the TES is fully superconducting indicates the issue lies outside the TES.

Our primary objective is to measure the intrinsic DCR of the TES. The PCA method effectively distinguishes photon-like events from high-energy events and electrical noise. During the QHalos experiment, these latter two types of events can be excluded, and the rate of photon-like events measured without the dielectric stack will be considered the intrinsic DCR.

The secondary objective is to gain a deeper understanding of the origins of these events and to explore potential correlations between photon-like and high-energy events. To achieve this, we conducted a series of experimental runs involving radioactive sources and coincidence measurements with cosmic rays.

5.3.3 Experimental Runs

The experimental run we conducted had the objective of measuring the intrinsic dark count and investigating the correlation between high-energy events and photon-like events.

The intrinsic photon-like DCR that we measured in the first run is on the order of 10^{-4} Hz, consistent with the findings of Ref. [15], the only preceding study of this kind. Additionally, we questioned whether cosmic rays or natural radioactive decays, interacting with either the TES or its substrate, could account for some of these photon-like events, as suggested by the same authors. To explore this possibility and gain a deeper understanding of high-energy events, which have not been extensively studied in optical TESs before, we conducted four specific tests, detailed below.

It is important to note that all experimental runs were conducted with the TES in dark mode.

Run 1: Background Test

The first run was a background test (Run 1) intended to measure the photon-like DCR. Additionally, in the same run, we measured the high-energy DCR, which we hypothesized to be caused by cosmic rays or natural radioactive decays interacting with the TES substrate.

Run 2 and Run 3: Radioactive Source Tests

In Run 2 and Run 3, we utilized two radioactive sources, ^{232}Th and ^{22}Na, respectively. These sources were positioned against the exterior of the ADR and aligned perpendicularly to the TES substrate to examine the TES's response to high-energy gamma events as shown in Figure 5.23 (a). For Run 2, we used a ^{232}Th source with an activity of approximately 10 kBq. In Run 3, we employed a ^{22}Na source with an activity of around 32 kBq. The emission spectrum of ^{22}Na is notable for its two prominent photoelectric peaks, one of which corresponds to the simultaneous emission of two back-to-back 511 keV photons. This phenomenon occurs due to electron-positron annihilation following a β^+ decay. To capture these events, the ^{22}Na source was placed between the ADR and a plastic scintillator connected to a photomultiplier tube (PMT), referred to as a "saber." This configuration allowed us to measure the double coincidences of the back-to-back gammas, detecting these occurrences with both the saber and the TES.

Run 4: Cosmic Ray Coincidence Test

For the fourth test, we aimed to demonstrate that cosmic rays can induce high-energy events in the TES. To achieve this, we implemented a cosmic ray coincidence system

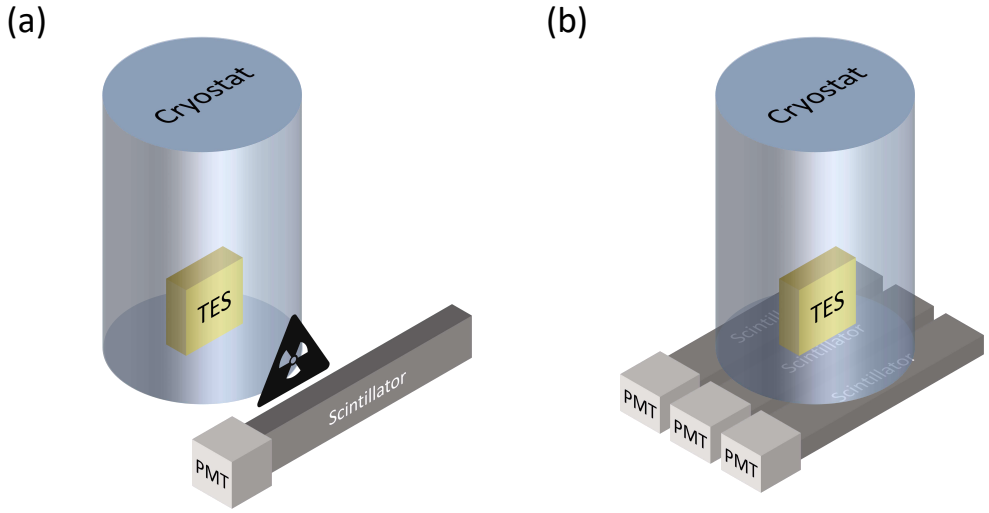

Fig. 5.23 Experimental setup showing (a) the positioning of radioactive sources ^{232}Th and ^{22}Na for high-energy gamma event detection, and (b) the cosmic ray coincidence system with three scintillators arranged beneath the ADR.

by placing three sabers side-by-side directly below the ADR, as shown in Figure 5.23(b). A simultaneous trigger of the TES and all three sabers indicated a cosmic ray shower or muon bundle event. The sabers were operated at the same gain within a 10% uncertainty, with the threshold set at 120 mV, corresponding to 250 keV.

The calibration of the sabers was performed at NYUAD using different radioactive sources and more detailed can be found in [16].

The data acquisition was conducted in two modes: in Run 4A, which lasted about 19 hours, the oscilloscope was configured to trigger on the AND signal of the three sabers, recording the TES signal simultaneously; in Run 4B, spanning around 14 hours, the trigger was set on the TES for signals greater than 0.8 eV, while recording all three sabers' outputs. Run 4A provided the ratio of quadruple coincidences (events registered by both the TES and the three sabers) to triple coincidences (events detected solely by the sabers), while Run 4B allowed us to estimate the ratio of quadruple coincidences to the total number of high-energy events detected by the TES.

5.3.4 Simulation Studies

Preliminary calculations indicated that the frequency of cosmic ray interactions directly with the TES is too low to account for the observed high-energy events. The estimated direct cosmic ray hits on a TES with an area of 20 μm × 20 μm would be approximately 10^{-2} per day, while the larger 3 mm × 5 mm substrate would receive around 10^4 hits per day. This suggests that high-energy events primarily originate from energy depositions within the substrate.

To investigate further and assess our hypothesis, GEANT4-based simulations were conducted at NYUAD for the experimental setups of Run 2, Run 3, and Run 4, using the substrate as the sensitive detector. Simulations modeled different sources, including ^{232}Th and ^{22}Na, and cosmic ray interactions using the CRY package [161]. A detailed explanation of the simulation is reported in [16].

5.3.5 Results

The key finding from Run 1 is that the photon-like DCR is 3.6×10^{-4} Hz within the energy range of 0.8 to 3.2 eV. Notably, at 1.5 ± 0.2 eV—the energy range targeted by

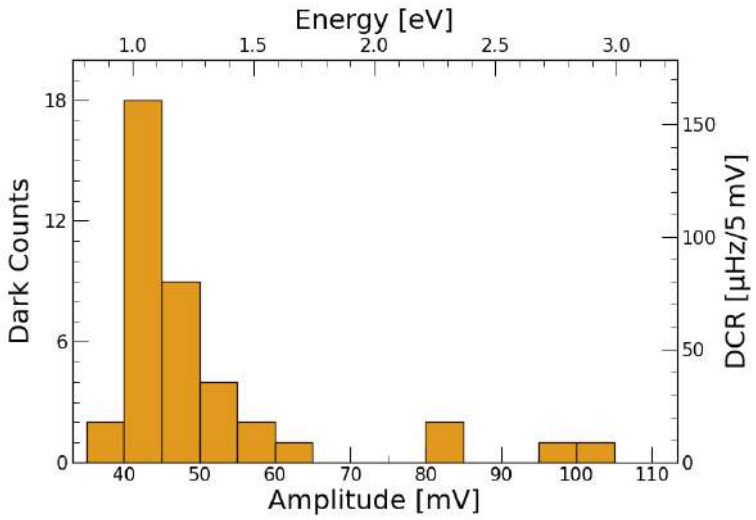

Fig. 5.24 Histogram displaying photon-like dark counts against amplitude (bottom x-axis) and corresponding energy (top x-axis) during the background run. Over 31 hours, 40 photon-like events were detected with a trigger threshold set at 0.8 eV. The rate per bin is shown on the right y-axis in μHz. The bin width of 5 mV corresponds to the standard deviation of the baseline noise.

the MuDHI dark photon dark matter haloscope detector [33]—the photon-like DCR is 6×10^{-5} Hz. Figure 5.24 shows the photon-like DCR for the TES as a function of photon energy and signal amplitude.

Contrary to initial expectations, the photon-like DCR in the 0.8 to 3.2 eV energy range remained constant (within uncertainties) across all runs (see the square points in Fig. 5.25), despite the introduction of radioactive sources in Run 2 and Run 3. This consistency suggests that high-energy gammas do not contribute to the observed photon-like event rate.

Despite including the Optical Physics package in our GEANT4 simulation, no optical photons indicative of scintillation processes around the TESs were recorded.

One potential explanation for the observed photon-like DCR is the presence of stray optical photons within the cryostat, possibly from external ambient light. However, the likelihood of these photons entering through the optical fiber seems minimal, as any ambient light entering the fiber would be absorbed by the 3 K stage to which it is fixed with copper tape. Supporting this, previous research indicates that the presence or absence of a fiber fed into the cryostat, but not directly coupled to the TES, has no significant effect on the photon-like DCR (see Fig. 4.13 in Ref. [162]).

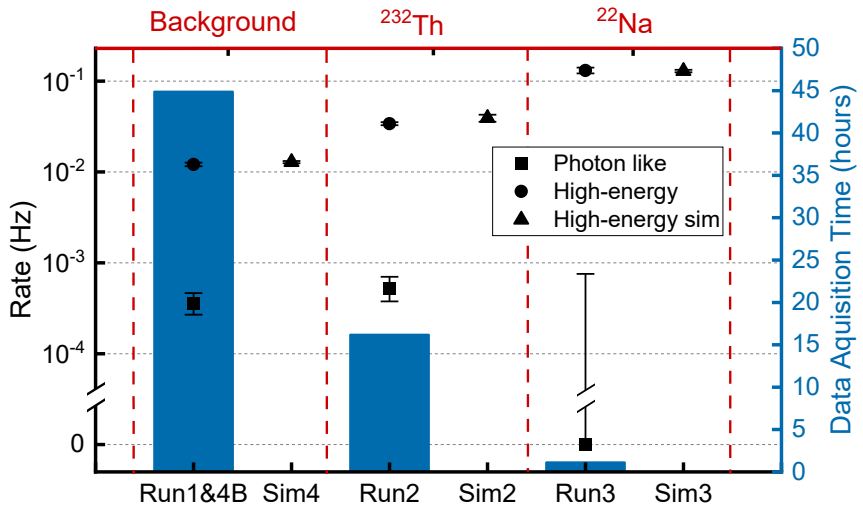

Fig. 5.25 TES count rates under different experimental configurations, namely when no radioactive source is present (background), with ^{232}Th, and with ^{22}Na. Squares are the measured photon-like rates, circles and triangles are the measured and simulated high-energy count rates, respectively.

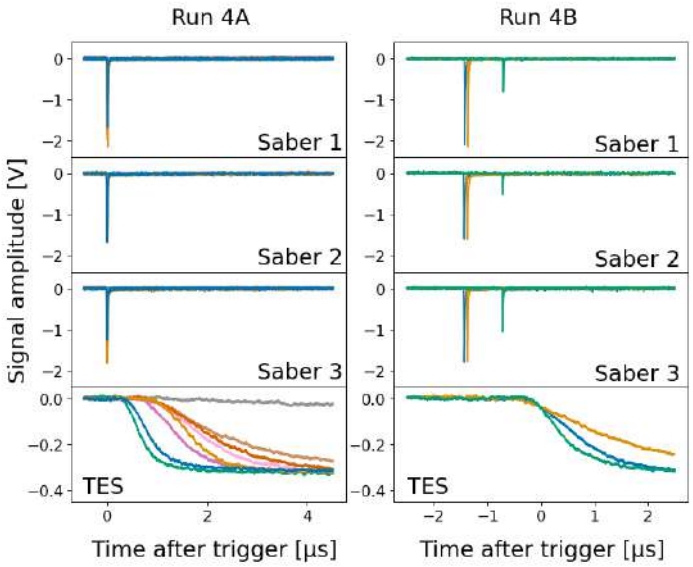

Fig. 5.26 Plots showing all quadruple coincidence events from Runs 4A (8 events over 19 hours) and 4B (3 events over 14 hours). Each color represents a specific event detected simultaneously across saber 1, 2, 3, and the TES, and is consistently used in all four corresponding plots for that event. In Run 4A, the trigger was set on the AND signal of the three sabers. Due to the TES's longer and more variable rise time and delay relative to the sabers, the saber pulses appear to overlap. In Run 4B, the time window is extended to negative values to capture saber pulses that occur prior to the TES trigger.

This suggests that the source of these photons remains unknown and requires further investigation.

In Run 1, we also selected high-energy signals to calculate the high-energy dark count rate. This rate is considered to be caused by cosmic ray interactions with the TES substrate. When radioactive sources were introduced, there was a significant increase in high-energy signals detected by the TES, particularly with the ^{22}Na source. As shown in Fig. 5.25, our simulations accurately replicated these high-energy events, producing consistent results for both ^{232}Th and ^{22}Na runs. The simulations suggest that energy is absorbed by the substrate and subsequently transmitted to the TES, where it is detected. This mechanism is further supported by the linear relationship between substrate area and DCR.

The photon-like rates could not be simulated due to their unknown origin. Background data come from Run 1, while ^{232}Th and ^{22}Na data come from Run 2 and Run 3. The simulated high-energy event rates are derived from Sim 4, Sim 2, and Sim 3, corresponding to cosmic rays and environmental gamma rays (presumed to be the predominant cause of high-energy background events), ^{232}Th, and ^{22}Na, respectively. As the simulations lack a built-in time, various time scaling factors were employed to convert simulation counts into rates. These factors include the triple coincidence rate from Run 4A, the environmental gamma rate from the NaI measurement, and the activities of thorium and sodium. The uncertainties associated with each measured data point represent the 90% confidence interval from Poisson statistics. For cases with 0 counts in Run 3, we used Feldman and Cousins [163] confidence intervals for the error bar. For the simulated rates, errors stem from the propagation of uncertainty in the time scaling factors.

Run 4 demonstrated that cosmic ray showers can generate high-energy events in the TES, as confirmed by the quadruple coincidences observed between the sensor and the three sabers below the ADR (see Fig. 5.26). The simulated ratio of triple-to-quadruple coincidences, representing the fraction of cosmic ray events detected by the saber system that also deposited energy in the TES, was higher than the observed ratio in Run 4A. Conversely, the simulated ratio of high-energy TES hits to quadruple coincidences was lower than observed in Run 4B. These discrepancies are likely due to the low statistics of quadruple coincidences and the limitations of the cosmic ray simulation. Table 5.1 provides the raw counts for triple and quadruple coincidences from both simulations and experimental data.

Table 5.1 The table compares the ratio of triple (t) to quadruple (q) coincidence events between simulation (Sim) and experimental data (Exp) for Run 4A, as well as the ratio of high-energy TES hits (h) to quadruple coincidences between simulation and experimental data for Run 4B. In Run 4A, the simulation predicts a triple to quadruple ratio that is approximately five times higher than what was observed experimentally. In Run 4B, the simulation overestimates the ratio of high-energy TES hits to quadruple coincidences, predicting a value 1.7 times higher than the experimental measurement.

	Sim	Exp	Ratio Sim/Exp
Run 4A t/q	107524/46	3818/8	5
Run 4B h/q	24906/46	963/3	1.7

5.3.6 Conclusion

We have characterized the DCR of a TiAu TES. Utilizing singular-value decomposition, principal component analysis (PCA), and K-means clustering, we effectively filtered out noise and high-energy events to isolate photon-like signals. These photon-like signals are particularly significant as they resemble the expected dark photon signal in a dielectric haloscope. We achieved a photon-like DCR of 3.6×10^{-4} Hz within the energy range of 0.8 to 3.2 eV. To achieve such a low DCR, it is crucial to eliminate optical connections between the TES and the ambient environment. However, the source of the residual photon-like events remains unexplained and requires further investigation.

Regarding high-energy events, our experimental runs using ^{232}Th and ^{22}Na sources, along with coincidence measurements between the TES and an external cosmic ray detector, coupled with detailed GEANT4 simulations, have allowed us to attribute these events to high-energy particle impacts in the TES substrate. This marks the first time such a clear attribution has been possible, as previous studies hypothesized that these high-energy events were due to radiation and cosmic ray interactions with the substrate, but lacked experimental and simulation verification. Additionally, natural radiation from materials in close proximity to the TES appears to have a negligible impact on the TES's high-energy DCR. Instead, the primary contributors to this rate are cosmic ray particles and environmental gamma rays hitting the substrate.

5.4 System Detection Efficiency Measurement

In this section, I present the results of the system detection efficiency (SDE) measurements conducted at PTB Braunschweig with Dr. Sebastian Raupach. During my third year of PhD, I spent four months as a guest researcher at PTB, working in both the Berlin and Braunschweig laboratories. In Berlin, under the supervision of Dr. Jörn Beyer, I characterized SQUIDs and deepened my understanding of these devices. In Braunschweig, I worked with Dr. Raupach to set up the cryo-optical facility for operating TESs with high SDE. Our objective was to achieve a detection system with high SDE at two different wavelengths, 930 nm and 1550 nm. Here, I discuss the results obtained at 1550 nm, where we achieved an SDE of 98%. Measurements at 930 nm are still ongoing and preliminary, so they will not be included in this thesis.

The device used is a 12 µm × 12 µm TiAu TES, fabricated by depositing 20 nm of Ti and 10 nm of Au at AIST in Japan by the group of Dr. Daiji Fukuda. The device fabrication is described in [22]. It has a T_C of 327 mK. The cavity is optimized for 1550 nm, and the fiber coupling is based on the self-aligned method similar to [101]. The fiber has a core of 3 µm to ensure good coupling with the TES active area, and the other end of the fiber is spliced to a fiber adaptor that converts the 3 µm core to a standard SMF fiber with 9 µm core with low losses. The TES is installed in an ADR cryostat and operated at approximately 100 mK. More details of the setup are reported in Section 4.4.

The schematic for the measurement of the SDE is shown in Figure 5.27. The laser light is split into two paths: one for monitoring the power with a calibrated

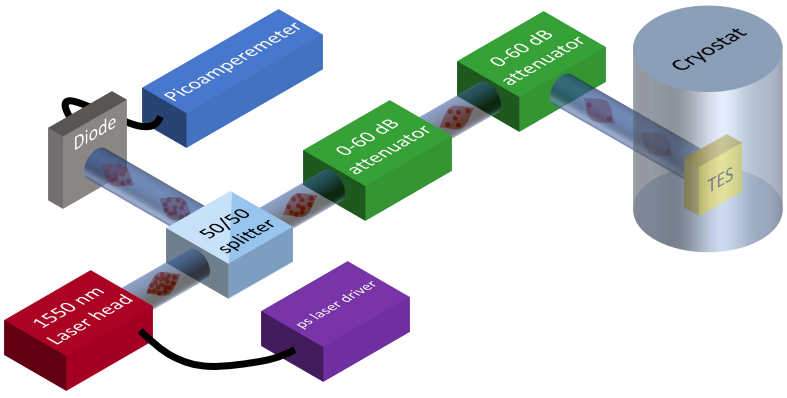

Fig. 5.27 Schematic of the setup for SDE measurement.

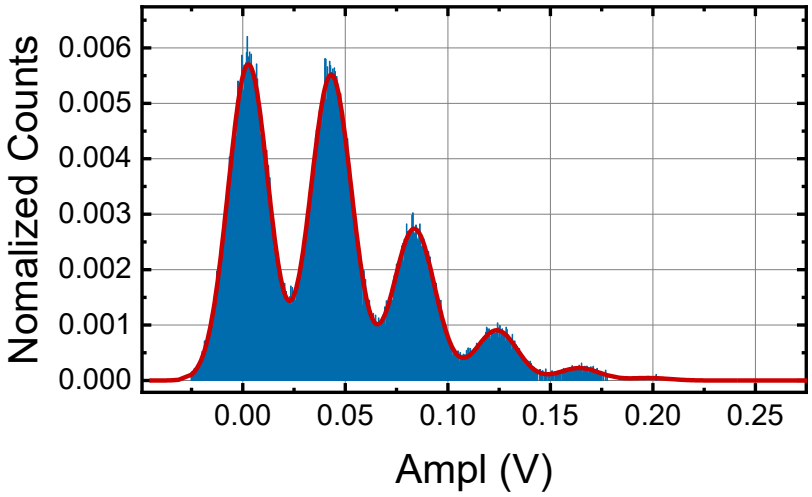

Fig. 5.28 Histogram of TES pulse amplitudes with the fitted Gaussian distribution. The measured mean photon number is $\mu_{\text{TES}} = 0.992 \pm 0.003$, the energy resolution at 0.8 eV is $\Delta E_{\text{fwhm}} \cong 0.46$ eV

diode, and the other is attenuated down to a few photons per pulse with two optical variable attenuator and sent to the cryostat.

Similar to the method described in Section 5.1.1, with the TES biased to its transition, we saved the waveform triggered by the laser while simultaneously reading the photocurrent generated by the diode. The histogram of the TES pulse amplitude shown in Figure 5.28 was taken with both attenuators in series set to 32 dB. The data were fitted with the following equation:

$$\text{Count}(V) = A\frac{e^{-\mu_{\text{TES}}}}{\sqrt{2\pi}}\sum_{i=0}^{5}\frac{\mu_{\text{TES}}^{i}}{i!}e^{\frac{-(V-x_i)^2}{2\sigma_i^2}} \tag{5.15}$$

From the fit (red curve in Figure 5.28), we obtained the mean photon number per pulse $\mu_{\text{TES}} = 0.992 \pm 0.003$.

We define the SDE as the ratio between μ_{TES} and the number of photons expected at the input of the cryostat μ_{in}:

$$SDE = \frac{\mu_{\text{TES}}}{\mu_{\text{in}}} \tag{5.16}$$

Where μ_{in} depends on Planck's constant (h) and the speed of light (c), the diode photocurrent (I_{ph}), the laser repetition rate (ν), the attenuation factor (Λ), the ratio between the monitored and attenuated paths (ρ), the laser emission wavelength (λ), and the diode sensitivity (S):

$$\mu_{\text{in}} = \frac{I_{\text{ph}} \cdot \rho \cdot \Lambda \cdot \lambda}{S \cdot \nu \cdot h \cdot c} \tag{5.17}$$

All these quantities were characterized before the measurement and their uncertainties evaluated. The diode was calibrated with by colleagues at PTB to a cryogenic radiometer at the PTB facility.

The formula for the SDE is therefore:

$$SDE = \frac{\mu_{\text{TES}} \cdot S \cdot \nu \cdot h \cdot c}{I_{\text{ph}} \cdot \rho \cdot \Lambda \cdot \lambda} \tag{5.18}$$

The combined uncertainty is:

$$u^2(SDE) = \left(\frac{\partial SDE}{\partial \mu_{\text{TES}}} u(\mu_{\text{TES}})\right)^2 + \left(\frac{\partial SDE}{\partial \nu} u(\nu)\right)^2 + \left(\frac{\partial SDE}{\partial S} u(S)\right)^2 + \left(\frac{\partial SDE}{\partial I_{\text{ph}}} u(I_{\text{ph}})\right)^2 + \left(\frac{\partial SDE}{\partial \rho} u(\rho)\right)^2 + \left(\frac{\partial SDE}{\partial \Lambda} u(\Lambda)\right)^2 + \left(\frac{\partial SDE}{\partial \lambda} u(\lambda)\right)^2$$

The sensitivity coefficients are:

$$\frac{\partial SDE}{\partial \mu_{\text{TES}}} = \frac{S \cdot \nu \cdot h \cdot c}{I_{\text{ph}} \cdot \rho \cdot \Lambda \cdot \lambda}, \quad \frac{\partial SDE}{\partial S} = \frac{\mu_{\text{TES}} \cdot \nu \cdot h \cdot c}{I_{\text{ph}} \cdot \rho \cdot \Lambda \cdot \lambda},$$
$$\frac{\partial SDE}{\partial \nu} = \frac{\mu_{\text{TES}} \cdot S \cdot h \cdot c}{I_{\text{ph}} \cdot \rho \cdot \Lambda \cdot \lambda}, \quad \frac{\partial SDE}{\partial I_{\text{ph}}} = -\frac{\mu_{\text{TES}} \cdot S \cdot \nu \cdot h \cdot c}{I_{\text{ph}}^2 \cdot \rho \cdot \Lambda \cdot \lambda},$$
$$\frac{\partial SDE}{\partial \rho} = -\frac{\mu_{\text{TES}} \cdot S \cdot \nu \cdot h \cdot c}{I_{\text{ph}} \cdot \rho^2 \cdot \Lambda \cdot \lambda}, \quad \frac{\partial SDE}{\partial \Lambda} = -\frac{\mu_{\text{TES}} \cdot S \cdot \nu \cdot h \cdot c}{I_{\text{ph}} \cdot \rho \cdot \Lambda^2 \cdot \lambda},$$
$$\frac{\partial SDE}{\partial \lambda} = -\frac{\mu_{\text{TES}} \cdot S \cdot \nu \cdot h \cdot c}{I_{\text{ph}} \cdot \rho \cdot \Lambda \cdot \lambda^2}.$$

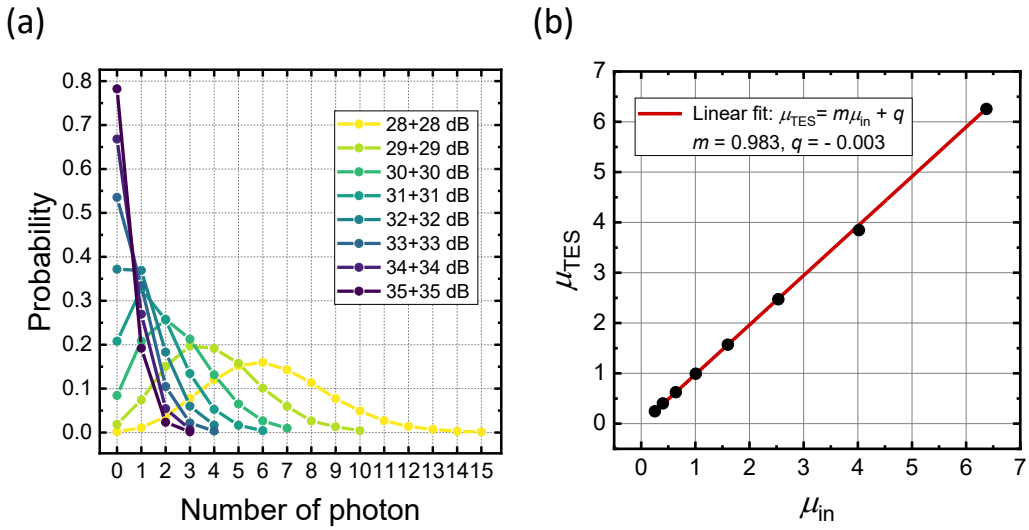

Fig. 5.29 Panel (a): Poissonian curves obtained for different attenuations. Panel (b): μ_{TES} vs. μ_{in} with a linear fit (red curve).

From the measurement shown in Figure 5.28 and the calibrated values, we evaluated an SDE of:

$$SDE = 0.98 \pm 0.02$$

with a confidence level of 95%. The uncertainty budget is shown in Table 5.2. From the budget, we can see that the major contribution to the uncertainty comes from the sensitivity measured during the calibration of the photodiode. We further studied the SDE at different mean photon numbers. In Figure 5.29, eight Poissonian curves are shown, each corresponding to different attenuation levels. These curves plot the probability related to the corresponding number of photons, derived from the histogram of TES amplitudes similar to that in Figure 5.28 (a).

For each dataset, we calculated both the mean photon number read by the TES (μ_{TES}) and the input photon number (μ_{in}) as described previously. Figure 5.29 (b) shows μ_{TES} plotted against μ_{in} with a linear fit (red curve). The slope of the fit represents the SDE over the range and was calculated to be $SDE_{\text{fit}} = 0.983 \pm 0.002$, with an intercept of $q = -0.0031 \pm 0.0006$. This result confirms that the SDE is constant over the 1-6 photon range.

5.4.1 Conclusion

The results from the system detection efficiency (SDE) measurements conducted at PTB Braunschweig demonstrate significant advancements in the operation of TES devices with high SDE, crucial for the SEQUME project. During the four-month period, we successfully set up a cryo-optical facility and achieved an SDE of 98% at a wavelength of 1548 nm using a 12 μm × 12 μm TiAu TES. The device, fabricated at AIST in Japan, showed excellent performance despite the challenging operational conditions.

The thorough characterization of the TES, including the fiber coupling and the cavity optimization for 1550 nm, ensured minimal losses and high efficiency along all the fiber optical connection between the input of the cryostat untill the TES. The methodology employed, involving the splitting of laser light into monitoring and attenuated paths, allowed for precise measurements and accurate calibration against a cryogenic radiometer.

The uncertainty budget analysis revealed that the major contribution to the uncertainty in SDE comes from the uncertainty of the sensitivity of the photodiode. Despite this, the combined standard uncertainty was maintained at an acceptable level, confirming the reliability of the SDE measurement.

Further studies on the SDE at different mean photon numbers reaffirmed the device's high efficiency and robustness. The linear relationship between μ_{TES} and μ_{in} demonstrated consistent performance across various attenuation levels.

Overall, the high SDE achieved with the TiAu TES device marks a significant milestone in the SEQUME project and represent a state of the art result for this kind of detector, paving the way for future advancements in high-efficiency photon detection systems. This progress not only supports the SEQUME project's goals, but also contributes to the broader field of quantum metrology and precision measurement.

Table 5.2 Uncertainty Budget for SDE Calculation

Source	**Value**	**Unit**	**Uncertainty Type**	**Std Uncertainty**	**Distribution**	**Sensitivity Coefficients**	**Uncertainty Contribution**
Diode Sensitivity (S)	1.12	A/W	B	0.01	Norm	0.88	0.0088
μ_{TES}	0.9910	-	A	0.0029	Norm	0.99	0.0029
Wavelength (λ)	1548×10^{-9}	m	B	2×10^{-9}	Rect	-6.36×10^{5}	−0.0013
Attenuation (Λ)	3.90127×10^{-7}	-	B	4.6×10^{-10}	Norm	-2.5×10^{6}	−0.0012
Ratio (ρ)	0.21778	-	B	0.00022	Norm	−4.52	−0.0010
Photocurrent (I_{ph})	1.70118×10^{-7}	A	A	1×10^{-10}	Norm	-5.7×10^{6}	−0.00058
		Combined Standard Uncertainty					0.0095
SDE	0.984	**Expanded Uncertainty** (95%)				k=1.96	0.019

5.5 Preliminary Results for Fast TES

In this section, I will discuss the preliminary results obtained in achieving TESs with short recovery times. As discussed in both Sections 2.3.5 and 3.5.2, two approaches can be followed: one consists of working at higher temperatures as shown by [113, 114, 22], and the other involves improving the conductance of the TES as demonstrated by [116].

5.5.1 Enhancing Recovery Time with Al TES

Typical working temperatures of TESs in the literature are shown in Table 2.2, where the highest critical temperature listed is 470 mK from [114] for a TES made by a single layer of Ti. In that case, the areas of the devices were 1 μm × 1 μm or 2 μm × 2 μm to compensate for the deterioration of the energy resolution due to high T_C.

Here, I present results for a TES with a much higher T_C made of aluminium. The reasons for using Al are twofold: first, the T_C of Ti-based TES is limited by the fact that titanium has bulk critical temperature of approximately 510 mK [141], while aluminium has a bulk critical temperature of 1.2 K. Second, Al has a lower heat capacity compared to Ti, which could compensate for the degradation of energy resolution due to higher T_C [1].

The preliminary results were obtained on a 7 μm × 7 μm TES made by a 30 nm layer of Al and wiring in Nb. As shown in Figure 5.30 (left), the superconductive transition of the TES was measured with a T_C of 1047 mK. Although the TES's energy resolution was not sufficient to discriminate single photons, a response was observed, as shown in Figure 5.30 (right). The figure also displays oscillations, indicating that the TES response is not stable.

As reported in [117], stability in TESs is achieved when $\frac{\tau_-}{\tau_+} > 5.8$. When the TES was polarized at 60% of its normal resistance, τ_+ was estimated to be approximately 8 ns. Therefore, τ_- could be less than 50 ns since the condition for stability is not met. Notably, the recovery time could be very short, but without improving the energy resolution and reducing the oscillation, this Al TES cannot be used for single-photon detection.

One important aspect to improve is the quality of the contact between the Al layer of the TES and the Nb wiring. During our investigations, we discovered that

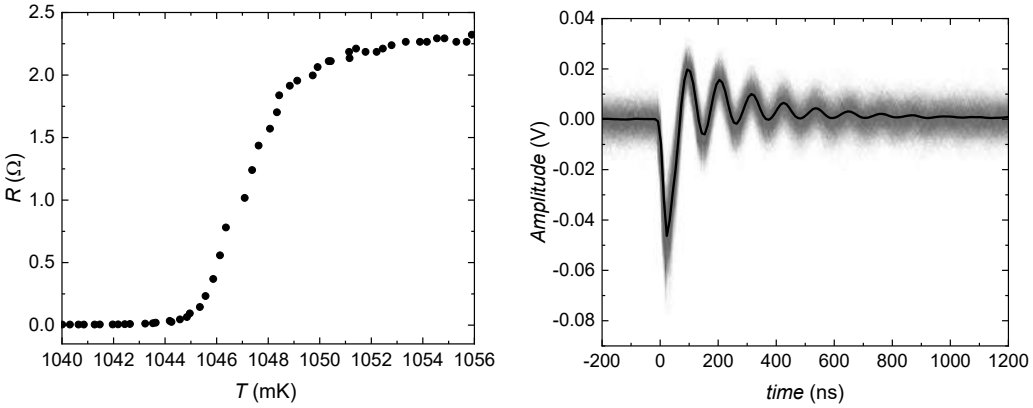

Fig. 5.30 Superconductive transition of a 7 µm × 7 µm Al TES (left). The superposition of 10,000 pulses is shown in gray, and the average is shown in black (right). This result was obtained by illuminating the TES with a pulsed monochromatic laser at constant power with emission at 1540 nm, and polarizing the TES at 60% of its normal resistance.

the performance of these devices was limited by the presence of a thin layer of aluminium oxide between the TES film and the wiring. This layer adversely affected the transition steepness and limited the critical current, resulting in poor energy resolution. This issue is currently under investigation. We are studying the optimal etching time before the deposition of the wiring, or alternatively, the possibility of depositing the wiring first and the aluminium afterward, ensuring good etching of Nb.

The preliminary results have provided valuable insights for the study of high T_C TES devices made with Al, indicating that improvements in stability and energy resolution are required but that potentially the recovery time could be very short.

5.5.2 Enhancing Recovery Time with Au Pads

In this section, I present preliminary results on the effect of Au pads on the performance of TES.

The Au pads refer to a layer of gold deposited after the deposition of the TES and before the deposition of the wiring. These pads are positioned on the sides of the TES that will not be covered by the wiring. A schematic of the layout is shown in Figure 5.31.

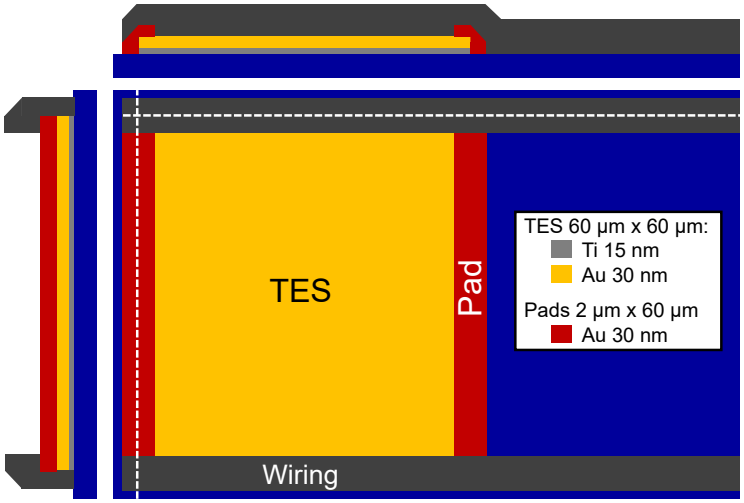

Fig. 5.31 Schematic layout of TES with Au pads. The horizontal dashed line is the reference for the section on top, and the vertical dashed line is for the section on the left.

The results presented here are obtained with two 60 µm × 60µm TES made of 15 nm of titanium and 30 nm of gold. Each pad consists of a 2 µm × 60µm layer of 30 nm Au deposited on two opposite sides of the TES, with 1 µm overlapping the TES and the other 1 µm directly on the substrate. On the two sides without pads, the wiring is deposited. Even though this pad contributes to the total heat capacity of the TES, the contribution is negligible. The volume of the gold pads relative to the total volume of gold in the TES is less than 4%.

The goal of adding Au pads is twofold. The first objective is related to an ongoing study on the aging of the TES. We are investigating the positive effect that these pads could have on the degradation of TiAu TES. By covering the sides not covered by the wiring, we aim to prevent the oxidation of the titanium due to the lateral surfaces exposed to air. This study is a long-term investigation and will not be discussed further here. The second objective is to enhance the thermal conductance and thereby improve the recovery time of the TES, as demonstrated by [116].

The first TES, labeled "p1," has a T_C of 123 mK. We measure the power dissipated to the substrate as described in Section 5.1, from which we calculate a conductance $G^{p1} = 654 \pm 5$ pW/K. The measured data and with the fit are shown in Figure 5.32 We characterized the device optically with a 406 nm pulsed laser using a 9 µm core fiber glued on the TES as described in Section 4.3. The response of the TES and

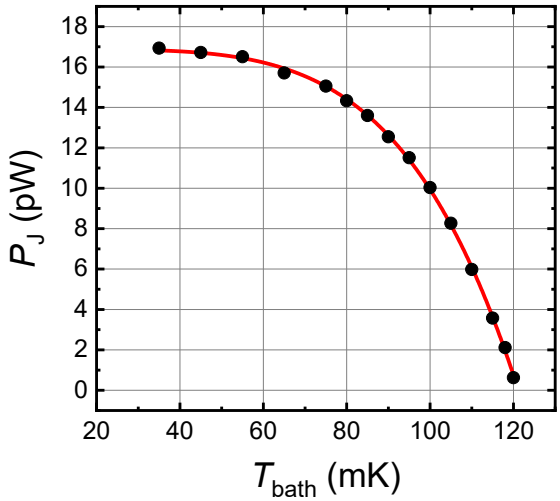

Fig. 5.32 Joule power dissipated to the substrate at different bath temperature when the TES p1 is polarize on the transition (back dots). The red line represents the fit of Eq. 5.1

its PNR is shown in Figure 5.33. Panel (a) shows 200 waveforms taken with the laser repetition rate at 50 kHz. From the average of the waveforms of the one-photon pulses, we extract the rise and fall time constants by fitting Equation 5.11:

$$\tau_{+}^{p1} = 81 \text{ ns}$$

$$\tau_{-}^{p1} = 244 \text{ ns}$$

The recovery time of the device, therefore, is $5 \cdot \tau_{-}^{p1} \sim 1.25\mu$s. This implies an MDR of approximately 800 kHz. We investigated the MDR by increasing the laser repetition rate and measuring both the energy resolution and the mean photon number. For repetition rates below 800 kHz, we expect the TES to maintain its performance independent of the laser repetition rate. In contrast, at laser repetition rates higher than the MDR, we anticipated a deterioration in energy resolution. An example of TES response to a repetition rate higher than 800 kHz is shown in Figure 5.33 (b), where the laser rate was set at 1.5 MHz. From the figure, it is visible that the TES does not fully recover between one pulse and another and signals are piling-up, even if the PNR capability is still clearly recognisable. This has an effect on the variability of the pulse amplitude, which has an effect on the energy resolution.

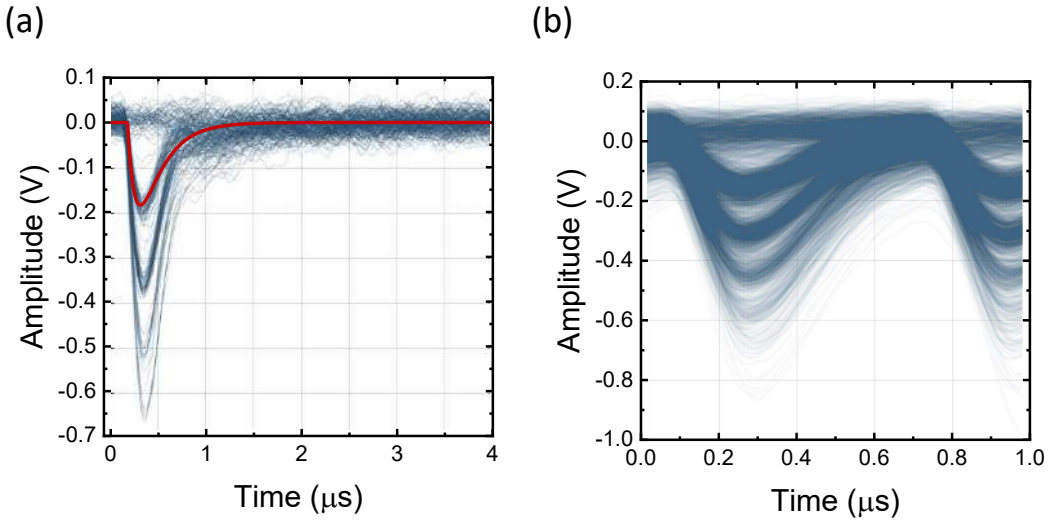

Fig. 5.33 TES p1 response to 406 nm photons at different laser rates. Panel (a): 200 waveform overlay and the fit function in red, laser rate at 50 kHz. Panel (b): TES response with laser repetition rate at 1.5 MHz, 50,000 waveforms overlaid. Pile up of waveforms is visible.

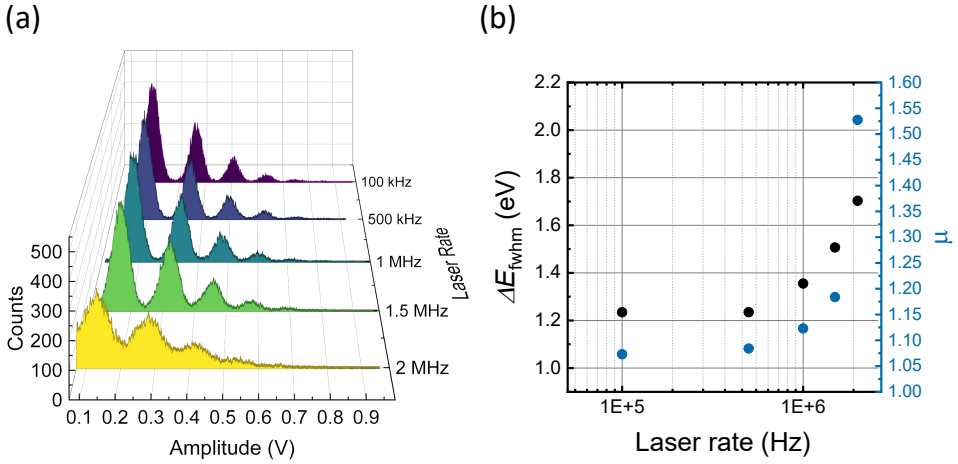

Fig. 5.34 Panel (a): Histograms of the TES response at different laser repetition rates. When the rate is below 800 kHz, the peaks are well separated, while at higher rates up to 2 MHz, the peaks become broader, indicating a deterioration in energy resolution. Panel (b): The plot shows the energy resolution at 3.05 eV (left axis) and the mean photon number (blue dots on the right axis) as a function of laser repetition rate. After 1 MHz, the energy resolution significantly deteriorates, and the mean photon number increases, suggesting that the TES does not fully recover between pulses at higher repetition rates.

The experimental results on the photon counting at different repetitions rate confirm this analysis and are reported in Figure 5.34, are consistent with this. In panel (a), five histograms at different laser repetition rates are displayed. When the rate is below 800 kHz, the peaks are well separated, while by increasing the rate up to 2 MHz, the peaks become broader. This is reflected in the plot in panel (b); the energy resolution at 3.05 eV, reported on the left axis, significantly deteriorates for frequencies higher than 1 MHz. Additionally, we observe that the mean photon number of the Poissonian statistics (blue dots on the right axis) increases from 1 MHz and beyond. This could be due to the fact that since the TES does not fully recover before a new detection occurs, there is an offset and the amplitude of the signals due to a new pulse is influenced by this. More investigations should be done to see if the MDR could be extended to a higher value than $\frac{1}{5\tau_{-}^{\mathrm{p1}}}$, since we noticed that even if the energy resolution deteriorates, it is still possible to discriminate single photons up to 2 MHz. We should understand why the measured mean photon number increases and if with a correct analysis that takes into account the piling up of the pulses, it is possible to operate the TES at this higher repetition rate while being confident that we are measuring the correct mean photon number.

The second TES described here, labeled "p2," has an almost identical critical temperature ($T_{\mathrm{C}} = 121$ mK) to p1, but with only one Au pad, meaning that the total volume of Au is halved and so we expected a lower thermal conductance. From the measurement, we calculate a $G^{\mathrm{p2}} = 413 \pm 5$ pW/K, which is 37% smaller than G^{p1}. The measured data and with the fit are shown in Figure 5.32

In this case, we measured a time constant of:

$$\tau_{+}^{\mathrm{p2}} = 422 \text{ ns}$$

$$\tau_{-}^{\mathrm{p2}} = 425 \text{ ns}$$

Therefore, we expect to be limited to an MDR of ~ 470 kHz. An example of the TES response to the 406 nm laser with a repetition rate set to 500 kHz is shown in Figure 5.36. From the image, we see that the device is still capable of PNR resolution. This result, together with the ones of TES p1, are a good indication that by adding these Au pads we are influencing the thermal conductance of the TiAu TES and so improving their recovery time. Further investigation is needed to optimize the

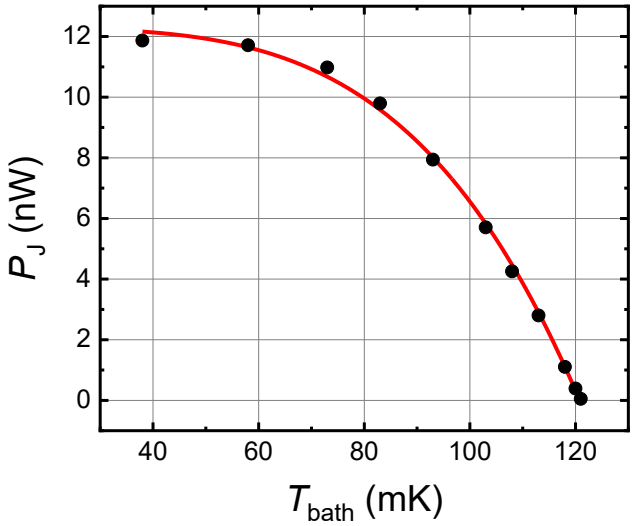

Fig. 5.35 Joule power dissipated to the substrate at different bath temperature when the TES p2 is polarized on the transition (back dots). The red line represents the fit of Eq. 5.1

volume of Au and extend this application to smaller TES in order to improve the energy resolution and discriminate photons in the IR.

Saturation Energy

Another important feature of such devices with this large active area is linked to their saturation energy. Figure 5.37 shows an histogram of pulse amplitudes acquired while increasing the incoming light intensity to TES p2. The histogram shows that with the 406 nm laser we are capable of discriminating up to 25 photons per pulse, meaning a saturation energy of the order of ~ 75 eV. This high saturation energy together with the possibility of operating the TES at a high repetition rate could be of great interest for radiometry applications.If we consider a TES illuminated with a repetition rate of 500 kHz receiving an average of 30 eV per pulse, the order of magnitude of the optical power at the input of the TES is 2 pW. This is within the range that standard detectors for radiometry are capable of measuring today [164]. A TES with an area suitable for a multimode fiber, typically with a core of 50 µm and an improved SDE in the optical range, could be used to bridge the gap between single-photon detectors and standard radiometry by performing a direct comparison.

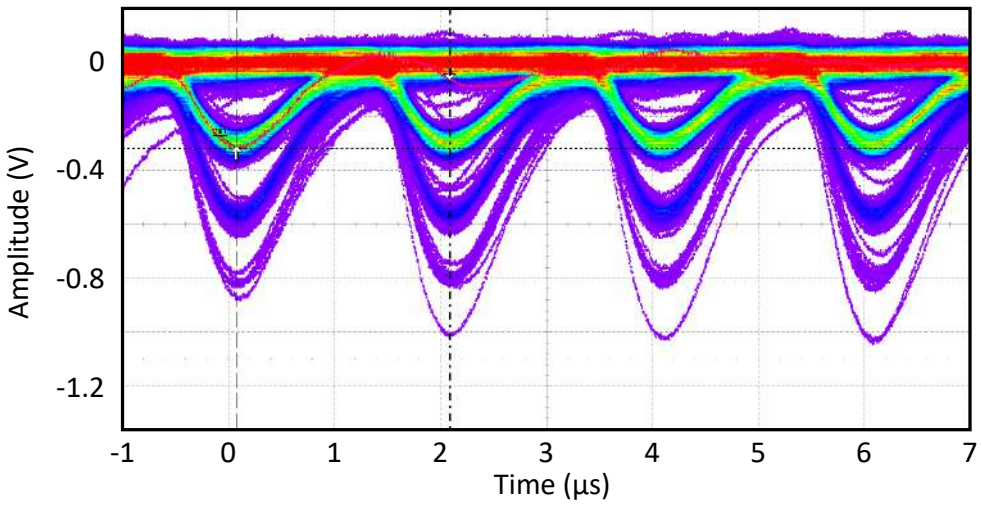

Fig. 5.36 TES p2 response to 406 nm laser at a repetition rate of 500 kHz. The pulses are separated by 2 µs, with the 3/4 photon pulses starting to overlap with the next detection event, demonstrating the device's PNR capability.

This is an active area of research in radiometry and will be part of the EMPIR project ScaleUP [165].

5.5.3 Conclusion

The preliminary results discussed in this section indicate significant potential for achieving TES devices with short recovery times by utilizing both higher critical temperature materials and/or enhanced thermal conductance. Specifically, the use of aluminium for TES film and gold pads has shown promising outcomes.

For the Al TES, the higher critical temperature ($T_C = 1047$ mK) achieved with a 30 nm layer of Al has demonstrated a potential for very short recovery times. However, challenges remain in improving energy resolution and ensuring stability, as indicated by the observed oscillations. The presence of an aluminium oxide layer between the TES film and the Nb wiring has been identified as a limiting factor. Ongoing investigations aim to optimize the etching process or adjust the deposition sequence to enhance the contact quality, thereby improving device performance.

The addition of Au pads to the TES made of Ti and Au layers has also been explored. The Au pads aim to prevent the oxidation of titanium and enhance thermal

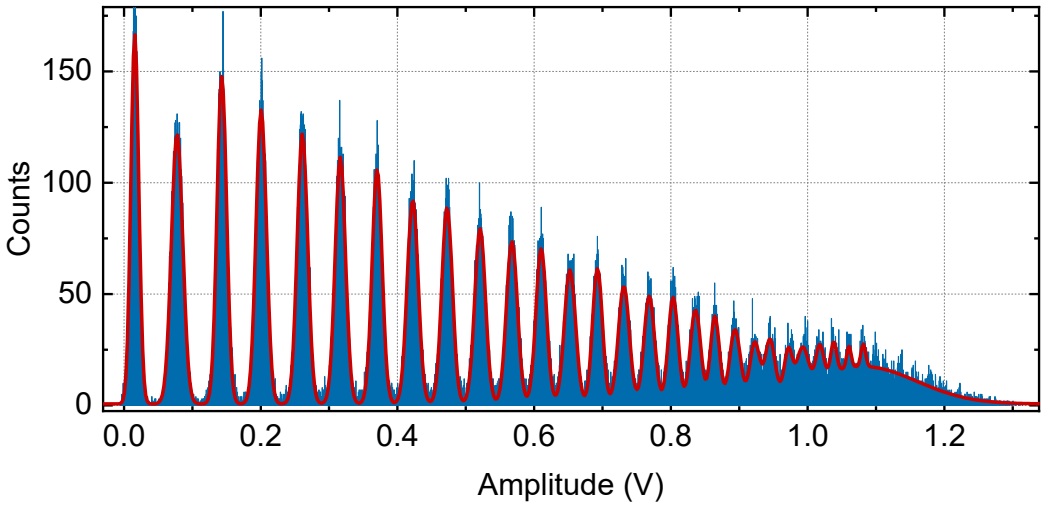

Fig. 5.37 Histogram of pulse amplitudes acquired while increasing the incoming light intensity to TES p2. The histogram shows discrimination of up to 20 photons per pulse, corresponding to an energy of $\sim$ 60 eV, demonstrating the high saturation energy of the device.

conductance. The TES labeled "p1" showed improved thermal conductance and a high MDR of approximately 800 kHz. The second TES, labeled "p2", with a single Au pad, demonstrated a lower thermal conductance and an MDR of around 470 kHz. This comparison indicates that the volume of Au directly influences the thermal conductance and recovery time.

Further research is necessary to optimize the Au pad volume and extend these enhancements to smaller TES devices, which could improve energy resolution and photon discrimination in the infrared range. Additionally, the high saturation energy observed in these fast TESs, capable of discriminating up to 25 photons per pulse, highlights the potential for radiometric application. A TES with an area suitable for multimode fiber could bridge the gap between single-photon detectors and standard radiometry, offering valuable insights for future developments.

In conclusion, while significant progress has been made, further improvements in stability, energy resolution, and device optimization are required to fully realize the potential of fast TES devices for various applications.

Chapter 6

Conclusion

In this thesis, I have focused on the development and enhancement of Transition-Edge Sensors (TESs) for high-precision applications, particularly in neutrino physics, dark matter research, quantum metrology, and radiometry. My research primarily aimed to improve TES performance in the optical to near-infrared energy range.

One of the primary objectives of my research was to achieve excellent energy resolution with TES devices without reducing the detector area, indeed keeping it as large as possible to meet the stringent requirements of the PTOLEMY project. The results with the Lito20 and Lito50 samples are promising. The Lito20 TES, with an area of 20 μm × 20 μm, achieved an energy resolution of 0.114 ± 0.001 eV at 0.8 eV, meeting the PTOLEMY project's performance requirements. Similarly, the Lito50 TES achieved 0.158 ± 0.001 eV at 0.8 eV. These advancements mark a substantial step forward in developing high-resolution detectors for precise energy measurements of low-energy particles. Future work should focus on developing TES devices with low T_C similar to the Lito50 TES but with improved stability over time. Additionally, the next critical step would be to realize an array of TES capable of high energy resolution.

Another crucial objective driven by the PTOLEMY project was to demonstrate that TES devices could detect low-energy electrons with energy resolutions comparable to those for photons. Using a cold electron source based on field emission from vertically-aligned carbon nanotubes, we demonstrated for the first time the possibility to detect low energy electrons with an intrinsic energy resolution between 1.8 and 4 eV for fully-absorbed electrons in the $90 - 101$ eV range. This resolution

is similar to that achieved for photons in the same energy range, demonstrating that TES devices can effectively detect both types of particles with high precision. This direct comparison between photon and electron energy resolutions opens new possibilities in electron detection, representing a significant milestone in the field. The next step in this direction is to investigate the TES response at even lower electron energies, around 10 eV. This would involve working on the electron source to achieve controlled field emission at lower voltages. Moreover, it will be important to study the detection efficiency of TES with electrons to fully understand and optimize their performance in electron detection.

The third objective of my research was to investigate the dark count rate (DCR) of TES detectors for their potential use in the dark matter search experiment QHaloS. In the thesis, I presented the characterization of the dark count of a TiAu TES, for which we measured a DCR of 3.6×10^{-4} Hz within the energy range of 0.8 eV to 3.2 eV. Moreover, through experimental runs involving radioactive sources, cosmic ray coincidence setups, and GEANT4 simulations, we proved that cosmic rays and environmental gamma rays are the primary contributors to high-energy DCR. We also assessed that the rate of photon-like events is not correlated with the rate of high-energy events. Further studies are needed to understand the origin of photon-like events in completely shielded TES devices. The next step involves investigating how to integrate TES detectors into the QHaloS experiment while achieving high system detection efficiency.

In the SEQUME project, I made significant contributions to achieving a system detection efficiency (SDE) of 98% at 1550 nm using a 12 µm $\times$ 12 µm TiAu TES fabricated by AIST(Japan). This high efficiency was verified through characterization and calibration, demonstrating the robustness and reliability of the TES device. These results support the SEQUME project's goals and contribute significantly to the broader field of quantum metrology.

Preliminary results for faster TES recovery times are also promising. By using higher critical temperature materials, such as aluminium, and enhancing thermal conductance with gold pads, I was able to achieve shorter recovery times. The next challenges involve improving energy resolution and ensuring stability for Al TES, as well as further studying how to optimize the Au pads for faster TiAu TES.

References

[1] Kent D Irwin and Gene C Hilton. Transition-edge sensors. In *Cryogenic particle detection*, pages 63–150. Springer, 2005.

[2] JM Gildemeister, Adrian T Lee, and PL Richards. A fully lithographed voltage-biased superconducting spiderweb bolometer. *Applied Physics Letters*, 74(6):868–870, 1999.

[3] KD Irwin. An application of electrothermal feedback for high resolution cryogenic particle detection. *Applied Physics Letters*, 66(15):1998–2000, 1995.

[4] B Cabrera, RM Clarke, P Colling, AJ Miller, S Nam, and RW Romani. Detection of single infrared, optical, and ultraviolet photons using superconducting transition edge sensors. *Applied Physics Letters*, 73(6):735–737, 1998.

[5] Daniel T Chow, Alex Loshak, Marcel L van den Berg, Matthias A Frank, Troy W Barbee Jr, and Simon E Labov. High-resolution gamma-ray spectrometers using bulk absorbers coupled to mo/cu multilayer superconducting transition-edge sensors. In *Hard X-Ray, Gamma-Ray, and Neutron Detector Physics II*, volume 4141, pages 67–75. SPIE, 2000.

[6] Dmitry V Morozov, Alessandro Casaburi, and Robert H Hadfield. Superconducting photon detectors. *Contemporary Physics*, 62(2):69–91, 2021.

[7] Adriana E Lita, Dileep V Reddy, Varun B Verma, Richard P Mirin, and Sae Woo Nam. Development of superconducting single-photon and photon-number resolving detectors for quantum applications. *Journal of Lightwave Technology*, 40(23):7578–7597, 2022.

[8] Robert H Hadfield. Single-photon detectors for optical quantum information applications. *Nature photonics*, 3(12):696–705, 2009.

[9] Francesco Ceccarelli, Giulia Acconcia, Angelo Gulinatti, Massimo Ghioni, Ivan Rech, and Roberto Osellame. Recent advances and future perspectives of single-photon avalanche diodes for quantum photonics applications. *Advanced Quantum Technologies*, 4(2):2000102, 2021.

[10] Didier DE Martin and Peter Verhoeve. Superconducting tunnel junctions. In *Observing Photons in Space: A Guide to Experimental Space Astronomy*, pages 479–496. Springer, 2013.

[11] Jochem Baselmans. Kinetic inductance detectors. *Journal of Low Temperature Physics*, 167:292–304, 2012.

[12] Chandra M Natarajan, Michael G Tanner, and Robert H Hadfield. Superconducting nanowire single-photon detectors: physics and applications. *Superconductor science and technology*, 25(6):063001, 2012.

[13] Adriana E Lita, Aaron J Miller, and Sae Woo Nam. Counting near-infrared single-photons with 95% efficiency. *Optics express*, 16(5):3032–3040, 2008.

[14] Daiji Fukuda, Go Fujii, Takayuki Numata, Kuniaki Amemiya, Akio Yoshizawa, Hidemi Tsuchida, Hidetoshi Fujino, Hiroyuki Ishii, Taro Itatani, Shuichiro Inoue, et al. Titanium-based transition-edge photon number resolving detector with 98% detection efficiency with index-matched small-gap fiber coupling. *Optics express*, 19(2):870–875, 2011.

[15] Jan Dreyling-Eschweiler, Noemie Bastidon, Babette Döbrich, Dieter Horns, Friederike Januschek, and Axel Lindner. Characterization, 1064 nm photon signals and background events of a tungsten tes detector for the alps experiment. *Journal of Modern Optics*, 62(14):1132–1140, 2015.

[16] Laura Manenti, Carlo Pepe, Isaac Sarnoff, Tengiz Ibrayev, Panagiotis Oikonomou, Artem Knyazev, Eugenio Monticone, Hobey Garrone, Fiona Alder, Osama Fawwaz, et al. Study of dark counts in optical superconducting transition-edge sensors. *arXiv preprint arXiv:2402.03073*, 2024.

[17] Kaori Hattori, Toshio Konno, Yoshitaka Miura, Sachiko Takasu, and Daiji Fukuda. An optical transition-edge sensor with high energy resolution. *Superconductor Science and Technology*, 35(9):095002, 2022.

[18] L Lolli, Emanuele Taralli, Chiara Portesi, Eugenio Monticone, and Mauro Rajteri. High intrinsic energy resolution photon number resolving detectors. *Applied Physics Letters*, 103(4):041107, 2013.

[19] Xiaolong Xu, Xiaoying Sun, Jian Chen, Mauro Rajteri, Hobey Garrone, Carlo Pepe, Wan Li, Jinjin Li, Mingyu Zhang, Tianjia Bu, et al. Development of ti/au transition-edge sensors for single-photon detection. *IEEE Transactions on Applied Superconductivity*, 2024.

[20] M Tarkhov, J Claudon, J Ph Poizat, A Korneev, A Divochiy, O Minaeva, V Seleznev, N Kaurova, B Voronov, AV Semenov, et al. Ultrafast reset time of superconducting single photon detectors. *Applied Physics Letters*, 92(24), 2008.

[21] Boris Korzh, Qing-Yuan Zhao, Jason P Allmaras, Simone Frasca, Travis M Autry, Eric A Bersin, Andrew D Beyer, Ryan M Briggs, Bruce Bumble, Marco Colangelo, et al. Demonstration of sub-3 ps temporal resolution with a superconducting nanowire single-photon detector. *Nature Photonics*, 14(4):250–255, 2020.

[22] Ryo Kobayashi, Kaori Hattori, Shuichiro Inoue, and Daiji Fukuda. Development of a fast response titanium-gold bilayer optical tes with an optical fiber self-alignment structure. *IEEE Transactions on Applied Superconductivity*, 29(5):1–5, 2019.

[23] Antia Lamas-Linares, Brice Calkins, Nathan A Tomlin, Thomas Gerrits, Adriana E Lita, Jörn Beyer, Richard P Mirin, and Sae Woo Nam. Nanosecond-scale timing jitter for single photon detection in transition edge sensors. *Applied Physics Letters*, 102(23), 2013.

[24] Ptolemy website https://ptolemy.lngs.infn.it/.

[25] E Baracchini, MG Betti, M Biasotti, A Bosca, F Calle, J Carabe-Lopez, G Cavoto, C Chang, AG Cocco, AP Colijn, et al. Ptolemy: A proposal for thermal relic detection of massive neutrinos and directional detection of mev dark matter. *arXiv preprint arXiv:1808.01892*, 2018.

[26] MG Betti, M Biasotti, A Boscá, F Calle, N Canci, G Cavoto, C Chang, AG Cocco, AP Colijn, et al. Neutrino physics with the ptolemy project: active neutrino properties and the light sterile case. *Journal of Cosmology and Astroparticle Physics*, 2019(07):047, 2019.

[27] N Rossi, A Apponi, MG Betti, M Borghesi, O Castellano, G Cavoto, E Celasco, W Chung, A Cocco, A Colijn, et al. Cosmic neutrino background detection with ptolemy. In *The European Physical Society Conference on High Energy Physics*, page 103, 2024.

[28] M Rajteri, M Biasotti, M Faverzani, E Ferri, R Filippo, F Gatti, A Giachero, E Monticone, A Nucciotti, and A Puiu. Tes microcalorimeters for ptolemy. *Journal of Low Temperature Physics*, 199:138–142, 2020.

[29] A Apponi, MG Betti, M Borghesi, N Canci, G Cavoto, C Chang, W Chung, AG Cocco, AP Colijn, N D'Ambrosio, et al. Implementation and optimization of the ptolemy transverse drift electromagnetic filter. *Journal of Instrumentation*, 17(05):P05021, 2022.

[30] Masha Baryakhtar, Junwu Huang, and Robert Lasenby. Axion and hidden photon dark matter detection with multilayer optical haloscopes. *Physical Review D*, 98(3):035006, 2018.

[31] Nabila Aghanim, Yashar Akrami, Mark Ashdown, Jonathan Aumont, Carlo Baccigalupi, Mario Ballardini, Anthony J Banday, RB Barreiro, N Bartolo, S Basak, et al. Planck 2018 results-vi. cosmological parameters. *Astronomy & Astrophysics*, 641:A6, 2020.

[32] Marco Fabbrichesi, Emidio Gabrielli, and Gaia Lanfranchi. *The Physics of the Dark Photon: A Primer*. Springer, 2021.

[33] Laura Manenti, Umang Mishra, Gianmarco Bruno, Henry Roberts, Panos Oikonomou, Renu Pasricha, Isaac Sarnoff, James Weston, Francesco Arneodo, Adriano Di Giovanni, et al. Search for dark photons using a multilayer dielectric haloscope equipped with a single-photon avalanche diode. *Physical Review D*, 105(5):052010, 2022.

[34] Jeff Chiles, Ilya Charaev, Robert Lasenby, Masha Baryakhtar, Junwu Huang, Alexana Roshko, George Burton, Marco Colangelo, Ken Van Tilburg, Asimina Arvanitaki, et al. New constraints on dark photon dark matter with superconducting nanowire detectors in an optical haloscope. *Physical Review Letters*, 128(23):231802, 2022.

[35] Sequme website: https://sequme.cmi.cz/, 2024. Accessed: 2024-06-19.

[36] Stefan Kück, Marco López, Helmuth Hofer, Hristina Georgieva, Justus Christinck, Beatrice Rodiek, Geiland Porrovecchio, Marek Šmid, Stephan Götzinger, Christoph Becher, et al. Single photon sources for quantum radiometry: a brief review about the current state-of-the-art. *Applied Physics B*, 128(2):28, 2022.

[37] Emilio Corte, Selene Sachero, Sviatoslav Ditalia Tchernij, Tobias Lühmann, Sébastien Pezzagna, Paolo Traina, Ivo Pietro Degiovanni, Ekaterina Moreva, Paolo Olivero, Jan Meijer, et al. Spectral emission dependence of tin-vacancy centers in diamond from thermal processing and chemical functionalization. *Advanced Photonics Research*, 3(1):2100148, 2022.

[38] Cornelius Nawrath, Raphael Joos, Sascha Kolatschek, Stephanie Bauer, Pascal Pruy, Florian Hornung, Julius Fischer, Jiasheng Huang, Ponraj Vijayan, Robert Sittig, et al. Bright source of purcell-enhanced, triggered, single photons in the telecom c-band. *Advanced Quantum Technologies*, 6(11):2300111, 2023.

[39] Ghulam Murtaza, Maja Colautti, Michael Hilke, Pietro Lombardi, Francesco Saverio Cataliotti, Alessandro Zavatta, Davide Bacco, and Costanza Toninelli. Efficient room-temperature molecular single-photon sources for quantum key distribution. *Optics Express*, 31(6):9437–9447, 2023.

[40] Joshua Bienfang, Thomas Gerrits, Paulina Kuo, Alan Migdall, Sergey Polyakov, and Oliver Slattery. Single-photon sources and detectors dictionary, 2023.

[41] Jeremy L O'brien. Optical quantum computing. *Science*, 318(5856):1567–1570, 2007.

[42] Giorgio Brida, Marco Genovese, and Marco Gramegna. Twin-photon techniques for photo-detector calibration. *Laser Physics Letters*, 3(3):115, 2005.

[43] K Nagayoshi, ML Ridder, MP Bruijn, L Gottardi, E Taralli, P Khosropanah, H Akamatsu, S Visser, and J-R Gao. Development of a ti/au tes microcalorimeter array as a backup sensor for the athena/x-ifu instrument. *Journal of Low Temperature Physics*, 199:943–948, 2020.

[44] Antonio Pifferi, Alessandro Torricelli, Lorenzo Spinelli, Davide Contini, Rinaldo Cubeddu, Fabrizio Martelli, Giovanni Zaccanti, Alberto Tosi, Alberto Dalla Mora, Franco Zappa, et al. Time-resolved diffuse reflectance using small source-detector separation and fast single-photon gating. *Physical review letters*, 100(13):138101, 2008.

[45] Marissa Giustina, Marijn AM Versteegh, Sören Wengerowsky, Johannes Handsteiner, Armin Hochrainer, Kevin Phelan, Fabian Steinlechner, Johannes Kofler, Jan-Åke Larsson, Carlos Abellán, et al. Significant-loophole-free test of bell's theorem with entangled photons. *Physical review letters*, 115(25):250401, 2015.

[46] Dileep V Reddy, Robert R Nerem, Sae Woo Nam, Richard P Mirin, and Varun B Verma. Superconducting nanowire single-photon detectors with 98% system detection efficiency at 1550 nm. *Optica*, 7(12):1649–1653, 2020.

[47] Peng Hu, Hao Li, Lixing You, Heqing Wang, You Xiao, Jia Huang, Xiaoyan Yang, Weijun Zhang, Zhen Wang, and Xiaoming Xie. Detecting single infrared photons toward optimal system detection efficiency. *Optics Express*, 28(24):36884–36891, 2020.

[48] J Chang, JWN Los, JO Tenorio-Pearl, Niels Noordzij, R Gourgues, A Guardiani, JR Zichi, SF Pereira, HP Urbach, Val Zwiller, et al. Detecting telecom single photons with 99.5- 2.07+ 0.5% system detection efficiency and high time resolution. *APL Photonics*, 6(3), 2021.

[49] H Kamerlingh Onnes. The superconductivity of mercury. *Comm. Phys. Lab. Univ. Leiden*, 122:124, 1911.

[50] Walther Meissner and Robert Ochsenfeld. Ein neuer effekt bei eintritt der supraleitfähigkeit. *Naturwissenschaften*, 21(44):787–788, 1933.

[51] F London. On the problem of the molecular theory of superconductivity. *Physical Review*, 74(5):562, 1948.

[52] Lev Davidovich Landau and Vitaly Lazarevich Ginzburg. On the theory of superconductivity. *Zh. Eksp. Teor. Fiz.*, 20:1064, 1950.

[53] Fritz London and Heinz London. The electromagnetic equations of the supraconductor. *Proceedings of the Royal Society of London. Series A-Mathematical and Physical Sciences*, 149(866):71–88, 1935.

[54] John Bardeen, Leon N Cooper, and J Robert Schrieffer. Microscopic theory of superconductivity. *Physical Review*, 106(1):162, 1957.

[55] John Bardeen, Leon N Cooper, and John Robert Schrieffer. Theory of superconductivity. *Physical review*, 108(5):1175, 1957.

[56] Brian G Marchionini, Yutaka Yamada, Luciano Martini, and Hiroyuki Ohsaki. High-temperature superconductivity: a roadmap for electric power sector applications, 2015–2030. *IEEE Transactions on Applied Superconductivity*, 27(4):1–7, 2017.

[57] John H Durrell, Mark D Ainslie, Difan Zhou, Philippe Vanderbemden, Tom Bradshaw, Susannah Speller, Mykhaylo Filipenko, and David A Cardwell. Bulk superconductors: a roadmap to applications. *Superconductor science and technology*, 31(10):103501, 2018.

[58] Alexander Molodyk and David C Larbalestier. The prospects of high-temperature superconductors. *Science*, 380(6651):1220–1222, 2023.

[59] Brian David Josephson. Possible new effects in superconductive tunnelling. *Physics letters*, 1(7):251–253, 1962.

[60] Philip W Anderson and John M Rowell. Probable observation of the josephson superconducting tunneling effect. *Physical Review Letters*, 10(6):230, 1963.

[61] A Peacock, P Verhoeve, N Rando, A Van Dordrecht, BG Taylor, C Erd, MAC Perryman, R Venn, J Howlett, DJ Goldie, et al. Single optical photon detection with a superconducting tunnel junction. *Nature*, 381(6578):135–137, 1996.

[62] GN Gol'Tsman, O Okunev, G Chulkova, A Lipatov, A Semenov, K Smirnov, B Voronov, A Dzardanov, C Williams, and Roman Sobolewski. Picosecond superconducting single-photon optical detector. *Applied physics letters*, 79(6):705–707, 2001.

[63] Peter K Day, Henry G LeDuc, Benjamin A Mazin, Anastasios Vayonakis, and Jonas Zmuidzinas. A broadband superconducting detector suitable for use in large arrays. *Nature*, 425(6960):817–821, 2003.

[64] Alexei D Semenov, Gregory N Gol'tsman, and Roman Sobolewski. Hot-electron effect in superconductors and its applications for radiation sensors. *Superconductor Science and Technology*, 15(4):R1, 2002.

[65] Allen Rothwarf and BN Taylor. Measurement of recombination lifetimes in superconductors. *Physical Review Letters*, 19(1):27, 1967.

[66] AG Kozorezov, AF Volkov, JK Wigmore, A Peacock, A Poelaert, and R Den Hartog. Quasiparticle-phonon downconversion in nonequilibrium superconductors. *Physical Review B*, 61(17):11807, 2000.

[67] A Zehnder. Response of superconductive films to localized energy deposition. *Physical Review B*, 52(17):12858, 1995.

[68] Damian Twerenbold. Superconducting tunnelling junctions as high-resolution x-ray detectors, 1986.

[69] DDE Martin, P Verhoeve, T Oosterbroek, R Hijmering, A Peacock, and R Schulz. Accurate time-resolved optical photospectroscopy with superconducting tunnel junction arrays. In *Ground-based and Airborne Instrumentation for Astronomy*, volume 6269, pages 238–248. SPIE, 2006.

[70] Evan D Walsh, Woochan Jung, Gil-Ho Lee, Dmitri K Efetov, Bae-Ian Wu, K-F Huang, Thomas A Ohki, Takashi Taniguchi, Kenji Watanabe, Philip Kim, et al. Josephson junction infrared single-photon detector. *Science*, 372(6540):409–412, 2021.

[71] EGP O'Connor, A Shearer, and K O'Brien. Energy-sensitive detectors for astronomy: Past, present and future. *New Astronomy Reviews*, 87:101526, 2019.

[72] Omar S Magaña-Loaiza, Roberto de J León-Montiel, Armando Perez-Leija, Alfred B U'Ren, Chenglong You, Kurt Busch, Adriana E Lita, Sae Woo Nam, Richard P Mirin, and Thomas Gerrits. Multiphoton quantum-state engineering using conditional measurements. *npj Quantum Information*, 5(1):80, 2019.

[73] Martin Von Helversen, Jonas Böhm, Marco Schmidt, Manuel Gschrey, Jan-Hindrik Schulze, André Strittmatter, Sven Rodt, Jörn Beyer, Tobias Heindel, and Stephan Reitzenstein. Quantum metrology of solid-state single-photon sources using photon-number-resolving detectors. *New Journal of Physics*, 21(3):035007, 2019.

[74] Mamoru Endo, Ruofan He, Tatsuki Sonoyama, Kazuma Takahashi, Takahiro Kashiwazaki, Takeshi Umeki, Sachiko Takasu, Kaori Hattori, Daiji Fukuda, Kosuke Fukui, et al. Non-gaussian quantum state generation by multi-photon subtraction at the telecommunication wavelength. *Optics Express*, 31(8):12865–12879, 2023.

[75] Miller Eaton, Amr Hossameldin, Richard J Birrittella, Paul M Alsing, Christopher C Gerry, Hai Dong, Chris Cuevas, and Olivier Pfister. Resolution of 100 photons and quantum generation of unbiased random numbers. *Nature Photonics*, 17(1):106–111, 2023.

[76] MD Audley, WS Holland, WD Duncan, David Atkinson, Mark Cliffe, Maureen Ellis, Xiaofeng Gao, DC Gostick, Trevor Hodson, Dennis Kelly, et al. Scuba-2: A large-format tes array for submillimetre astronomy. *Nuclear Instruments and Methods in Physics Research Section A: Accelerators, Spectrometers, Detectors and Associated Equipment*, 520(1-3):479–482, 2004.

[77] MD Niemack, Y Zhao, E Wollack, R Thornton, ER Switzer, DS Swetz, ST Staggs, L Page, O Stryzak, H Moseley, et al. A kilopixel array of tes bolometers for act: Development, testing, and first light. *Journal of Low Temperature Physics*, 151:690–696, 2008.

[78] Kent D Irwin. Squids and transition-edge sensors. *Journal of Superconductivity and Novel Magnetism*, 34(6):1601–1606, 2021.

[79] Joel N Ullom and Douglas A Bennett. Review of superconducting transition-edge sensors for x-ray and gamma-ray spectroscopy. *Superconductor Science and Technology*, 28(8):084003, 2015.

[80] Luciano Gottardi and Stephen Smith. Transition-edge sensors for cryogenic x-ray imaging spectrometers. In *Handbook of X-ray and Gamma-ray Astrophysics*, pages 1–46. Springer, 2022.

[81] SJ Lee, JS Adams, SR Bandler, JA Chervenak, ME Eckart, FM Finkbeiner, RL Kelley, CA Kilbourne, FS Porter, JE Sadleir, et al. Fine pitch transition-edge sensor x-ray microcalorimeters with sub-ev energy resolution at 1.5 kev. *Applied Physics Letters*, 107(22), 2015.

[82] E Taralli, M de Wit, L Gottardi, K Nagayoshi, S Visser, ML Ridder, H Akamatsu, D Vaccaro, MP Bruijn, JR Gao, et al. Small size transition-edge sensors for future x-ray applications. *Journal of Low Temperature Physics*, 209(3):256–262, 2022.

[83] Roland den Hartog, D Boersma, M Bruijn, B Dirks, L Gottardi, H Hoevers, R Hou, Mikko Kiviranta, P De Korte, J Van Der Kuur, et al. Baseband feedback for frequency-domain-multiplexed readout of tes x-ray detectors. In *AIP Conference Proceedings*, volume 1185, pages 261–264. American Institute of Physics, 2009.

[84] Stephen J Smith, Joseph S Adams, Simon R Bandler, Sophie Beaumont, James A Chervenak, Edward V Denison, William B Doriese, Malcolm Durkin, Fred M Finkbeiner, Joseph W Fowler, et al. Performance of a broad-band, high-resolution, transition-edge sensor spectrometer for x-ray astrophysics. *IEEE Transactions on Applied Superconductivity*, 31(5):1–6, 2021.

[85] Alex D Semenov, Gregory N Gol'tsman, and Alexander A Korneev. Quantum detection by current carrying superconducting film. *Physica C: Superconductivity*, 351(4):349–356, 2001.

[86] Emma E Wollman, Varun B Verma, Andrew D Beyer, Ryan M Briggs, B Korzh, Jason P Allmaras, Francesco Marsili, Adriana E Lita, RP Mirin, Sae Woo Nam, et al. Uv superconducting nanowire single-photon detectors with high efficiency, low noise, and 4 k operating temperature. *Optics express*, 25(22):26792–26801, 2017.

[87] Jiansong Gao, MR Vissers, MO Sandberg, FCS Da Silva, Sae Woo Nam, DP Pappas, DS Wisbey, EC Langman, SR Meeker, BA Mazin, et al. A titanium-nitride near-infrared kinetic inductance photon-counting detector and its anomalous electrodynamics. *Applied Physics Letters*, 101(14), 2012.

[88] Paul Szypryt, SR Meeker, G Coiffard, N Fruitwala, B Bumble, G Ulbricht, AB Walter, M Daal, C Bockstiegel, G Collura, et al. Large-format platinum silicide microwave kinetic inductance detectors for optical to near-ir astronomy. *Optics Express*, 25(21):25894–25909, 2017.

[89] Sam Rowe, Enzo Pascale, Simon Doyle, Chris Dunscombe, Peter Hargrave, Andreas Papageorgio, Ken Wood, Peter AR Ade, Peter Barry, Aurélien Bideaud, et al. A passive terahertz video camera based on lumped element kinetic inductance detectors. *Review of Scientific Instruments*, 87(3), 2016.

[90] BA Mazin, Seth R Meeker, MJ Strader, P Szypryt, D Marsden, JC Van Eyken, GE Duggan, AB Walter, G Ulbricht, M Johnson, et al. Arcons: A 2024 pixel optical through near-ir cryogenic imaging spectrophotometer. *Publications of the Astronomical Society of the Pacific*, 125(933):1348–1361, 2013.

[91] W Guo, X Liu, Y Wang, Q Wei, LF Wei, J Hubmayr, J Fowler, J Ullom, L Vale, MR Vissers, et al. Counting near infrared photons with microwave kinetic inductance detectors. *Applied Physics Letters*, 110(21), 2017.

[92] Nicholas Zobrist, Grégoire Coiffard, Bruce Bumble, Noah Swimmer, Sarah Steiger, Miguel Daal, Giulia Collura, Alex B Walter, Clint Bockstiegel, Neelay Fruitwala, et al. Design and performance of hafnium optical and near-ir kinetic inductance detectors. *Applied Physics Letters*, 115(21), 2019.

[93] Pieter J De Visser, Steven AH De Rooij, Vignesh Murugesan, David J Thoen, and Jochem JA Baselmans. Phonon-trapping-enhanced energy resolution in superconducting single-photon detectors. *Physical Review Applied*, 16(3):034051, 2021.

[94] Weijun Zhang, Jia Huang, Chengjun Zhang, Lixing You, Chaolin Lv, Lu Zhang, Hao Li, Zhen Wang, and Xiaoming Xie. A 16-pixel interleaved superconducting nanowire single-photon detector array with a maximum count rate exceeding 1.5 ghz. *IEEE Transactions on Applied Superconductivity*, 29(5):1–4, 2019.

[95] Daiji Fukuda, Go Fujii, Takayuki Numata, Akio Yoshizawa, Hidemi Tsuchida, Shuichiro Inoue, and Tatsuya Zama. Titanium tes based photon number resolving detectors with 1 mhz counting rate and 65% quantum efficiency. In *Quantum Communications Realized II*, volume 7236, pages 60–69. SPIE, 2009.

[96] Roger W Romani, Aaron J Miller, B Cabrera, Sae Woo Nam, and John M Martinis. Phase-resolved crab studies with a cryogenic transition-edge sensor spectrophotometer. *The Astrophysical Journal*, 563(1):221, 2001.

[97] Leonardo Assis Morais, Till Weinhold, Marcelo Pereira de Almeida, Joshua Combes, Adriana Lita, Thomas Gerrits, Sae Woo Nam, Andrew G White, and Geoff Gillett. Precisely determining photon-number in real-time. *arXiv preprint arXiv:2012.10158*, 2020.

[98] JWN Los, Mariia Sidorova, BL Rodriguez, Patrick Qualm, J Chang, S Steinhauer, V Zwiller, and I Esmaeil Zadeh. High-performance photon number resolving detectors for 850-950 nm wavelengths. *arXiv preprint arXiv:2401.07265*, 2024.

[99] Hiroyuki Shibata, Kentaro Fukao, Naoto Kirigane, Shinichi Karimoto, and Hideki Yamamoto. Snspd with ultimate low system dark count rate using various cold filters. *IEEE Transactions on Applied Superconductivity*, 27(4):1–4, 2016.

[100] Mauro Rajteri, Maria Luisa Rastello Rastello, and Eugenio Monticone. Antireflection coatings for superconducting photodetectors. *Nuclear Instruments and Methods in Physics Research Section A: Accelerators, Spectrometers, Detectors and Associated Equipment*, 444(1-2):461–464, 2000.

[101] Aaron J Miller, Adriana E Lita, Brice Calkins, Igor Vayshenker, Steven M Gruber, and Sae Woo Nam. Compact cryogenic self-aligning fiber-to-detector coupling with losses below one percent. *Optics express*, 19(10):9102–9110, 2011.

[102] Lapo Lolli, Emanuele Taralli, Chiara Portesi, Diego Alberto, Mauro Rajteri, and Eugenio Monticone. Ti/au transition-edge sensors coupled to single mode optical fibers aligned by si v-groove. *IEEE transactions on applied superconductivity*, 21(3):215–218, 2011.

[103] Xintong Hou, Ni Yao, Lixing You, Hao Li, Yong Wang, Weijun Zhang, Heqing Wang, Xiaoyu Liu, Wei Fang, Limin Tong, et al. Ultra-broadband microfiber-coupled superconducting single-photon detector. *Optics Express*, 27(18):25241–25250, 2019.

[104] Pei-Sa Ma, Hong-Fan Zhang, and Xingxiang Zhou. Aligning superconducting transition-edge sensors by reflected wave intensity measurement. *Sensors*, 23(7):3495, 2023.

[105] Pei-Sa Ma, Hong-Fan Zhang, and Xingxiang Zhou. Fiber-sensor alignment based on surface microstructures. *Optics Express*, 31(1):737–744, 2023.

[106] G Fujii, D Fukuda, T Numata, A Yoshizawa, H Tsuchida, and S Inoue. Thin gold covered titanium transition edge sensor for optical measurement. *Journal of Low Temperature Physics*, 167:815–821, 2012.

[107] Adriana E Lita, Brice Calkins, LA Pellochoud, Aaron J Miller, and Sae Nam. High-efficiency photon-number-resolving detectors based on hafnium transition-edge sensors, 2009.

[108] Hong-Fan Zhang, Pei-Sa Ma, and Xingxiang Zhou. Titanium/silver transition-edge sensors for photon-number-resolving measurement. *IEEE Transactions on Applied Superconductivity*, 2024.

[109] Yuki Mitsuya, Toshio Konno, Sachiko Takasu, Kaori Hattori, Masashi Ohno, Daiji Fukuda, and Hiroyuki Takahashi. Photon number resolution with an iridium optical transition edge sensor at a telecommunication wavelength. *Journal of Low Temperature Physics*, 210(3):498–505, 2023.

[110] Carlo Pepe, Benedetta Corcione, Francesco Pandolfi, Hobey Garrone, Eugenio Monticone, Ilaria Rago, Gianluca Cavoto, Alice Apponi, Alessandro Ruocco, Federico Malnati, et al. Detection of low-energy electrons with transition-edge sensors. *arXiv preprint arXiv:2405.19475,*, 2024.

[111] KM Patel, S Withington, AG Shard, DJ Goldie, and CN Thomas. Electron spectroscopy using transition-edge sensors. *Journal of Applied Physics*, 135(22), 2024.

[112] FT Jaeckel, CV Ambarish, N Christensen, R Gruenke, L Hu, D McCammon, M McPheron, M Meyer, KL Nelms, A Roy, et al. Energy calibration of high-resolution x-ray tes microcalorimeters with 3 ev optical photons. *IEEE Transactions on Applied Superconductivity*, 29(5):1–4, 2019.

[113] L Lolli, Emanuele Taralli, Mauro Rajteri, T Numata, and D Fukuda. Characterization of optical fast transition-edge sensors with optimized fiber coupling. *IEEE transactions on applied superconductivity*, 23(3):2100904–2100904, 2013.

[114] Chiara Portesi, Emanuele Taralli, L Lolli, Mauro Rajteri, and Eugenio Monticone. Fabrication and characterization of fast tess with small area for single photon counting. *IEEE Transactions on Applied Superconductivity*, 25(3):1–4, 2014.

[115] Brice Calkins, Adriana E Lita, Anna E Fox, and Sae Woo Nam. Faster recovery time of a hot-electron transition-edge sensor by use of normal metal heat-sinks. *Applied Physics Letters*, 99(24), 2011.

[116] Ruslan Hummatov, Adriana E Lita, Tannaz Farrahi, Negar Otrooshi, Samuel Fayer, Matthew J Collins, Malcolm Durkin, Douglas Bennett, Joel Ullom, Richard P Mirin, et al. Fast transition-edge sensors suitable for photonic quantum computing. *Journal of Applied Physics*, 133(23), 2023.

[117] Kent D Irwin, Gene C Hilton, David A Wollman, and John M Martinis. Thermal-response time of superconducting transition-edge microcalorimeters. *Journal of Applied Physics*, 83(8):3978–3985, 1998.

[118] L Lolli, Emanuele Taralli, and Mauro Rajteri. Ti/au tes to discriminate single photons. *Journal of Low Temperature Physics*, 167:803–808, 2012.

[119] Dietmar Drung, C Abmann, J Beyer, A Kirste, M Peters, F Ruede, and Th Schurig. Highly sensitive and easy-to-use squid sensors. *IEEE Transactions on Applied Superconductivity*, 17(2):699–704, 2007.

[120] Magnicon GmbH. Xxf-1 - ultra-high bandwidth dc squid electronics https://www.magnicon.com. https://www.magnicon.com, 2011. Accessed: 2024-05-14.

[121] Mark Anton Lindeman. *Microcalorimetry and the transition-edge sensor*. University of California, Davis, 2000.

[122] Guglielmo Ventura and Lara Risegari. *The art of cryogenics: low-temperature experimental techniques*. Elsevier, 2010.

[123] WS Boyle and KF Rodgers. Performance characteristics of a new low-temperature bolometer. *JOSA*, 49(1):66–69, 1959.

[124] Enectali Figueroa Feliciano. *Theory and development of position-sensitive quantum calorimeters*. Stanford University, 2001.

[125] High Precision Devices, Inc. Adr cryostat installation and operation manual https://hpd-online.com. https://hpd-online.com, 2016. Accessed: 2024-05-14.

[126] www.amuneal.com/magnetic-shielding/magnetic-shielding-materials-2. Amuneal manufacturing corp magnetic shielding materials, 2024. Accessed: 2024-06-19.

[127] Scientific Instruments. *RO-600 Ruthenium Oxide Temperature Sensor Datasheet https://scientificinstruments.com*. Scientific Instruments, 2016. Accessed: 2024-05-14.

[128] Norland optical adhesive 68, https://www.norlandprod.com/adhesives/noa%2068.html, 2024. Accessed: 2024-06-19.

[129] Sebastian MF Raupach, Ivo Pietro Degiovanni, Hristina Georgieva, Alice Meda, Helmuth Hofer, Marco Gramegna, Marco Genovese, Stefan Kück, and Marco López. Detection rate dependence of the inherent detection efficiency in single-photon detectors based on avalanche diodes. *Physical Review A*, 105(4):042615, 2022.

[130] Marco López, Helmuth Hofer, and Stefan Kück. Detection efficiency calibration of single-photon silicon avalanche photodiodes traceable using double attenuator technique. *Journal of Modern Optics*, 62(20):1732–1738, 2015.

[131] Robert Williams Wood. A new form of cathode discharge and the production of x-rays, together with some notes on diffraction. preliminary communication. *Physical Review (Series I)*, 5(1):1, 1897.

[132] Sumio Iijima. Helical microtubules of graphitic carbon. *nature*, 354(6348):56–58, 1991.

[133] LA Chernozatonskii, Yu V Gulyaev, Z Ja Kosakovskaja, NI Sinitsyn, GV Torgashov, Yu F Zakharchenko, EA Fedorov, and VP Val'chuk. Electron field emission from nanofilament carbon films. *Chemical Physics Letters*, 233(1-2):63–68, 1995.

[134] Ralph Howard Fowler and Lothar Nordheim. Electron emission in intense electric fields. *Proceedings of the Royal Society of London. Series A, Containing Papers of a Mathematical and Physical Character*, 119(781):173–181, 1928.

[135] Emily Schifano, Gianluca Cavoto, Francesco Pandolfi, Giorgio Pettinari, Alice Apponi, Alessandro Ruocco, Daniela Uccelletti, and Ilaria Rago. Plasma-etched vertically aligned cnts with enhanced antibacterial power. *Nanomaterials*, 13(6):1081, 2023.

[136] Ravi Prakash Yadav, Ilaria Rago, Francesco Pandolfi, Carlo Mariani, Alessandro Ruocco, Sammar Tayyab, Alice Apponi, and Gianluca Cavoto. Evaluation of vertical alignment in carbon nanotubes: A quantitative approach. *Nuclear Instruments and Methods in Physics Research Section A: Accelerators, Spectrometers, Detectors and Associated Equipment*, 1060:169081, 2024.

[137] Fabrizio Sarasini, Jacopo Tirillò, Matteo Lilli, Maria Paola Bracciale, Per Erik Vullum, Filippo Berto, Giovanni De Bellis, Alessio Tamburrano, Gianluca Cavoto, Francesco Pandolfi, and Ilaria Rago. Highly aligned growth of carbon nanotube forests with in-situ catalyst generation: A route to multifunctional basalt fibres. *Composites Part B: Engineering*, 243:110136, 2022.

[138] Sammar Tayyab, Alice Apponi, Maria Grazia Betti, Elena Blundo, Gianluca Cavoto, Riccardo Frisenda, Nuria Jiménez-Arévalo, Carlo Mariani, Francesco Pandolfi, Antonio Polimeni, et al. Spectromicroscopy study of induced defects in ion-bombarded highly aligned carbon nanotubes. *Nanomaterials*, 14(1):77, 2024.

[139] Eugenio Monticone, Micaela Castellino, Roberto Rocci, and Mauro Rajteri. Ti/au ultrathin films for tes application. *IEEE Transactions on Applied Superconductivity*, 31(5):1–5, 2021.

[140] John M Martinis, Gene C Hilton, Kent D Irwin, and David A Wollman. Calculation of tc in a normal-superconductor bilayer using the microscopic-based usadel theory. *Nuclear Instruments and Methods in Physics Research Section A: Accelerators, Spectrometers, Detectors and Associated Equipment*, 444(1-2):23–27, 2000.

[141] A Peruzzi, E Gottardi, F Pavese, I Peroni, and G Ventura. Investigation of the titanium superconducting transition as a temperature reference point below 0.65 k. *Metrologia*, 37(3):229, 2000.

[142] Mark A Lindeman, Simon Bandler, Regis P Brekosky, James A Chervenak, Enectali Figueroa-Feliciano, Fred M Finkbeiner, Mary J Li, and Caroline A Kilbourne. Impedance measurements and modeling of a transition-edge-sensor calorimeter. *Review of Scientific Instruments*, 75(5):1283–1289, 2004.

[143] Emanuele Taralli, Chiara Portesi, L Lolli, Eugenio Monticone, Mauro Rajteri, I Novikov, and J Beyer. Impedance measurements on a fast transition-edge sensor for optical and near-infrared range. *Superconductor Science and Technology*, 23(10):105012, 2010.

[144] Emanuele Taralli, L Lolli, Eugenio Monticone, Mauro Rajteri, Luca Callegaro, T Numata, and D Fukuda. Full characterization of optical transition-edge

sensor by impedance spectroscopy measurements in a bandwidth extending to 1 mhz. In *2013 IEEE 14th International Superconductive Electronics Conference (ISEC)*, pages 1–4. IEEE, 2013.

[145] Emanuele Taralli, Carlos Pobes, Pourya Khosropanah, Lourdes Fàbrega, Agustín Camón, Luciano Gottardi, Kenichiro Nagayoshi, ML Ridder, MP Bruijn, and JR Gao. Ac/dc characterization of a ti/au tes with au/bi absorber for x-ray detection. *Journal of Low Temperature Physics*, 199:102–109, 2020.

[146] K Hattori, R Kobayashi, T Numata, S Inoue, and D Fukuda. Complex impedance of fast optical transition edge sensors up to 30 mhz. *Journal of Low Temperature Physics*, 193(3):217–224, 2018.

[147] Kimmo Kinnunen. *Studies of transition-edge sensor physics: Thermal models and noise*. PhD thesis, University of Jyväskylä, 2011.

[148] Wen Zhang, Zheng Wang, Jia-Qiang Zhong, Pei-Zhang Li, Yue Geng, Wei Miao, Yuan Ren, Kang-Ming Zhou, Qi-Jun Yao, and Sheng-Cai Shi. Evidence for controllable reduction of critical temperature in titanium tess by baking in air. *IEEE Transactions on Applied Superconductivity*, 31(5):1–5, 2021.

[149] Diego Alberto, Mauro Rajteri, Emanuele Taralli, L Lolli, Chiara Portesi, Eugenio Monticone, Yifan Jia, Roberto Garello, and Michela Greco. Optical transition-edge sensors single photon pulse analysis. *IEEE transactions on applied superconductivity*, 21(3):285–288, 2010.

[150] A. Apponi, F. Pandolfi, I. Rago, G. Cavoto, C. Mariani, and A. Ruocco. Absolute efficiency of a two-stage microchannel plate for electrons in the 30 - 900 eV energy range. *Measur. Sci. Tech.*, 33:025102, 2022.

[151] Alice Apponi, Gianluca Cavoto, Marco Iannone, Carlo Mariani, Francesco Pandolfi, Daniele Paoloni, Ilaria Rago, and Alessandro Ruocco. Response of windowless silicon avalanche photo-diodes to electrons in the 90–900 eV range. *JINST*, 15(11):P11015, 2020.

[152] Matteo Gugiatti, Matteo Biassoni, Marco Carminati, Oliviero Cremonesi, Carlo Fiorini, Pietro King, Peter Lechner, Susanne Mertens, Lorenzo Pagnanini, Maura Pavan, and Stefano Pozzi. Characterisation of a silicon drift detector for high-resolution electron spectroscopy. *Nuclear Instruments and Methods in Physics Research Section A: Accelerators, Spectrometers, Detectors and Associated Equipment*, 979:164474, 2020.

[153] M. G. Betti et al. A design for an electromagnetic filter for precision energy measurements at the tritium endpoint. *Prog. Part. Nucl. Phys.*, 106:120–131, 2019.

[154] E. Monticone, A. M. Rossi, M. Rajteri, R. S. Gonnelli, V. Lacquaniti, and G. Amato. Structural and morphological properties of evaporated siox films. *Philosophical Magazine B*, 80(4):523–529, 2000.

[155] Masaaki Araidai, Yasuhiro Nakamura, and Kazuyuki Watanabe. Field emission mechanisms of graphitic nanostructures. *Phys. Rev. B*, 70:245410, Dec 2004.

[156] Robert Gomer. Field emission, field ionization, and field desorption. *Surface Science*, 299-300:129–152, 1994.

[157] Pauli Virtanen, Ralf Gommers, Travis E. Oliphant, Matt Haberland, Tyler Reddy, David Cournapeau, Evgeni Burovski, Pearu Peterson, Warren Weckesser, Jonathan Bright, Stéfan J. van der Walt, Matthew Brett, Joshua Wilson, K. Jarrod Millman, Nikolay Mayorov, Andrew R. J. Nelson, Eric Jones, Robert Kern, Eric Larson, C J Carey, İlhan Polat, Yu Feng, Eric W. Moore, Jake VanderPlas, Denis Laxalde, Josef Perktold, Robert Cimrman, Ian Henriksen, E. A. Quintero, Charles R. Harris, Anne M. Archibald, Antônio H. Ribeiro, Fabian Pedregosa, Paul van Mulbregt, and SciPy 1.0 Contributors. SciPy 1.0: Fundamental Algorithms for Scientific Computing in Python. *Nature Methods*, 17:261–272, 2020.

[158] Svante Wold, Kim Esbensen, and Paul Geladi. Principal component analysis. *Chemometrics and Intelligent Laboratory Systems*, 2(1):37–52, 1987. Proceedings of the Multivariate Statistical Workshop for Geologists and Geochemists.

[159] David Arthur and Sergei Vassilvitskii. k-means++: the advantages of careful seeding. In *ACM-SIAM Symposium on Discrete Algorithms*, 2007.

[160] nyuad astroparticle: tes analysis, 2024. https://github.com/nyuad-astroparticle/TES-analysis.

[161] Chris Hagmann, David Lange, and Douglas Wright. Cosmic-ray shower generator (cry) for monte carlo transport codes. In *2007 IEEE Nuclear Science Symposium Conference Record*, volume 2, pages 1143–1146, 2007.

[162] Jan Dreyling-Eschweiler. A superconducting microcalorimeter for low-flux detection of near-infrared single photons. Technical report, Deutsches Elektronen-Synchrotron (DESY), 2014.

[163] Gary J. Feldman and Robert D. Cousins. Unified approach to the classical statistical analysis of small signals. *Physical Review D*, 57(7):3873–3889, April 1998.

[164] Santeri Porrasmaa, Timo Dönsberg, Farshid Manoocheri, and Erkki Ikonen. Predictable quantum efficient detector for low optical flux measurements. *Optical Review*, 27:190–194, 2020.

[165] Scaleup website https://scaleup.aalto.fi/.